DARK MATTER BENCHMARK MODELS FOR EARLY LHC RUN-2 SEARCHES: REPORT OF THE ATLAS/CMS DARK MATTER FORUM

Author/contributor list to be added as document is finalized.

Contact editors: lhc-dmf-admin@cern.ch

June 2, 2015

Contents

1

Introduction

Many theories of physics beyond the Standard Model predict the existence of a stable, neutral, weakly-interacting and massive particle that is a putative dark matter candidate. In the following, we refer to such matter as dark matter, even though the observation of such matter at a collider could only establish that it is neutral, weakly-interactive, massive and stable on the distance-scales of 10's of meters. Dark matter has not yet been observed in particle physics experiments, and there is not yet any evidence for non-gravitational interactions between dark matter and Standard Model particles. If such interactions exist, dark matter particles could be produced at the LHC. Since dark matter particles themselves do not produce signals in the LHC detectors, one way to observe them is when they are produced in association with a visible SM particle $X(=g, q, \gamma, Z, W, \text{or } h)$. Such reactions, which are observed at colliders as particles or jets recoiling against an invisible state, are called "mono-X" or $\not{E}_T$+X reactions [FST06, BHK$^+$10, BFH10], where $\not{E}_T$ is the missing transverse momentum observable in the detector. This type of reaction includes the production of a Higgs boson that decays to pairs of dark matter particles.

To do **CD: why singling out mono-Higgs? (??)**

Early LHC Run-1 searches for $\not{E}_T$+X signatures at ATLAS [ATL15d, ATL15c, ATL14c, ATL14b, ATL14a, ATL15b, ATL15a, ATL14d] and CMS [CMS14a, CMS14b, CMS15c, CMS15b, CMS15d, CMS14c, CMS15a] employed a basis of contact interaction operators in effective field theories (EFTs) [GIR$^+$11, GIR$^+$10] to calculate the possible signals. These particular EFTs assume that production of dark matter takes place through a contact interaction involving a quark-antiquark pair or two gluons, and two dark matter particles. In this case, the missing energy distribution of the signal is determined by the nature and the mass of the dark matter particles and the Lorentz structure of the interaction, and only the overall production rate is a free parameter to be constrained or measured. Both experiments studied a variety of EFTs with different spin structures. Provided that the contact interaction approximation holds, these EFTs can also provide a straightforward way to compare the results from different collider searches with non-collider searches for dark matter. From the time of their proposal, however, it was clear that, though the contact interactions provide interesting limits, they are

To do **Check these references here (??)**

not always a good description of dark matter production at the LHC in the regime of interest [GIR$^+$11, SV12].

The interpretation of Tevatron [A$^+$12a] and Run-1 LHC searches as constraints on contact interactions provided results that were outside the range of applicability of the EFT description, requiring further study [BFH10, Kop11, FHKT11, FHKT12, SV12, BDSMR14]. Some "simplified models" [AST09, GS11, A$^+$12b] of dark matter production were constructed, including particles and interactions beyond the SM. These models can be used consistently at LHC energies, and provide an extension to the EFT approach. Many proposals for such models have emerged (see, for example Refs. [AJW12, AHW13, DNRT13, BDM14, BB13, BB14, AWZ14, A$^+$14a, MMA$^+$14, HKSW15, BFG15, HR15, BT13, CNS$^+$13, BDG$^+$12, PS14, CDM$^+$14]). These models introduce a new particle – a mediator – that allows interactions between SM and DM particles. In the limit of large mediator mass, these simplified models map onto EFT operators. If the mass of the mediator is small, the kinematics of the dark matter production can differ substantially from that due to a contact interaction, modifying limits and possibly requiring new search strategies. Appropriate simplified models can be used both to interpret Dark Matter searches at the LHC, and to guide the design of complementary search signatures.

To do **CD: How are those references chosen? (??)**

1.1   The ATLAS/CMS Dark Matter Forum

To understand what signal models should be used for the upcoming LHC Run 2, groups of experimenters from both ATLAS and CMS collaborations have held separate discussions with small groups of theorists [MMA$^+$14, A$^+$14a]. Another joint discussion was held at the DM@LHC workshop in Oxford, in September 2014 [par]. As discussed at the DM@LHC workshop, ATLAS and CMS organized a forum at the end of 2014, called the *ATLAS-CMS Dark Matter Forum*, to form a consensus on the use of simplified models and EFTs for Run-2 with the participation of experts on theories of dark matter. This is the final report of that forum.

One of the guiding principles of this report is to channel the efforts of the ATLAS and CMS collaborations towards a minimal set of dark matter models that should influence the design of the early Run-2 searches. At the same time, a thorough survey of realistic collider signals of dark matter is a crucial input to the overall design of the search program.

The goal of this report is such a survey, though confined within some broad assumptions and focused on benchmarks for kinematically-distinct signals which are most urgently needed. As far as time and resources have allowed, the assumptions have been carefully motivated by theoretical consensus and comparisons of simulations. But, to achieve a true consensus in only a few months before the start of Run-2, it was important to restrict the scope and timescale to the following:

1. The forum should propose a prioritized, compact set of bench-mark simplified models that should be agreed upon by both collaborations for Run-2 searches. The values for the scan on the parameters of the models for which experimental results are provided should be specified, to facilitate theory reinterpretation beyond the necessary model-independent limits that should be provided by all LHC Dark Matter searches.

2. The forum should standardize the event generator implementation of the simplified models and harmonize other common technical details as far as practical. It would be desirable to have a common choice of LO/NLO, ME-parton shower matching and merging, factorization and renormalization scales for each of the simplified models. This will also lead to a common set of theory uncertainties, which will facilitate the comparison of results between the two collaborations.

3. The forum could also discuss how to apply the EFT formalism and present the results of EFT interpretations.

4. The forum should prepare a report summarizing these items, suitable both as a reference for the internal ATLAS and CMS audiences and as an explanation of Run-2 benchmarks for theory and non-collider readers. This report represents the views of the participants of the forum.

1.2 *Grounding Assumptions*

We assume that interactions exist between Standard Model hadrons and whatever the particle that constitutes cosmological dark matter. If this is not the case, then proton collisions will not produce dark matter particles, and dark matter will not scatter off nuclei in direct detection experiments.

The Dark Matter itself is assumed to be a single particle, a Dirac fermion WIMP, stable on collider timescales and non-interacting with the detector. The former assumption is reductionistic. The rich particle content of the Standard Model is circumstantial evidence that the dark matter sector, which constitutes five times as much of the mass of the universe, may be more complex than a single particle or a single interaction. But, as was often the case in the discoveries of the SM, here only one mediator and one search channel might play a dominant role in the opening stages of an LHC discovery. The latter assumption focuses our work on early LHC searches, where small kinematic differences between models will not matter in a discovery scenario, and with the imminent re-start of the LHC our report relies heavily on a large body of existing theoretical work which made this assumption. Different types of dark matter particles will typically give similar results. Some exceptions exist: the choice of Dirac fermions forbids some processes that are allowed for Majorana fermions [GIR+11]. Aside from this, the

cases of Dirac or Majorana fermions or scalars produce only minor changes in the kinematic distributions of the visible particle, especially when considering cut-and-count[1] analysis. Thus the choice of Dirac fermion dark matter is deemed sufficient for the benchmarks aiding the design of the upcoming Run-2 searches. Nevertheless, a more complete set of models will certainly be required upon a discovery; see e.g. [CHLR13, HHR14, CHH15] for some studies of observables that may distinguish amongst these models.

Simplified models are considered in depth within this report since a strength of collider experiments lies in the ability to study the mediator, not just the DM. A discovery of an anomalous $\not{E}_T$ signature at the LHC would not uniquely imply discovery of dark matter, while at the same time discovery of an anomalous and annually-modulated signal in a direct-detection experiment would leave unanswered many questions about the nature of the interaction that could be resolved by the simultaneous discovery of a new mediator particle. Collider, direct, and indirect detection searches provide complementary ways to approach this problem, and it is in this spirit that our focus is on the mediator. We systematically explore the basic possibilities for mediators of various possible spins and couplings. All models considered are assumed to produce a signature with pairs of dark matter particles. Though more varied and interesting possibilities are added to the literature almost daily, these basic building blocks account for much of the physics studied at hadron colliders in the past three decades.

We also assume that Minimal Flavor Violation (MFV) [CG87, HR90, BGG+01, DGIS02] applies to the models included in this report. This means that the flavor structure of the couplings between dark matter and ordinary particles follows the same structure as the Standard Model. This choice is simple, since no additional theory of flavor is required, beyond what is already present in the SM, and it provides a mechanism to ensure that the models do not violate flavor constraints. As a consequence, spin-0 resonances must have couplings to fermions proportional to the SM Higgs couplings. Flavor-safe models can still be constructed beyond the MFV assumption, for example [ABG14], and deserve further study.

In the parameter scan for the models considered in this report, we make the assumption of a minimal decay width for the particles mediating the interaction between SM and DM. This means that only decays strictly necessary for the self-consistency of the model (e.g. to DM and to quarks) are accounted for in the definition of the mediator width. We forbid any further decays to other invisible particles of the Dark Sector that may increase the width or produce striking, visible signatures. Studies within the Forum show that, for cut-and-count analyses, the kinematic distributions of many models, and therefore the sensitivity of the search, do not depend significantly on the mediator width, as long as the width remains smaller than the mass of the particle.

The particle content of the models chosen as benchmarks is

[1] Cut-and-count refers to an analysis that applies a certain event selection and checks the inclusive number of events which pass. This is to be contrasted with a shape analysis, which compares the distribution of events.

limited to one single kind of DM whose self-interactions are not
relevant for LHC phenomenology, and to one type of SM/DM
interaction at a time. These assumptions only add a limited number
of new particles to the SM. These simplified models, independently
explored by different experimental analyses, can be used as starting
points to build more complete theories. Even though this factorized
picture does not always lead to full theories and leaves out details
that are necessary for the self-consistency of single models (e.g.
the mass generation for mediator particles), it is a starting point to
prepare a set of distinct but complementary collider searches for
Dark Matter, as it leads to benchmarks that are easily comparable
across channels.

1.3   *Choices of benchmarks considered in this report*

Contact interaction operators have been outlined as a complete se-
ries of theoretical building blocks representing possible types of
interactions between SM and DM particles in [GIR$^+$10]. The ap-
proach followed by LHC searches (see e.g. Refs. [CMS14a, ATL15d]
for the most recent jet+$\not{E}_T$ Run-1 searches with the 8 TeV dataset)
so far has been to simulate only a prioritized set of the possible
operators with distinct kinematics for the interpretation of the con-
straints obtained, and provide results to be reinterpreted in terms
of the other operators. This report intends to follow this strategy,
firstly focusing on simplified models that allow the exploration
of scenarios where the mediating scale is not as large. Secondly,
this report considers specific EFT benchmarks whenever neither a
simplified model completion nor other simplified models yielding
similar kinematic distributions are available. This is the case for
dimension-5 or dimension-7 operators with direct Dark Matter-
electroweak boson couplings. Considering these models as separate
experimental benchmarks will allow to target new signal regions
and help validate the contact interaction limit of new simplified
models developed to complete these specific operators.

In all cases, experimental searches should deliver results that are
independent from the specific benchmark tested. Furthermore, it
should be possible to map results from simplified models to contact
operators, in the high mediator mass limit. Results from EFT bench-
marks should include the condition that the momentum transfer
does not probe the scale of the interaction; whenever there is no
model that allows a direct mapping between these two quantities,
various options should be tested to ensure a given fraction of events
within the range of applicability of the EFT approach.

1.4   *Structure of this report*

Chapter 2 of the report is dedicated to simplified models with ra-
diation of a hard object either from the initial state or from the
mediator. These models produce primarily monojet signatures,

but should be considered for all $\not{E}_T$+X searches. Details of the implementation of these models in Monte Carlo generators are provided in Appendix A. Chapter 3 contains the benchmark model recommendations and choices for final states specifically containing an electroweak boson ($W/Z/\gamma/H$). In this case, both simplified models leading to mono-boson signatures and contact interaction operators are considered. Chapter 4 is devoted to the treatment of the presentation of results for the benchmark models from contact interaction operators. Chapter 5 prescribes how to estimate theoretical uncertainties on the simulation of these models. Chapter 6 concludes the report. Appendix C contains the necessary elements that should be included in the results of experimental searches to allow for further reinterpretation. The technical implementation and further models that can be studied beyond early searches are described in Appendix B. For these models, either the implementation could not be fully developed by the time of this report, or some of the grounding assumptions were not fully met. Some of these models have been used in previous ATLAS and CMS analyses and discussed thoroughly within the Forum. They are therefore worth considering for further studies and for Run-2 searches, since they lead to unique $\not{E}_T$+X signatures that are not produced by any other of the models included in this report.

2

Simplified models for all $\not{E}_T$ +X analyses

In this Chapter we review models that yield $X+\not{E}_T$ signatures, where X is a QCD parton or γ, W, Z or h.

The primary simplified models for Dirac fermion DM endorsed by this Forum are detailed in this Chapter, comprising spin-0 and spin-1 mediators. Section 2.1 covers the s-channel exchange of a vector mediator [1], while we consider both s-channel and t-channel exchange for scalar mediators in Section 2.2 and 2.3 respectively. Spin-2 mediators are briefly mentioned in Section 2.4. While these models are general and cover a broad set of signatures, the discussion and studies are focused on the monojet final state. Details on final states with EW boson radiation and with heavy flavor quarks from diagrams arising within these models are also discussed in this Chapter.

The simplified model where a vector mediator is exchanged in the s-channel is known to NLO accuracy in the case of DM pair production in association to one parton **??**. All other models are currently known to leading order. Appendix A details the recommended implementation of these models that have been used for the studies in this Chapter. A summary of the recommendation of the generation of this model is provided in Table **??**.

[1] Colored vector mediators can be exchanged in the t-channel, but there are no examples in literature so far.

2.1 Vector and axial vector mediator, s-channel exchange

A simple extension of the Standard Model (SM) is an additional $U(1)$ gauge symmetry, where a dark matter (DM) candidate particle has charges only under this new group. Assuming that some SM particles are also charged under this group, a new gauge boson can mediate interactions between the SM and DM.

We consider the case of a DM particle χ of mass m_{DM} that is a Dirac fermion and where the production proceeds via the exchange of a spin-1 mediator of mass M_{med} in the s-channel, illustrated in Fig. 2.1.

We consider two models with vector and axial-vector couplings between the spin-1 mediator Z' and SM and DM fields, with the corresponding interaction Lagrangians:
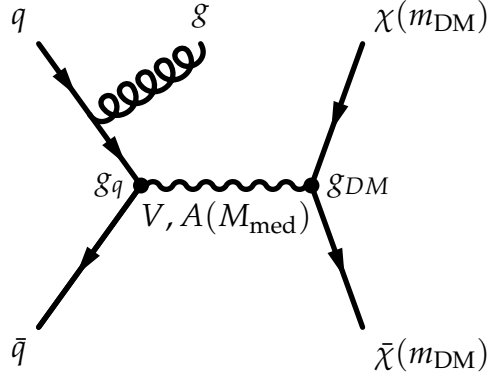
Figure 2.1: Representative Feynman diagram showing the pair production of dark matter particles in association with a parton from the initial state via a vector or axial-vector mediator. The cross section and kinematics depend upon the mediator and dark matter masses, and the mediator couplings to dark matter and quarks respectively: $(M_{\mathrm{med}}, m_{\mathrm{DM}}, g_{\mathrm{DM}}, g_{\mathrm{q}})$.

$$\mathcal{L}_{\mathrm{vector}} = g_{\mathrm{q}} \sum_{q=u,d,s,c,b,t} Z'_\mu \bar{q} \gamma^\mu q + g_{\mathrm{DM}} Z'_\mu \bar{\chi} \gamma^\mu \chi \tag{2.1}$$

$$\mathcal{L}_{\mathrm{axial-vector}} = g_{\mathrm{q}} \sum_{q=u,d,s,c,b,t} Z'_\mu \bar{q} \gamma^\mu \gamma^5 q + g_{\mathrm{DM}} Z'_\mu \bar{\chi} \gamma^\mu \gamma^5 \chi. \tag{2.2}$$

The coupling g_{q} is assumed to be universal to all quarks. As mentioned in the Introduction, when no additional visible or invisible decays contribute to the width of the mediator, the minimal width is fixed by the choices of couplings g_{q} and g_{DM}. The effect of larger widths is discussed in Section 2.5.2. For the vector and axial-vector models, the minimal width is:

$$\Gamma^V_{\mathrm{min}} = \frac{g_{\mathrm{DM}}^2 M_{\mathrm{med}}}{12\pi} \left(1 + \frac{2m_{\mathrm{DM}}^2}{M_{\mathrm{med}}^2} \right) \beta_{DM} \theta(M_{\mathrm{med}} - 2m_{\mathrm{DM}}) \tag{2.3}$$

$$+ \sum_q \frac{3g_{\mathrm{q}}^2 M_{\mathrm{med}}}{12\pi} \left(1 + \frac{2m_q^2}{M_{\mathrm{med}}^2} \right) \beta_q \theta(M_{\mathrm{med}} - 2m_q),$$

$$\Gamma^A_{\mathrm{min}} = \frac{g_{\mathrm{DM}}^2 M_{\mathrm{med}}}{12\pi} \beta_{DM}^{3/2} \theta(M_{\mathrm{med}} - 2m_{\mathrm{DM}}) \tag{2.4}$$

$$+ \sum_q \frac{3g_{\mathrm{q}}^2 M_{\mathrm{med}}}{12\pi} \beta_q^{3/2} \theta(M_{\mathrm{med}} - 2m_q) \, .$$

$\theta(x)$ denotes the Heaviside step function, and $\beta_f = \sqrt{1 - \frac{4m_f^2}{M_{\mathrm{med}}^2}}$ is the velocity of the fermion f with mass m_f in the mediator rest frame. Note the color factor 3 in the quark terms. Figure 2.2 shows the minimal width as a function of mediator mass for both vector and axial-vector mediators assuming $g_{\mathrm{q}} = g_{\mathrm{DM}} = 1$. With this choice of the couplings, the dominant contribution to the minimal width comes from the quarks, due to the combined quark number and color factor enhancement. We specifically assume that the vector mediator does not couple to leptons. If such a coupling were present, it would have a minor effect in increasing the mediator width, but it would also bring in constraints from measurements of the Drell-Yan process that would unnecessarily restrict the model space.

Therefore, the minimal set of parameters under consideration for these two models is

$$\left\{ m_{\mathrm{DM}}, M_{\mathrm{med}}, g_{\mathrm{q}}, g_{\mathrm{DM}} \right\} . \tag{2.5}$$
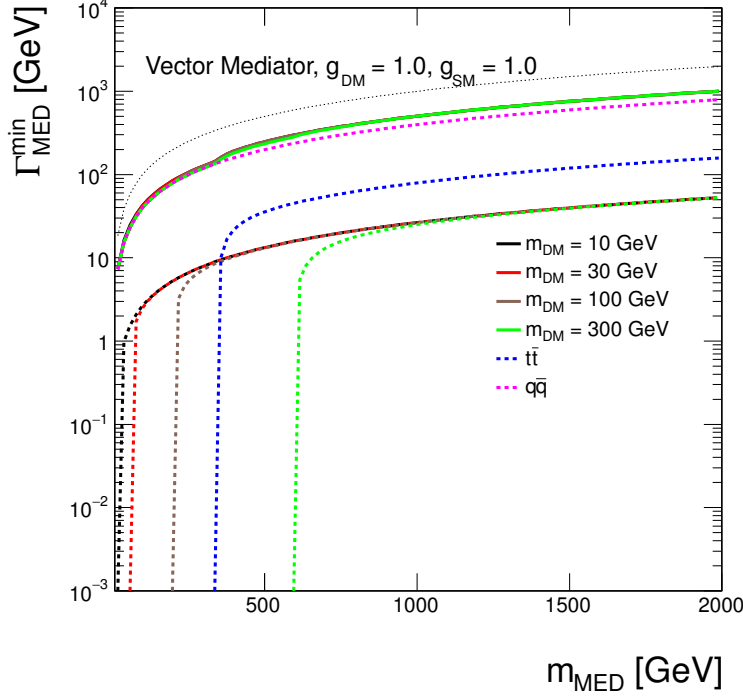
Figure 2.2: Minimal width as a function of mediator mass for vector and axial-vector mediator assuming couplings of 1. The total width is shown as solid lines for Dark Matter masses of 10 GeV, 30 GeV, 100 GeV and 300 GeV in black, red, brown and green, respectively. The individual contributions from Dark Matter are indicated by dotted lines with the same colors. The contribution from all quarks but top is shown as magenta dotted line and the contribution from top quarks only is illustrated by the dotted blue line. The dotted black line shows the extreme case $\Gamma_{min} = M_{med}$.
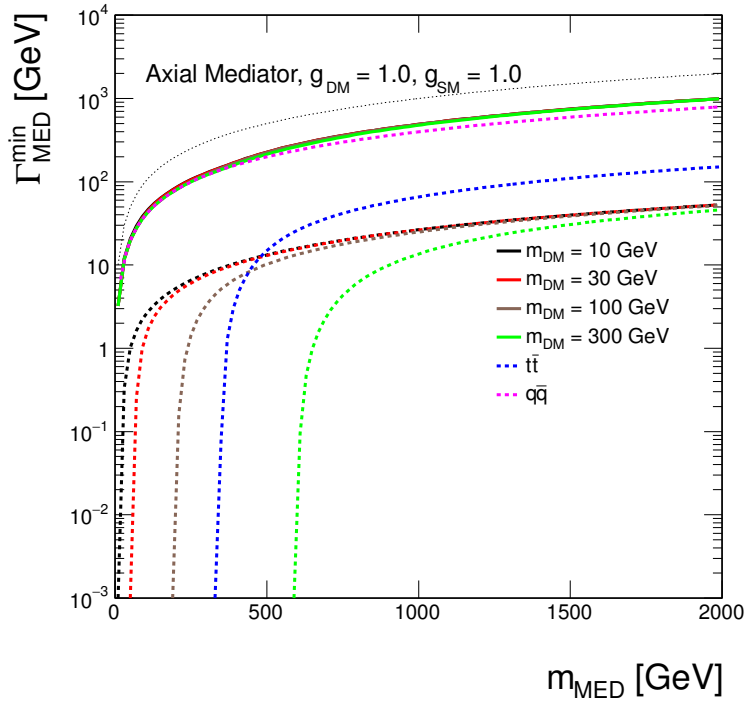
See [BDMM15] for a thorough discussion of these models.

2.1.1 Spin structure of the couplings

In this section, the differences between the vector and axial-vector models are described. Furthermore, it is possible to consider other models in which mixed vector and axial-vector couplings are considered, for instance the couplings to the quarks are axial-vector whereas those to DM are vector. Such comparisons are also presented.

The samples with pure vector and pure axial-vector couplings are compared for $M_{med} = 100$ GeV and different Dark Matter masses in Fig. 2.3. No differences in the shape of the $\not{E}_T$ distributions are observed between the samples with coincident masses.

In the case of the on-shell Dark Matter pair production where $2m_{DM} \ll M_{med}$, the cross sections of the pure vector and pure axial-vector models are similar. With increasing Dark Matter mass towards the $2m_{DM} = M_{med}$ transition and beyond into the off-shell production regime, the relative difference between the cross sections of the two samples is increasing, with the vector samples having larger cross sections.

To do **Do we want to propose to generate one model only and refer to the cross section tables in HEPData repository for the other? (??)**

To do **This can be understood in the eikonal approximation since the A terms have an additional η^2 in front.**

m_{DM} [GeV]		Γ/m_{med}	$\sigma \times A_{300}$ [fb]	$\sigma \times A_{500}$ [fb]
V	10	0.424	1.9e+04	1.8e+03
A	10	0.422	1.9e+04	1.8e+03
V	30	0.423	1.8e+04	1.7e+03
A	30	0.410	1.3e+04	1.3e+03
V	100	0.398	2.9e+03	4.1e+02
A	100	0.397	1.4e+03	2.4e+02

Figure 2.3: Comparison of the pure vector and pure axial-vector couplings. The $\not{E}_T$ distribution is shown for the samples generated with $M_{med} = 100$ GeV and different Dark Matter masses. Ratios of the normalized distributions are shown for between the samples with coincident masses. A_{300} and A_{500} in the table denote the acceptance of the $\not{E}_T > 300$ GeV and $\not{E}_T > 500$ GeV cut, respectively.

Figure 2.4 shows the samples generated with pure and mixed couplings for $m_{DM} = 100$ GeV and $M_{med} = 1$ TeV, i.e. where the Dark Matter pair is produced on-shell. The mediator width between the pure vector and pure axial-vector couplings differ only by 2% in this case, and < 10% agreement between the cross sections is found. The mediator widths for the samples with the same type coupling to quarks agree at better than 1% since the width is dominated by the quark contribution, as expected from Eq. 2.3. No significant differences between the samples with same type Dark Matter coupling are seen, given the statistical precision of the generated samples. This is expected since the mediator is produced

on-shell, and the details of the invisible decay are unimportant in cut-and-count searches.

For the off-shell Dark Matter pair production, shown in Fig. 2.5 for $m_{DM} = 100$ GeV and $M_{med} = 100$ GeV, there is approximately a factor 2 difference between the cross-sections of the samples with pure couplings is observed. As in the previous case, the samples with the same type coupling to Dark Matter are similar both in terms of cross sections and $\not{E}_T$ shape. Since the contribution to the mediator width from Dark Matter is closed in this case, only the quark couplings define the width. Only couplings to light quarks are opened in the case of $M_{med} = 100$ GeV for which the differences between the partial widths of vector and axial-vector couplings are marginal. This explains the similar minimal widths for all four samples stated in Fig. 2.5.

In general, the coupling to quarks is not expected to play an important role as it is only needed to produce the mediator which is confirmed by the observations above. For scalar and psuedoscalar mediators, the coupling to Dark Matter determines the form of the matrix element which explains the similarity of the samples with the same type Dark Matter couplings. Based on these arguments, we recommend to consider only the models with pure vector couplings or pure axial-vector couplings.
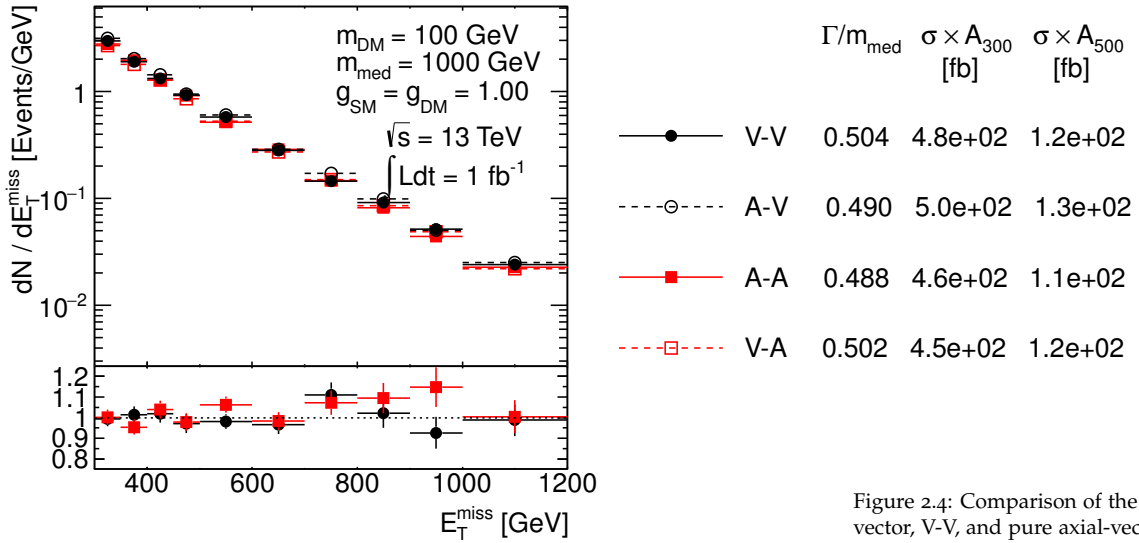
Figure 2.4: Comparison of the pure vector, V-V, and pure axial-vector, A-A, couplings with mixed couplings, A-V and V-A where the first (second) letter indicates the Standard Model (Dark Sector) vertex. The $\not{E}_T$ distribution is shown for the samples generated with $m_{DM} = 100$ GeV and $M_{med} = 1$ TeV. Ratios of the normalized distributions are shown for A-V over V-V and for V-A over A-A. A_{300} and A_{500} in the table denote the acceptance of the $\not{E}_T > 300$ GeV and $\not{E}_T > 500$ GeV cut, respectively.

2.1.2 *Parameter scan*

In order to determine an optimal choice of the parameter grid for the simulation of early Run-2 benchmark models, dependencies of the kinematic quantities and cross sections on the model parameters have been studied. The following paragraphs list the main observations from the scans over the parameters that support the final proposal for the benchmark signal grid.

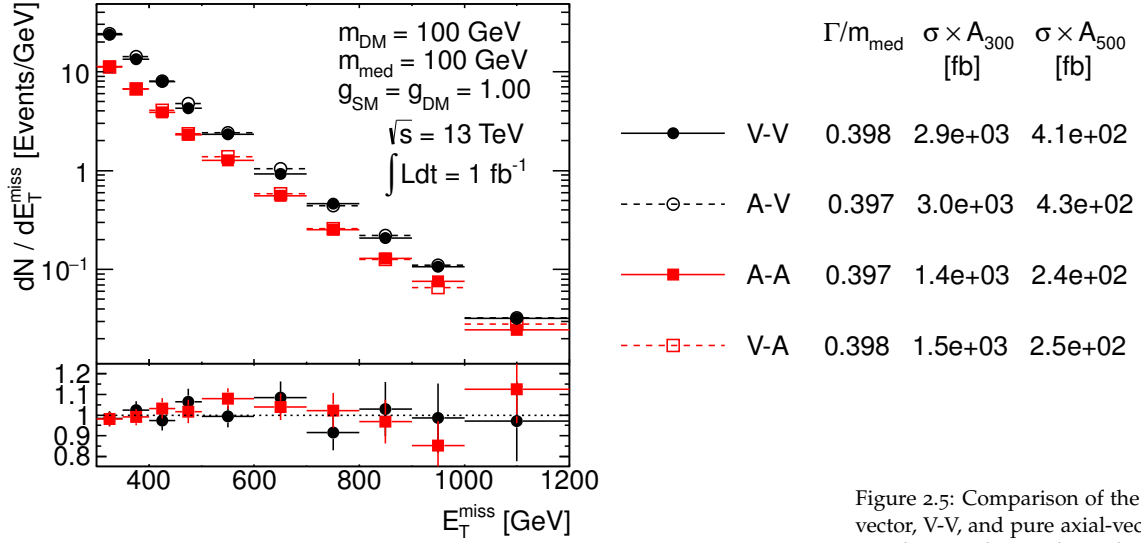|	Γ/m_{med}	$\sigma \times A_{300}$ [fb]	$\sigma \times A_{500}$ [fb]
V-V	0.398	2.9e+03	4.1e+02
A-V	0.397	3.0e+03	4.3e+02
A-A	0.397	1.4e+03	2.4e+02
V-A	0.398	1.5e+03	2.5e+02

Figure 2.5: Comparison of the pure vector, V-V, and pure axial-vector, A-A, couplings with mixed couplings, A-V and V-A where the first (second) letter indicates the Standard Model (Dark Sector) vertex. The $\not{E}_T$ distribution is shown for the samples generated with $m_{DM} = 100$ GeV and $M_{med} = 100$ GeV. Ratios of the normalized distributions are shown for A-V over V-V and for V-A over A-A. A_{300} and A_{500} in the table denote the acceptance of the $\not{E}_T > 300$ GeV and $\not{E}_T > 500$ GeV cut, respectively.

447 *Scan over the couplings*   To study the dependence of kinematic dis-
448 tributions on the coupling strength, samples were generated where
449 a pair of $m_{DM} = 10$ GeV Dark Matter particles is produced on-
450 shell from the mediator of $M_{med} = 1$ TeV. Figure 2.6 compares
451 the shapes of the $\not{E}_T$ distribution for the different choices of the
452 coupling strength. This is a generator-level prediction with no kine-
453 matic selections or detector simulation. Coupling values in the scan
454 range 0.1–1.45, fixing $g_q = g_{DM}$, correspond to a rough estimate
455 of the lower sensitivity of mono-jet analyses and a maximum cou-
456 pling value such that $\Gamma_{min} < M_{med}$. We observe that the shapes of
457 the $\not{E}_T$ or jet p_T distributions do not depend on the couplings (and
458 consequently the width) in the ranges considered. A large width of
459 the mediator implies a broad integral over the contributing parton
460 distributions, which might not be well approximated by the mid-
461 point of this integral. This study shows that the effect, in the p_T
462 distribution of the observed gluon, is not important.

463   Based on similar findings for different choices of M_{med} and
464 m_{DM}, we conclude that the shapes of kinematic distributions are
465 not altered by coupling variations, neither for the on-shell Dark
466 Matter production where $M_{med} > 2m_{DM}$, nor for the off-shell Dark
467 Matter production where $M_{med} < 2m_{DM}$. Only the production cross
468 sections change. Differences in kinematic distributions are expected
469 only close to the transition region where both on-shell and off-shell
470 decays occur.

471   Special care needs to be taken when coupling strengths are com-
472 bined with extremely heavy mediators. Figure 2.7 suggests a change
473 in the shape of the $\not{E}_T$ distribution for a $M_{med} = 5$ TeV medi-
474 ator once Γ_{min}/M_{med} is of the order of a percent or lower. Such
475 heavy mediators, although inacessible by the LHC data, are inter-
476 esting since they provide a good approximation for benchmark
477 EFT models. The observed difference among the simplified mod-
478 els in the plot arises from the fact that the region of low invariant

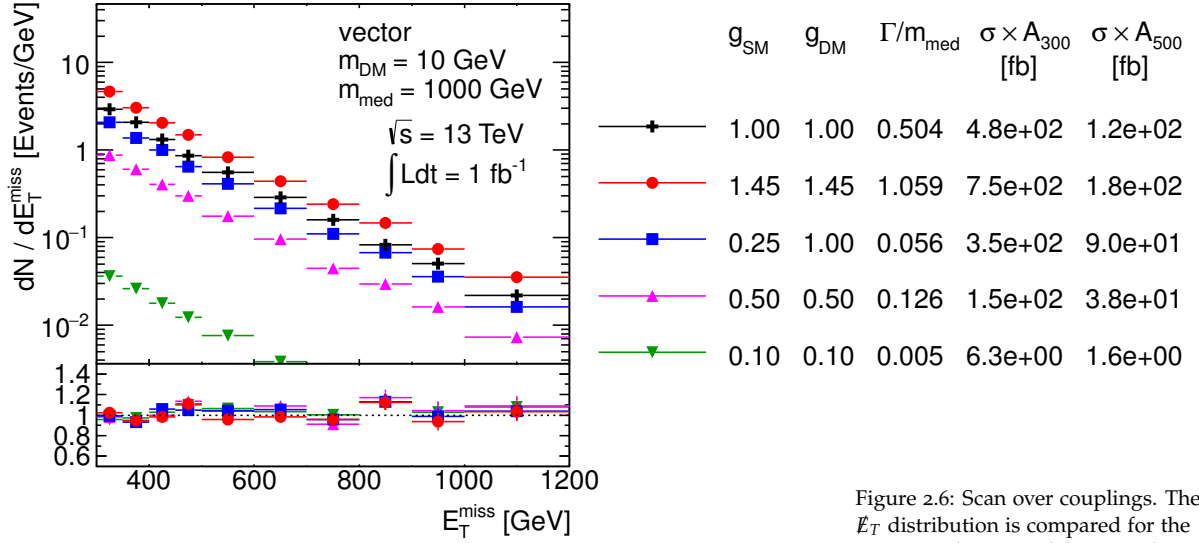|	g_{SM}	g_{DM}	Γ/m_{med}	$\sigma \times A_{300}$ [fb]	$\sigma \times A_{500}$ [fb]
+	1.00	1.00	0.504	4.8e+02	1.2e+02
●	1.45	1.45	1.059	7.5e+02	1.8e+02
■	0.25	1.00	0.056	3.5e+02	9.0e+01
▲	0.50	0.50	0.126	1.5e+02	3.8e+01
▼	0.10	0.10	0.005	6.3e+00	1.6e+00

Figure 2.6: Scan over couplings. The $\not{E}_T$ distribution is compared for the vector mediator models using the parameters as indicated. Ratios of the normalized distributions with respect to the first one are shown. A_{300} and A_{500} in the table denote the acceptance of the $\not{E}_T > 300$ GeV and $\not{E}_T > 500$ GeV cut, respectively.

masses of the Dark Matter pair, $m_{\bar{\chi}\chi}$, is suppressed due to narrow Breit-Wigner peak that only probes a narrow window of parton distribution functions. For wider mediators, the low mass region is significantly enhanced by parton distribution functions at low Bjorken x, as illustrated in Fig. 2.8(a). This explains why the sample with the narrowest mediator in Fig. 2.7 is heavily suppressed in terms of production cross section and also gives different $\not{E}_T$ shape. Furthermore, Fig. 2.7 compares the vector model with 5 TeV mediator to the D5 EFT sample and reveals that the simplified models with larger mediator widths (e.g. for couplings of 1 where $\Gamma_{min}/M_{med} \sim 0.5$) are the ones resembling the kinematics of contact interactions. This is because the production in the EFT model is always off-shell, i.e. no peak in the $m_{\bar{\chi}\chi}$ distribution is present. In case of narrow width mediators, e.g. $\Gamma_{min}/M_{med} \sim 0.05$, even larger mediator masses need to be chosen in order to significantly suppress the peak in the $m_{\bar{\chi}\chi}$ distribution and reproduce the kinematic shapes of an EFT model. Figure 2.8(b) verifies that the choice of 10 TeV mediator mass is sufficient to achieve that.

Since kinematic distributions are robust to changes in the specific values of coupling as long as heavy narrow mediators are avoided, the choice of $g_q = g_{DM}$ is reasonable to reduce the parameter space to be scanned. There are no complications associated with small couplings, but, also, the early part of Run 2 will not be sensitive to them. The range of couplings we recommend limit the calculated width of the mediator to be near or below M_{med}.

For direct mediator searches, such as $q\bar{q} \to Z' \to q\bar{q}$, asymmetric couplings ($g_q \neq g_{DM}$) might also be considered. A scan in g_{DM} vs g_q can then be performed for a fixed mediator mass. Such searches may restrict g_q to a greater degree than g_{DM}.

Scan over m_{DM}   For a fixed mediator mass M_{med} and couplings, the Dark Matter mass falls into three regimes:

g_{SM}	g_{DM}	Γ/m_{med}	$\sigma \times A_{300}$ [fb]	$\sigma \times A_{500}$ [fb]
EFT (Λ = 5 TeV)			6.1e-01	1.7e-01
0.10	0.10	0.005	7.3e-04	2.6e-04
0.50	0.50	0.126	6.9e-02	2.1e-02
1.00	1.00	0.504	6.6e-01	1.9e-01
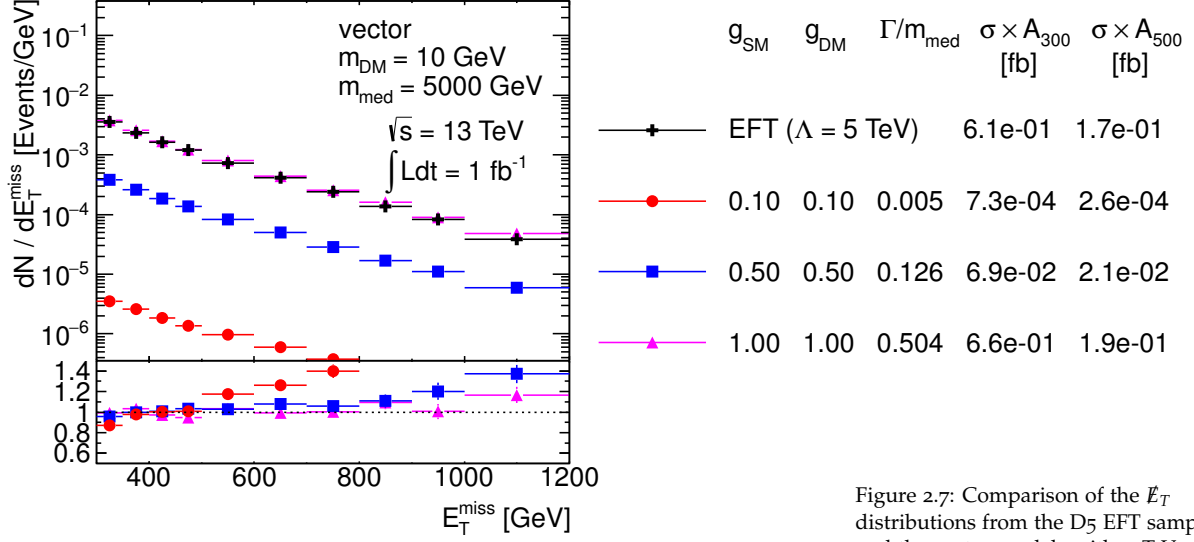
Figure 2.7: Comparison of the $\not{E}_T$ distributions from the D5 EFT sample and the vector models with 5 TeV heavy mediator of various widths. Ratios of the normalized distributions with respect to the first one are shown. A_{300} and A_{500} in the table denote the acceptance of the $\not{E}_T > 300$ GeV and $\not{E}_T > 500$ GeV cut, respectively.

(a)

(b)
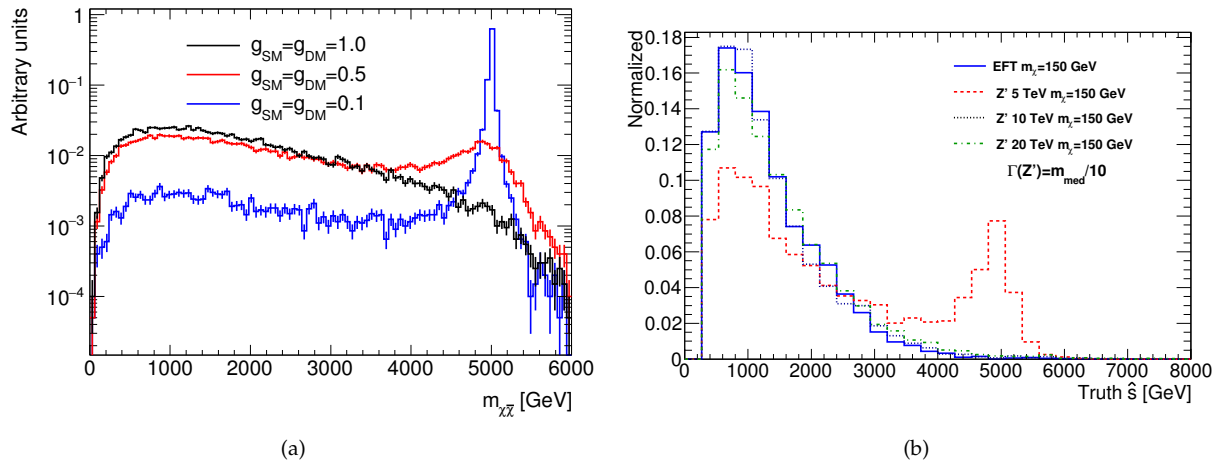
Figure 2.8: Invariant mass of the Dark Matter pair in the vector mediator samples with $m_{DM} = 10$ GeV, $M_{med} = 5$ TeV and different coupling strengths (a). Similar comparison is shown for the samples with different mediator masses considering $\Gamma_{min}/M_{med} = 0.05$ (b). An EFT sample is also displayed in the latter case. The distributions are normalised to unit area.

510 On-shell: When $M_{\mathrm{med}} \gg 2m_{\mathrm{DM}}$, most mediators are produced on-
511 shell. The hardness of the ISR is set by M_{med}, and the kinematic
512 distributions do not strongly depend on m_{DM}. This is illustrated
513 in Fig. 2.9 for an example of M_{med} =1 TeV 10 GeV $< m_{\mathrm{DM}} <$
514 300 GeV. The cross section decreases as the m_{DM} approaches
515 $M_{\mathrm{med}}/2$. A coarse binning along m_{DM} is sufficient.

516 Threshold: When $M_{\mathrm{med}} \approx 2m_{\mathrm{DM}}$, the production is resonantly
517 enhanced, and both the cross section and kinematic distributions
518 change more rapidly as a function of the two masses, and finer
519 binning is needed in order to capture the changes.

520 Off-shell: When $M_{\mathrm{med}} ll 2m_{\mathrm{DM}}$, the Dark Matter pair is produced
521 off-shell. The mediator propagator gives an explicit suppression
522 of $(M_{\mathrm{med}}/Q)^4$ that suppresses hard ISR. The $m_{\mathrm{DM}} = 1$ TeV
523 case, shown in Fig. 2.9, and Figure 2.10 demonstrates that the
524 $\not{E}_T$ spectrum hardens with increasing m_{DM}, accompanied by
525 the gradual decrease of the cross section. Due to the significant
526 cross section suppression, it is not necessary to fully populate the
527 parameter space. Imminent LHC searches are not expected to be
528 sensitive to these signals.

m_{DM} [GeV]	Γ/m_{med}	$\sigma \times A_{300}$ [fb]	$\sigma \times A_{500}$ [fb]
10	0.504	4.8e+02	1.2e+02
30	0.504	4.9e+02	1.2e+02
100	0.504	4.8e+02	1.2e+02
300	0.502	3.8e+02	1.0e+02
1000	0.477	2.4e+00	7.9e-01

Figure 2.9: Scan over Dark Matter mass. The $\not{E}_T$ distribution is compared for the vector mediator models using the parameters as indicated. Ratios of the normalized distributions with respect to the first one are shown. A_{300} and A_{500} in the table denote the acceptance of the $\not{E}_T > 300$ GeV and $\not{E}_T > 500$ GeV cut, respectively.

529 *Scan over the mediator mass* Changing the mediator mass for fixed
530 Dark Matter mass and couplings leads to significant differences
531 in cross section and shapes of the kinematic variables for on-shell
532 production, as shown in Fig. 2.11. As expected, higher mediator
533 masses lead to harder $\not{E}_T$ spectra. On the other hand, the $\not{E}_T$ shapes
534 are similar in the off-shell Dark Matter production regime. This

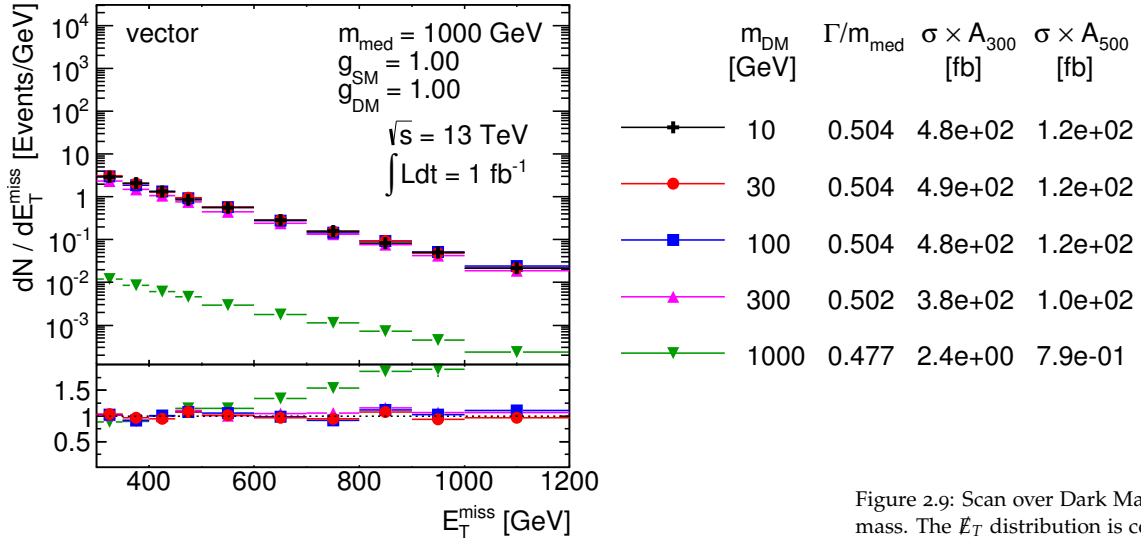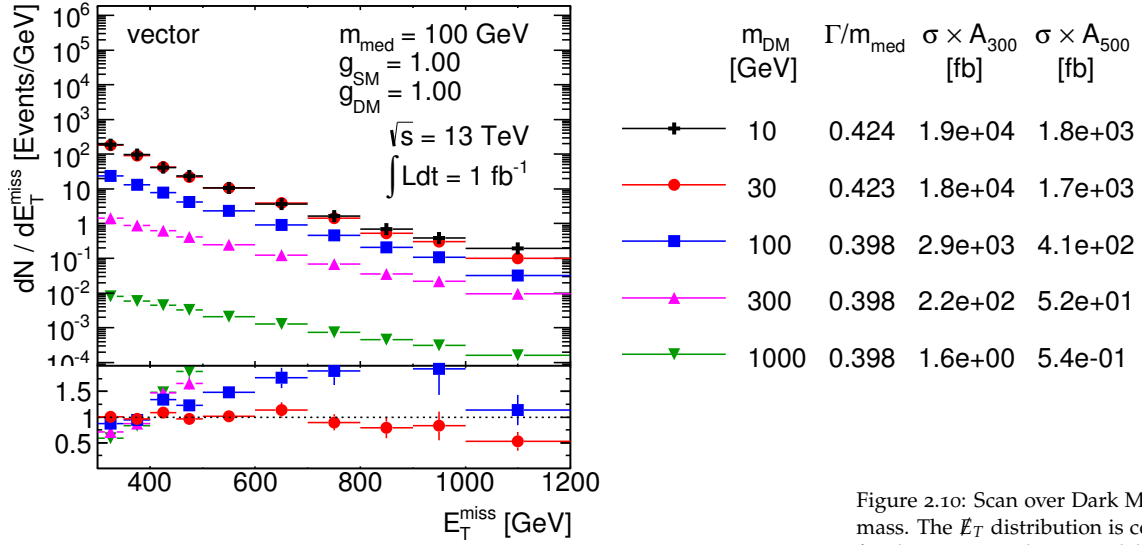| m_{DM} [GeV]	Γ/m_{med}	$\sigma \times A_{300}$ [fb]	$\sigma \times A_{500}$ [fb]
10	0.424	1.9e+04	1.8e+03
30	0.423	1.8e+04	1.7e+03
100	0.398	2.9e+03	4.1e+02
300	0.398	2.2e+02	5.2e+01
1000	0.398	1.6e+00	5.4e-01

Figure 2.10: Scan over Dark Matter mass. The $\not{E}_T$ distribution is compared for the vector mediator models using the parameters as indicated. Ratios of the normalized distributions with respect to the first one are shown. A_{300} and A_{500} in the table denote the acceptance of the $\not{E}_T > 300$ GeV and $\not{E}_T > 500$ GeV cut, respectively.

is illustrated in Fig. 2.12. Therefore, a coarse binning in M_{med} is sufficient in the off-shell regime.

Proposed parameter grid The final step in proposing a parameter grid is to evaluate the sensitivity of Run-2 LHC data with respect to rate and/or kinematics. The parameter scan focuses on two important regions, the light mediator region and the heavy mediator limit to reproduce the EFT limit, and takes into account the projected sensitivities for the mono-jet analysis.

Considering simplified models also allows to discuss constraints from different search channels. In the case of the *s*-channel exchange, the results from the mono-jet final states, where the mediator decays to a DM pair, one can also take into account dijet constraints on the processes where the mediator decays back to Standard Model particles. The importance of the dijet results depend on the magnitude of the coupling g_q. We recommend to keep the two channels rather independent by choosing $g_q = 0.25$ and $g_{DM} = 1$, based on the findings given in Ref. **??**. Furthermore, it is also important to mention this choice leads to $\Gamma_{min}/M_{med} \lesssim 0.06$. Note that the usual choice of $g_q = g_{DM} = 1$ used in literature leads to $\Gamma_{min}/M_{med} \sim 0.5$, which makes the applicability of the narrow with approximation questionable.

Projected sensitivities for a 14 TeV mono-jet analysis are available from ATLAS [ATL14d]. The expected upper limit at 95% confidence level on the product of cross section, acceptance and efficiency, $\sigma \times A \times \epsilon$, in the final Run-1 ATLAS mono-jet analysis [ATL15d] is 51 fb and 7.2 fb for $\not{E}_T > 300$ GeV and $\not{E}_T > 500$ GeV, respectively. ATLAS estimates a factor of two increase

m_{med} [GeV]	Γ/m_{med}	$\sigma \times A_{300}$ [fb]	$\sigma \times A_{500}$ [fb]
100	0.424	1.9e+04	1.8e+03
1000	0.504	4.8e+02	1.2e+02

Figure 2.11: Scan over mediator mass. The $\not{E}_T$ distribution is compared for the vector mediator models using the parameters as indicated. Ratios of the normalized distributions with respect to the first one are shown. A_{300} and A_{500} in the table denote the acceptance of the $\not{E}_T > 300$ GeV and $\not{E}_T > 500$ GeV cut, respectively.

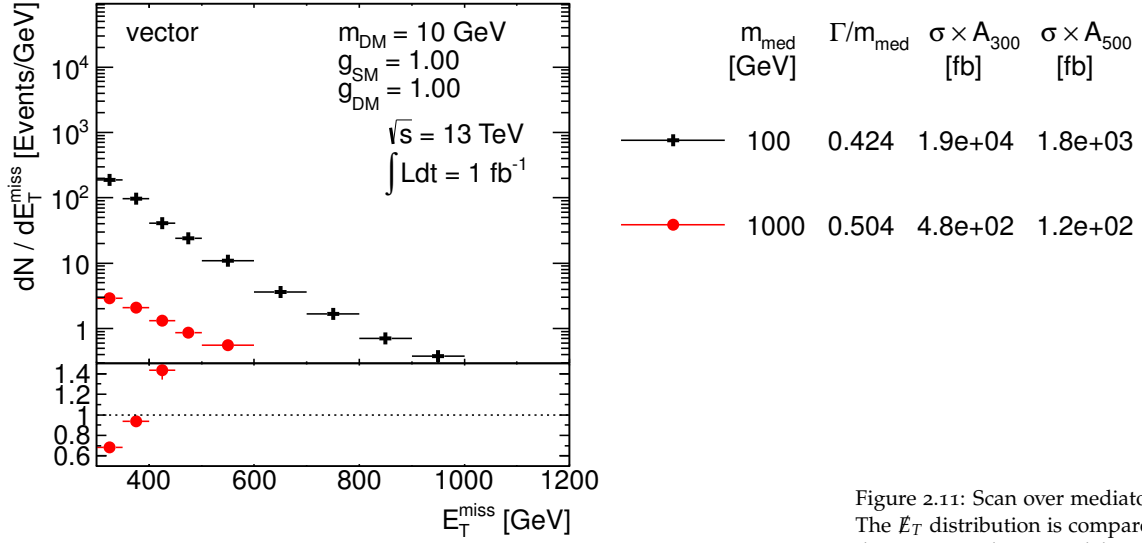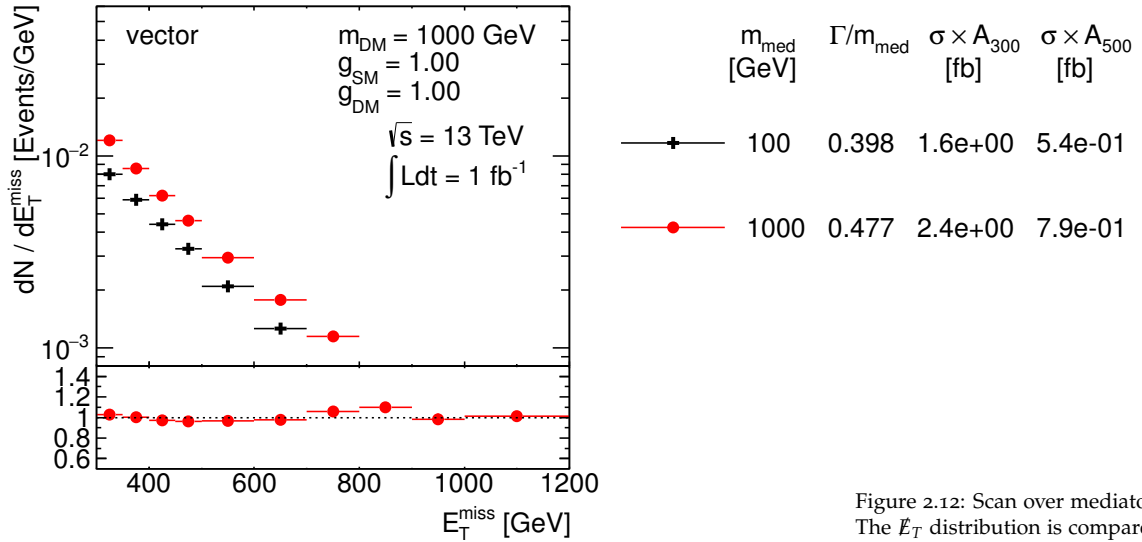| m_{med} [GeV]	Γ/m_{med}	$\sigma \times A_{300}$ [fb]	$\sigma \times A_{500}$ [fb]
100	0.398	1.6e+00	5.4e-01
1000	0.477	2.4e+00	7.9e-01

Figure 2.12: Scan over mediator mass. The $\not{E}_T$ distribution is compared for the vector mediator models using the parameters as indicated. Ratios of the normalized distributions with respect to the first one are shown. A_{300} and A_{500} in the table denote the acceptance of the $\not{E}_T > 300$ GeV and $\not{E}_T > 500$ GeV cut, respectively.

in sensitivity with the 2015 data. Given that cross section for V+jets processes increases by roughly a factor 2 when going from $\sqrt{s} = 8$ TeV to 13 TeV, similar fiducial cross section limits can be expected with the first Run-2 data as from the final Run-1 analysis. The generator level cross section times the acceptance at $\not{E}_T > 500$ GeV for the model with couplings $g_q = 0.25$ and $g_{DM} = 1$, a light Dark Matter particle of m_{DM} =10 GeV and a M_{med} =1 TeV vector mediator is at the order of 100 fb, i.e. the early Run-2 mono-jet analysis is going to be sensitive to heavier mediators than this. The value of $\sigma \times A$ at $\not{E}_T > 500$ GeV for 5 TeV vector mediator is at the order of 0.1 fb, therefore this model lies beyond the reach of the LHC in the early Run 2. However, models with high enough mediators are still useful to reproduce the EFT result.

Following these arguments, M_{med} grid points are chosen, roughly equidistant in a logarithmic scale: 10 GeV, 20 GeV, 50 GeV, 100 GeV, 200 GeV, 300 GeV, 500 GeV, 1000 GeV and 2000 GeV. In the threshold regime $M_{med} = 2m_{DM}$, the m_{DM} grid points are taken at approximately $M_{med}/2$, namely: 10 GeV, 50 GeV, 150 GeV, 500 GeV and 1000 GeV. Points on the on-shell diagonal are always chosen to be 5 GeV away from the threshold, to avoid numerical instabilities in the event generation. The detailed studies of the impact of the parameter changes on the cross section and kinematic distributions presented earlier in this section support removing some of the grid points and relying on interpolation. The optimized grids proposed for the vector and axial-vector mediators are given in Table. 2.1. One point at very high mediator mass (10 TeV) is added for each of the DM masses scanned, to aid the reinterpretation of results in terms of contact interaction operators (EFTs), as discussed in Section 4.2.

m_{DM} / GeV	M_{med} / GeV									
1	10	20	50	100	200	300	500	1000	2000	10000
10	10	15	50	100						10000
50	10		50	95	200	300				10000
150	10				200	295	500	1000		10000
500	10						500	995	2000	10000
1000	10							1000	1995	10000

Table 2.1: Simplified model benchmarks for s-channel simplified models (spin-1 mediators decaying to Dirac DM fermions in the V and A case, taking the minimum width for $g_q = 0.25$ and $g_{DM} = 1$)

The presentation of the results in the g_q–g_{DM} plane for fixed masses benefits from cross section scaling and is discussed in Section 2.5.

2.1.3   *Additional considerations for V+$\not{E}_T$ signatures*

All models detailed in this Section are applicable to signatures where a photon, a W boson, a Z boson or a Higgs boson is radiated from the initial state partons instead of a gluon. The experimental signature is identified as V+$\not{E}_T$ and it has been studied in Refs. [].

Monojet searches are generally more sensitive with respect to final states including bosons, due to the much larger rates of signal

To do **Add experimental citations. (??)**

To do **Add link to section describing EW bosons from a blob. CD: why here? (??)**

events featuring quark or gluon radiation with respect to radiation of bosons [ZBW13], in combination with the low branching ratios if leptons from boson decays are required in the final state. The rates for the Higgs boson radiation is too low for these models to be considered a viable benchmark [CDM$^+$14]. However, the presence of photons, leptons from W and Z decays, and W or Z bosons decaying hadronically allow backgrounds to be rejected more effectively, making Z/gamma/W+$\not{E}_T$ searches still worth comparing with searches in the jet+$\not{E}_T$ final state.

In the case of a spin-1 mediator, an example Feynman diagram for these processes can be constructed by taking Fig. 2.1 and replacing the gluon with γ, W or Z.

When the initial state radiation is a $W^\pm$ boson, Run 1 searches have considered three benchmark cases adapted from the vector interaction in Ref. [BT13], distinguished by ξ, the strength of the d quark coupling relative the u quark coupling:

$\xi = 0$: Mediator couples to up-type or down-type quarks, but not both;

$\xi = 1$: Mediator couples to up-type and down-type quarks with same strength;

$\xi = -1$: Mediator couples to up-type and down-type quarks with same strength, but opposite sign.

Contemplation of $\xi = -1$ heightened interest in searches for spin-1 mediators with $W^\pm$ bosons in the final state. This choice enhances the cross-section significantly above the other choices and hardens the distribution of missing transverse energy used in the searches. The sensitivity of the $W + \not{E}_T$ search then surpasses that of the jet+$\not{E}_T$ search. However, the situation $\xi = -1$ does not appear in an SU(2)-gauge-invariant simplified model.[2] The simplified model with a vector mediator exchanged in the s-channel model is still viable when $\xi = 1$. Ref. [BCD$^+$15] discusses the viability of departures $\xi < 1$ from both gauge-invariance and experimental points of view. An example of a model that arranges different effective DM couplings to u_L and d_L is detailed in Appendix B.

As in the case of the jet+$\not{E}_T$ models, the width does not have a significant impact on the kinematic distributions relevant for those searches. An example of the particle-level analysis acceptance using the generator-level cuts from Ref. [ATL15c] for the photon+$\not{E}_T$ analysis, but raising the photon p_T cut to 150 GeV, is shown in Figure 2.2, comparing a width that is set to $\Gamma = M_{med}/3$ to the minimal width (the ratio between the two widths ranges from 1.05 to 1.5 with increasing mediator masses).

Examples of relevant kinematic distributions for selected benchmark points are shown in Fig. 2.13. Leading-order cross-sections for the chosen benchmark points are shown in Appendix B.

In addition, for the vector models considered, initial and final state radiation of a Z' can occur which can appear as a narrow jet if

[2] It is well-known that the diagrams in which the W couples to u and $\bar{d}$ have opposite sign. This is what gives rise to the "helciity zero" in $u\bar{d} \to Wg$. The relative sign is set by SU(2) and the statement that the mediator is an SU(2) singlet. We can increase the cross section by changing the sign, but to do so we have to give the mediator some SU(2) quantum number, making it, and the associated χ, visible.

| Acceptance ratio for $\Gamma = \Gamma_{\min}$ vs $\Gamma = M_{\mathrm{med}}/3$				
	$m_{\mathrm{DM}}/\mathrm{GeV}$			
$M_{\mathrm{med}}/\mathrm{GeV}$	10	50	200	400
50	0.96	0.99		0.95
100	0.97			
300	1.00	1.02		
600			0.96	
1000	1.01	1.02	1.03	
3000	1.02	1.03		1.01

Table 2.2: Analysis acceptance ratios for the photon+$\not{E}_T$ analysis when varying the mediator width, in the case of a vector mediator exchanged in the s-channel
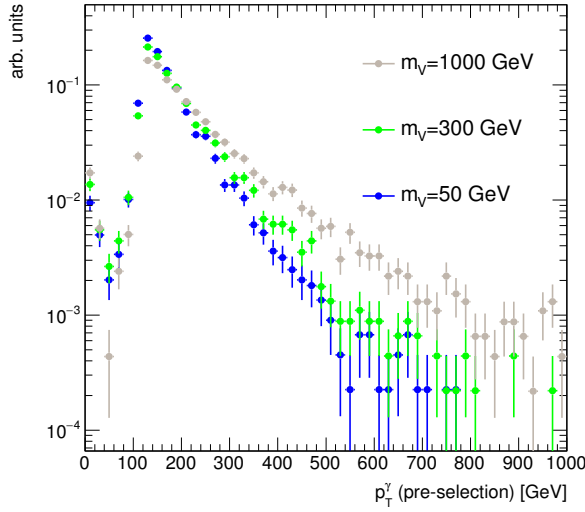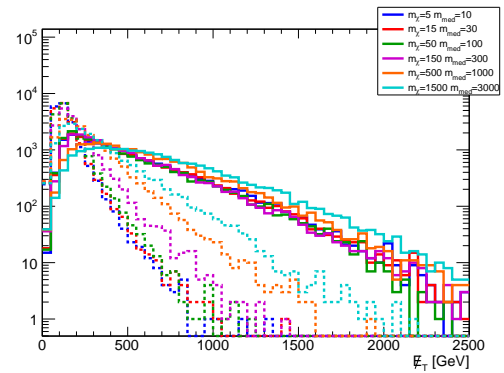

(a) Missing transverse momentum distribution for the photon+$\not{E}_T$ final state, for different mediator mass choices, for $m_{\mathrm{DM}} = 10$ GeV.
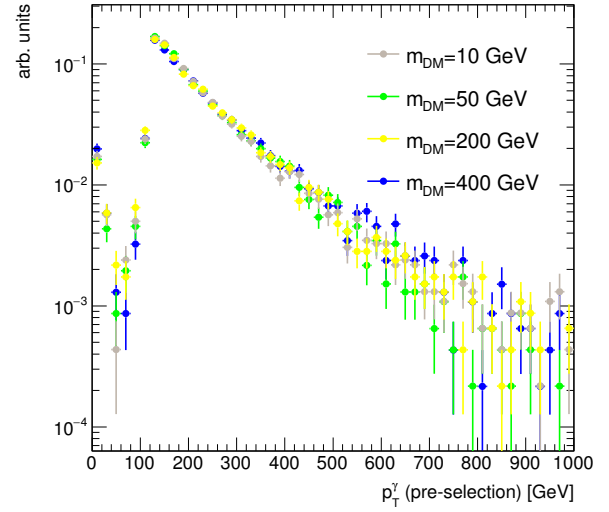
(b) Leading photon transverse momentum distribution for the photon+$\not{E}_T$ final state, for different DM mass choices, with $M_{\mathrm{med}} = 1$ TeV.
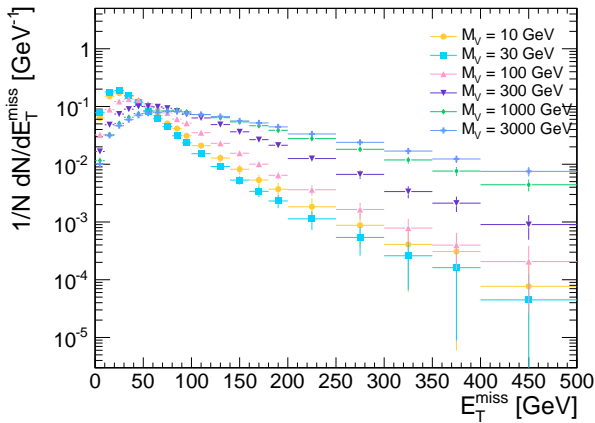
(c) Missing transverse momentum distribution for the leptonic $Z+\not{E}_T$ final state, for different mediator mass choices, for $m_{\mathrm{DM}} = 15$ GeV

(d) Missing transverse momentum distribution for the hadronic $W+\not{E}_T$ final state.

Figure 2.13: Kinematic distributions relevant for searches with W, Z and photons in the final state, for the simplified model with a vector mediator exchanged in the s-channel.

648 it decays hadronically and may not be distinguishable from a QCD
649 jet, thus accounting for some fraction of the monojet signal. The
650 ISR and FSR of Z' becomes more important at large values of the
651 couplings [?].

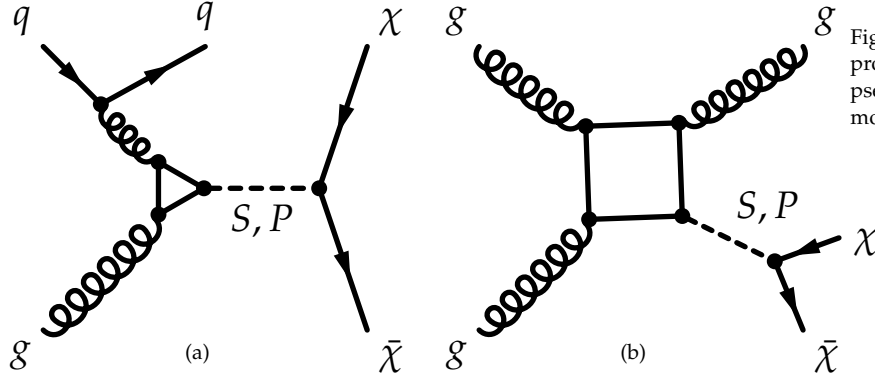## 2.2   Scalar and pseudoscalar mediator, s-channel exchange

Figure 2.14: One-loop diagrams of processes exchanging a scalar (*S*) or pseudoscalar (*P*) mediator, leading to a mono-jet signature.

In this section, we consider a parallel situation to the vector and axial-vector mediators in the previous sections: a real scalar or a pseudoscalar where the associated scalar is decoupled at higher energies[3]. This section is largely based on Refs. [BFG15, HKSW15] which contain a thorough discussion of these models.

Assuming MFV, spin-0 resonances behave in a similar fashion as the SM Higgs boson. Relative to the vector and axial-vector models discussed above, the scalar models are distinguished by the special consequences of the MFV assumption: the very narrow width of the mediator and its extreme sensitivity to which decays are kinematically available, and the loop-induced coupling to gluons. The interaction Lagrangians are

$$\mathcal{L}_\phi = g_{\mathrm{DM}}\phi\bar{\chi}\chi + \frac{\phi}{\sqrt{2}}\sum_i \left(g_u y_i^u \bar{u}_i u_i + g_d y_i^d \bar{d}_i d_i + g_\ell y_i^\ell \bar{\ell}_i \ell_i\right), \tag{2.6}$$

$$\mathcal{L}_a = i g_{\mathrm{DM}} a\bar{\chi}\gamma_5\chi + \frac{ia}{\sqrt{2}}\sum_i \left(g_u y_i^u \bar{u}_i \gamma_5 u_i + g_d y_i^d \bar{d}_i \gamma_5 d_i + \right.$$

$$\left. g_\ell y_i^\ell \bar{\ell}_i \gamma_5 \ell_i\right). \tag{2.7}$$

where ϕ and a are respectively the scalar and pseudoscalar mediators, and the Yukawa couplings y_i^f are normalized to the Higgs vev as $y_i^f = \sqrt{2}m_i^f/v$.

The couplings to fermions are proportional to the SM Higgs couplings, yet one is still allowed to adjust an overall strength of the coupling to charged leptons and the relative couplings of *u*- and *d*-type quarks. As in the preceding sections, for the sake of simplicity and straightforward comparison, we reduce the couplings to the SM fermions to a single universal parameter $g_{\mathrm{q}} \equiv g_u = g_d = g_\ell$. Unlike the vector and axial-vector models, the scalar mediators are allowed to couple to leptons.[4]

The relative discovery and exclusion power of each search can be compared in this framework. However, we again emphasize the importance of searching the full set of allowed channels in case violations of these simplifying assumptions lead to significant modifications of the decay rates that unexpectedly favor different channels

[3] This assumption does not hold in a UV-complete model where the two components of the complex scalar mediator would be approximately degenerate. The complex scalar case could be studied separately in the case of heavy flavor final states given the sufficiently different kinematics.

[4] This contribution plays no role for most of the parameter space considered. The choice to allow lepton couplings follows Refs. [BFG15, HKSW15].

than the mix obtained under our assumptions. The coupling g_{DM} parameterizes the entire dependence on the structure between the mediator and the dark sector.

Given these simplifications, the minimal set of parameters under consideration is

$$\left\{ m_{\text{DM}}, \; m_{\phi/a} = M_{\text{med}}, \; g_{\text{DM}}, \; g_{\text{q}} \right\} . \tag{2.8}$$

Fig. 2.14 shows the one-loop diagrams producing a jet+X signature. The full calculation of the top loop is available at LO for DM pair production in association with one parton.

The minimal mediator width is given by

$$\Gamma_{\phi,a} = \sum_f N_c \frac{y_f^2 g_q^2 m_{\phi,a}}{16\pi} \left(1 - \frac{4m_f^2}{m_{\phi,a}^2} \right)^{x/2} + \frac{g_{\text{DM}}^2 m_{\phi,a}}{8\pi} \left(1 - \frac{4m_{\text{DM}}^2}{m_{\phi,a}^2} \right)^{x/2}$$
$$+ \frac{\alpha_s^2 y_t^2 g_q^2 m_{\phi,a}^3}{32\pi^3 v^2} \left| f_{\phi,a} \left(\frac{4m_t^2}{m_{\phi,a}^2} \right) \right|^2 \tag{2.9}$$

where $x = 3$ for scalars and $x = 1$ for pseudoscalars. The loop integrals are

$$f_\phi(\tau) \;\; = \;\; \tau \left[1 + (1 - \tau) \arctan^2 \left(\frac{1}{\sqrt{\tau - 1}} \right) \right] , \tag{2.10}$$

$$f_a(\tau) \;\; = \;\; \tau \arctan^2 \left(\frac{1}{\sqrt{\tau - 1}} \right) \tag{2.11}$$

for $\tau < 1$, where $\tau = 4m_t^2 / m_{\phi,a}^2$, and, for $\tau > 1$,

$$f_\phi(\tau) \;\; = \;\; \tau \left[1 + (1 - \tau) \left(-\frac{1}{4} \left(\log \frac{1 + \sqrt{1 - \tau}}{1 - \sqrt{1 - \tau}} + i\pi \right)^2 \right) \right] , \tag{2.12}$$

$$f_a(\tau) \;\; = \;\; \tau \left(-\frac{1}{4} \left(\log \frac{1 + \sqrt{1 - \tau}}{1 - \sqrt{1 - \tau}} + i\pi \right)^2 \right) . \tag{2.13}$$

The minimal widths for scalar and pseudo-scalar mediators with $g_{\text{q}} = g_{\text{DM}} = 1$ are shown in Fig. 2.15, illustrating the effect of choosing the SM Higgs-like Yukawa couplings for the SM fermions. For the mediator mass above twice the top quark mass m_t, the minimal width receives the dominant contribution from the top quark. For lighter mediator masses, Dark Matter dominates as the couplings to lighter quarks are Yukawa suppressed.

It can be seen in Fig. 2.16 that the kinematics for the scalar and pseudoscalar models coincides when considering the diagrams in Fig. 2.14. For this reason, we recommend to generate only one of the two models. No preference is given between the two models as they have the same kinematics, although it is worth noting that the pseudo-scalar model has been used for a Dark Matter interpretation of the DAMA signal and of the galactic center excess [ADNP15]. Like in the case of the vector and axial-vector models described
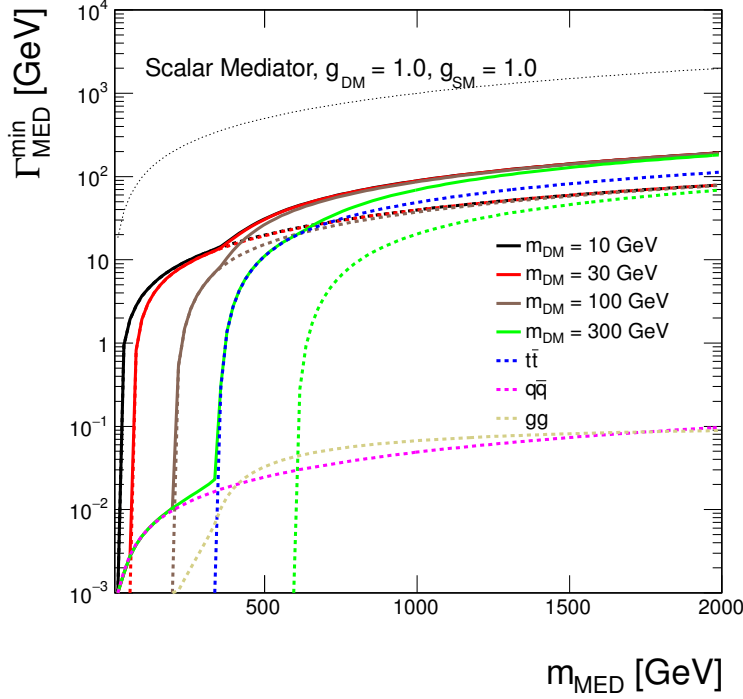
Figure 2.15: Minimal width as a function of mediator mass for scalar and pseudo-scalar mediator assuming couplings of 1. The total width is shown as solid lines for Dark Matter masses of m_{DM} =10 GeV, 30 GeV, 100 GeV and 300 GeV in black, red, brown and green, respectively. The individual contributions from Dark Matter are indicated by dotted lines with the same colors. The contribution from all quarks but top is shown as magenta dotted line and the contribution from top quarks only is illustrated by the dotted blue line. The dotted beige line shows the contribution from the coupling to gluons. The dotted black line shows the extreme case $\Gamma_{min} = M_{med}$.
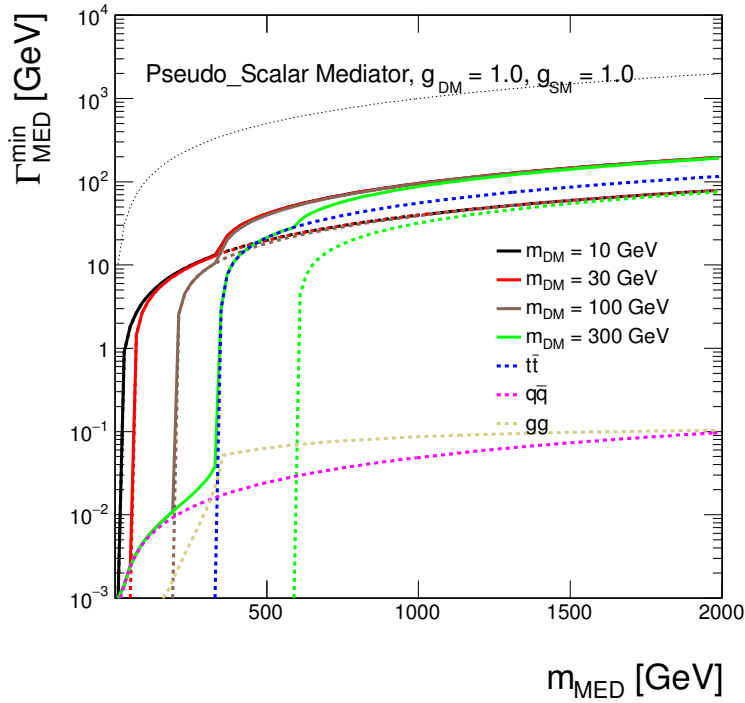
708   in Section 2.1.1, the differences between the cross sections for the
709   scalar and pseudo-scalar samples with the same m_{DM} and M_{med}
710   are increasing with the Dark Matter mass for fixed mediator mass.
711   The pseudo-scalar model gives larger cross sections. Also note the
712   increasing differences between the minimal widths close to the
713    $2m_{DM} = M_{med}$ threshold.

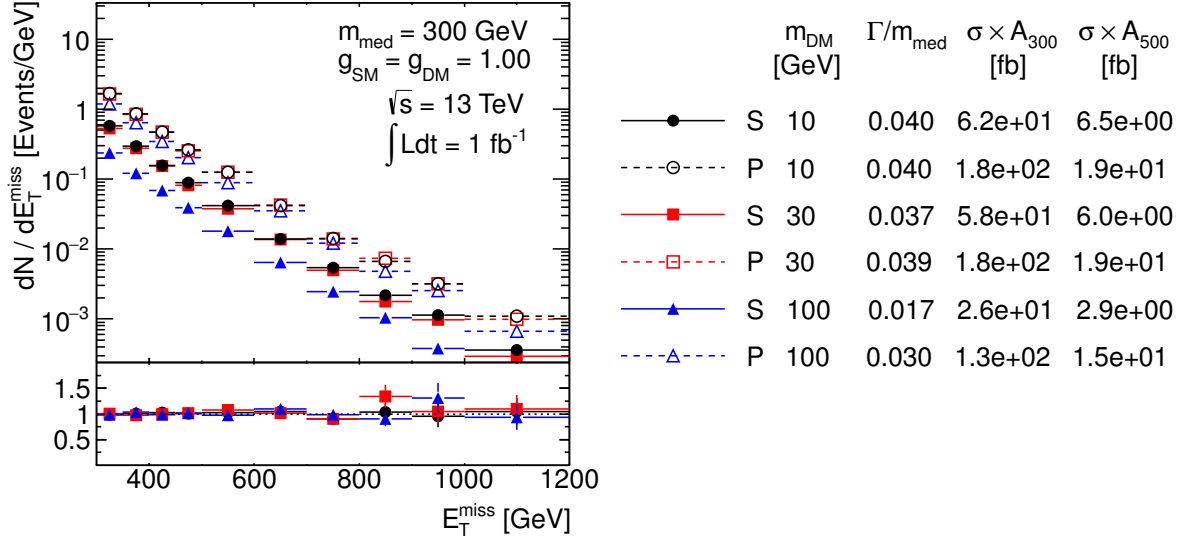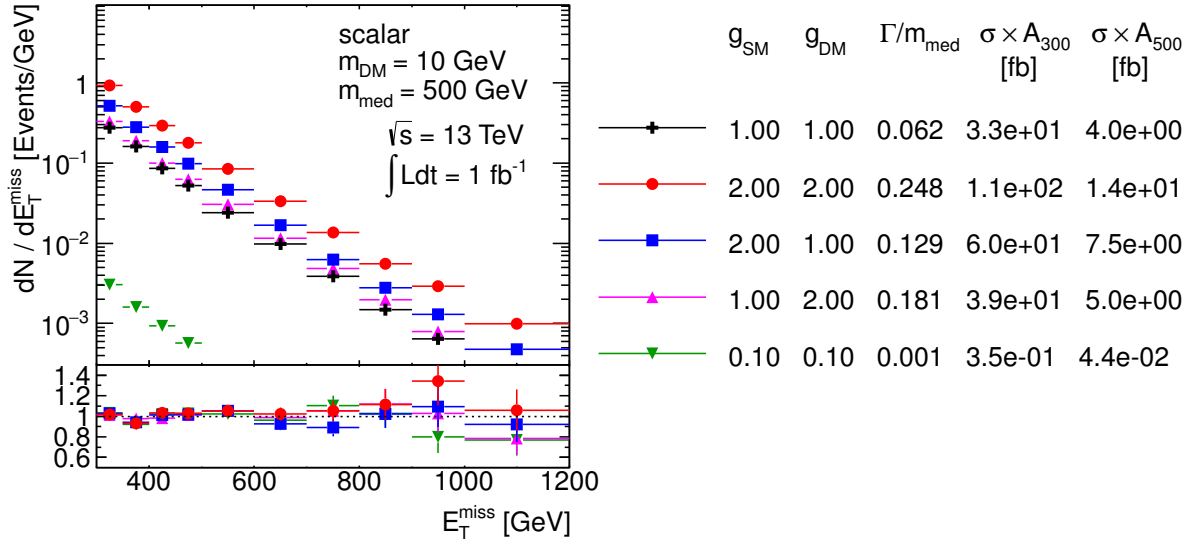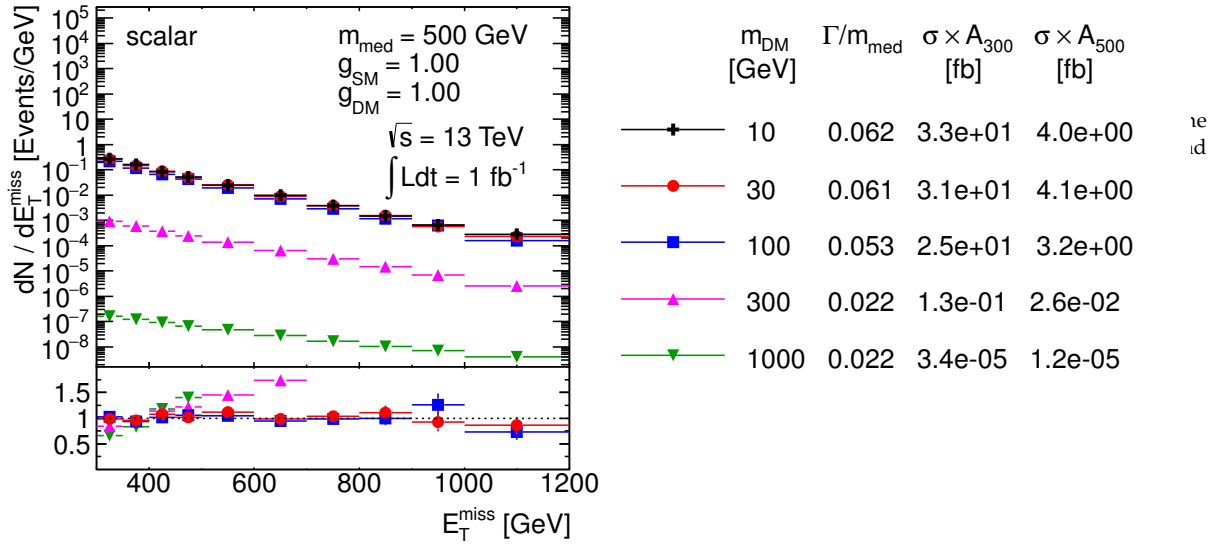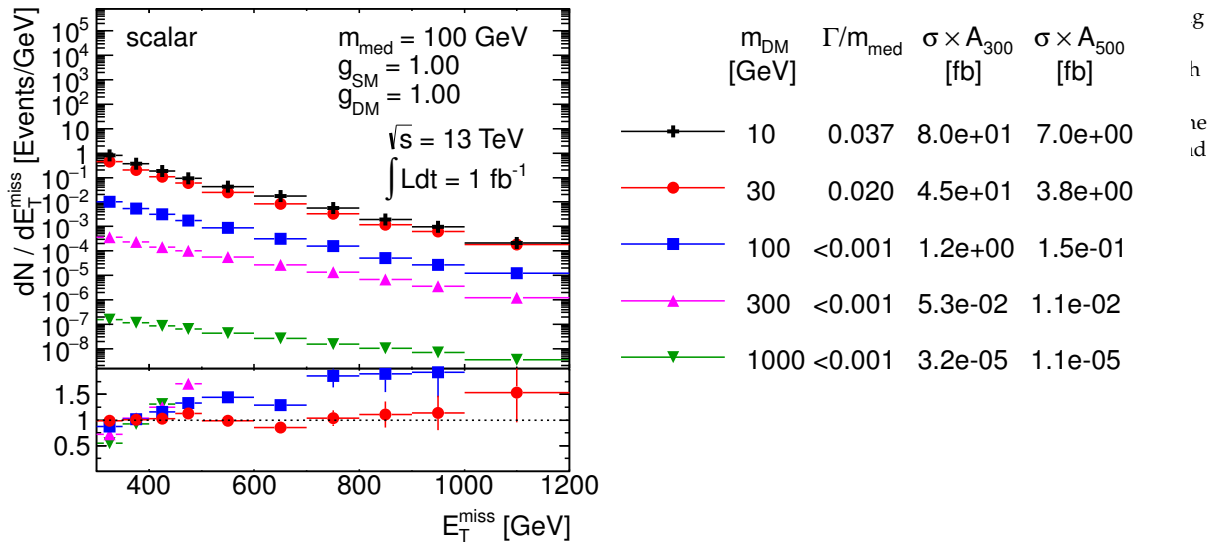| m_{DM} [GeV]	Γ/m_{med}	$\sigma \times A_{300}$ [fb]	$\sigma \times A_{500}$ [fb]
S 10	0.040	6.2e+01	6.5e+00
P 10	0.040	1.8e+02	1.9e+01
S 30	0.037	5.8e+01	6.0e+00
P 30	0.039	1.8e+02	1.9e+01
S 100	0.017	2.6e+01	2.9e+00
P 100	0.030	1.3e+02	1.5e+01

Figure 2.16: Comparison of the $\not{E}_T$ distributions for the scalar and pseudoscalar models for different $M_{med} = 300$ GeV and different Dark Matter masses. Ratios of the normalized distributions with respect to the first one are shown. A_{300} and A_{500} in the table denote the acceptance of the $\not{E}_T > 300$ GeV and $\not{E}_T > 500$ GeV cut, respectively.

714   *2.2.1   Parameter scan*

715   Similarly as in the case of the vector and axial-vector couplings of
716   spin-1 mediators, scans in the parameter space are performed also
717   for the scalar and pseudo-scalar couplings of the spin-0 mediators
718   in order to decide on the optimized parameter grid for the pre-
719   sentation of Run-2 results. Figures 2.17- 2.21 show the scans over
720   the couplings, Dark Matter mass and mediator mass and the same
721   conclusions apply as in Section 2.1.

722   A scan over the mediator mass is shown in Fig. 2.21 where M_{med}
723   = 300 GeV and 500 GeV are chosen to be below and above $2m_t$. The
724   off-shell Dark Matter production regime is assumed by taking an
725   extreme limit ($m_{DM} = 1$ TeV) in order to study solely the effects of
726   the couplings to quarks. No differences in the kinematic distribu-
727   tions are observed and also the cross sections remain similar in this
728   case. No significant changes appear for mediator masses around
729   the $2m_t$ threshold.

730   The optimized parameter grid in the M_{med}–m_{DM} plane for scalar
731   and pseudo-scalar mediators is motivated by similar arguments
732   as in the previous section. Therefore, a similar pattern is followed
733   here, taking again $g_q = 0.25$ and $g_{DM} = 1$. Only the sensitivity to
734   the highest mediator masses has to be re-evaluated. The generator
735   level cross section times the acceptance at $\not{E}_T > 500$ GeV for the
736   model with couplings $g_q = g_{DM} = 1$, light Dark Matter of m_{DM}
737   =10 GeV and a M_{med} =500 GeV scalar mediator is at the order of

g_{SM}	g_{DM}	Γ/m_{med}	$\sigma \times A_{300}$ [fb]	$\sigma \times A_{500}$ [fb]
1.00	1.00	0.062	3.3e+01	4.0e+00
2.00	2.00	0.248	1.1e+02	1.4e+01
2.00	1.00	0.129	6.0e+01	7.5e+00
1.00	2.00	0.181	3.9e+01	5.0e+00
0.10	0.10	0.001	3.5e-01	4.4e-02

Figure 2.17: Scan over couplings. The $\not{E}_T$ distribution is compared for the

m_{DM} [GeV]	Γ/m_{med}	$\sigma \times A_{300}$ [fb]	$\sigma \times A_{500}$ [fb]
10	0.062	3.3e+01	4.0e+00
30	0.061	3.1e+01	4.1e+00
100	0.053	2.5e+01	3.2e+00
300	0.022	1.3e-01	2.6e-02
1000	0.022	3.4e-05	1.2e-05

Figure 2.18: Scan over Dark Matter mass. The $\not{E}_T$ distribution is compared

m_{DM} [GeV]	Γ/m_{med}	$\sigma \times A_{300}$ [fb]	$\sigma \times A_{500}$ [fb]
10	0.037	8.0e+01	7.0e+00
30	0.020	4.5e+01	3.8e+00
100	<0.001	1.2e+00	1.5e-01
300	<0.001	5.3e-02	1.1e-02
1000	<0.001	3.2e-05	1.1e-05

Figure 2.19: Scan over Dark Matter mass. The $\not{E}_T$ distribution is compared for the scalar mediator models using the parameters as indicated. Ratios of the normalized distributions with respect to the first one are shown. A_{300} and A_{500} in the table denote the acceptance of the $\not{E}_T > 300$ GeV and

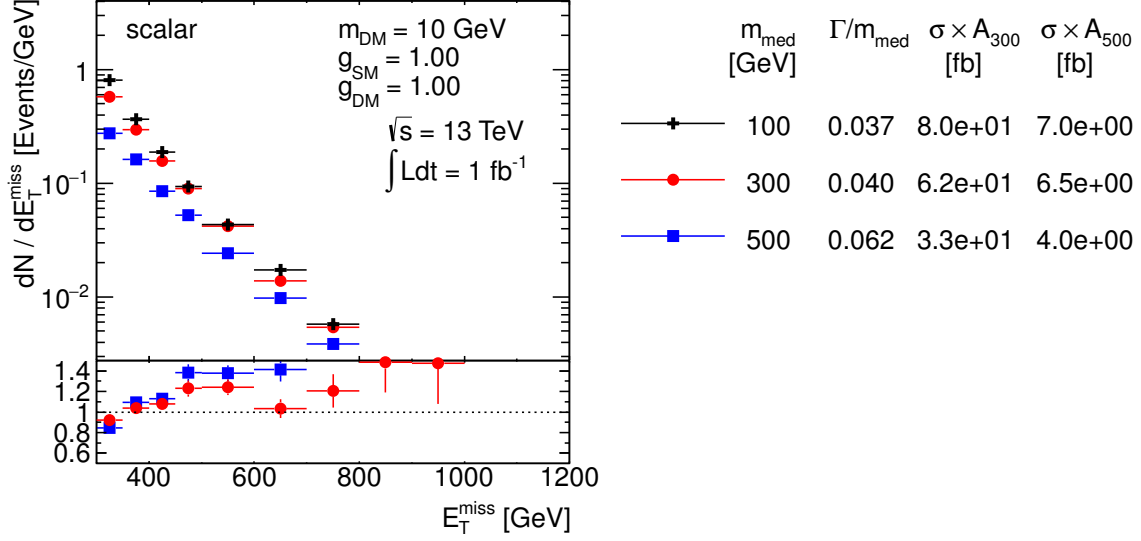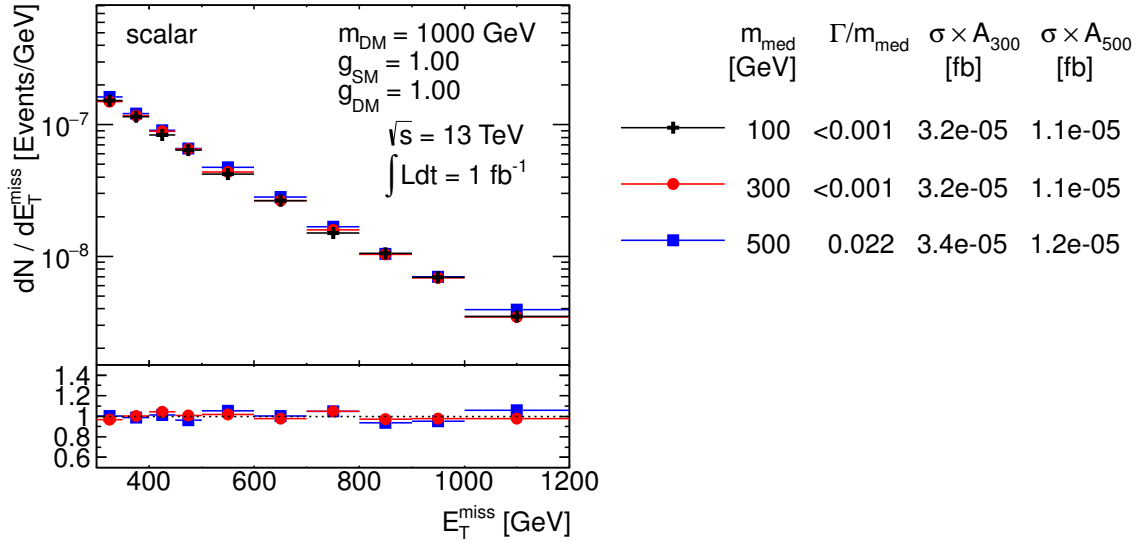| m_{med} [GeV]	Γ/m_{med}	$\sigma \times A_{300}$ [fb]	$\sigma \times A_{500}$ [fb]
100	0.037	8.0e+01	7.0e+00
300	0.040	6.2e+01	6.5e+00
500	0.062	3.3e+01	4.0e+00

Figure 2.20: Scan over mediator mass. The $\not{E}_T$ distribution is compared for the scalar mediator models using the parameters as indicated. Ratios of the normalized distributions with respect to the first one are shown. A_{300} and A_{500} in the table denote the acceptance of the $\not{E}_T > 300$ GeV and $\not{E}_T > 500$ GeV cut, respectively.

m_{med} [GeV]	Γ/m_{med}	$\sigma \times A_{300}$ [fb]	$\sigma \times A_{500}$ [fb]
100	<0.001	3.2e-05	1.1e-05
300	<0.001	3.2e-05	1.1e-05
500	0.022	3.4e-05	1.2e-05

Figure 2.21: Scan over mediator mass. The $\not{E}_T$ distribution is compared for the scalar mediator models using the parameters as indicated. Ratios of the normalized distributions with respect to the first one are shown. A_{300} and A_{500} in the table denote the acceptance of the $\not{E}_T > 300$ GeV and $\not{E}_T > 500$ GeV cut, respectively.

738 10 fb, i.e. just at the edge of the early Run-2 sensitivity. Increasing
739 the mediator mass to 1 TeV pushes the product $\sigma \times A$ down to ap-
740 proximately 0.1 fb, below the LHC sensitivity. Therefore, we choose
741 to remove the 2 TeV mediator mass from the grid and present the
742 final grid with 33 mass points only, as shown in Tab. 2.3. One point
743 at very high mediator mass (10 TeV) is added for each of the DM
744 masses scanned, to aid the reinterpretation of results in terms of
745 contact interaction operators (EFTs).

m_{DM} (GeV)	M_{med} (GeV)								
1	10	20	50	100	200	300	500	1000	10000
10	10	15	50	100					10000
50	10		50	95	200	300			10000
150	10				200	295	500	1000	10000
500	10						500	995	10000
1000	10							1000	10000

Table 2.3: Simplified model benchmarks for s-channel simplified models (spin-0 mediators decaying to Dirac DM fermions in the scalar and pseudoscalar case, taking the minimum width for $g_{\mathrm{q}} = 0.25$ and $g_{\mathrm{DM}} = 1$)

2.2.2   Additional considerations for $V + \not{E}_T$ signatures

747 The discussion of parameters for the model with a color-singlet,
748 spin-0 mediator parallels that in Section 2.
749   Even though the sensitivity of mono-boson searches to this
750 model is low and it may not be in reach of early LHC searches, we
751 recommend to generate this model for W, Z and photon searches in
752 order to reproduce the kinematics of contact interaction operators
753 that are further described in Section 3.2.1, for later reinterpretation.

2.2.3   Additional considerations for $t\bar{t}$ and $b\bar{b}+\not{E}_T$ signatures

755 With the MFV assumption, the top and possibly bottom quark can
756 play a primary role in the phenomenology. The model predicts not
757 only the monojet process described in Section 2.2, but also pro-
758 duction of dark matter in association with top (or bottom) pairs,
759 as illustrated in Fig. 2.22. Dedicated searches including jets from
760 heavy flavor quarks in the final state can be designed for this sig-
761 nature. Another class of simplified models, which includes a Dark
762 Matter interpretation among many others, and yields a single top
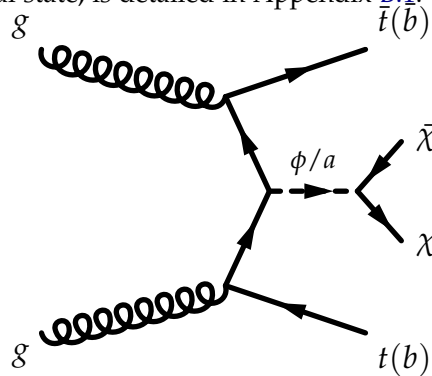763 quark in the final state, is detailed in Appendix B.1.

Figure 2.22: Representative Feynman diagram showing the pair production of dark matter particles in association with $t\bar{t}$ (or $b\bar{b}$).

764   In some theoretically motivated scenario (e.g. for high $tan\beta$

in 2HDM in the pMSSM), spin-0 mediators might couple more strongly to down generation quarks. This assumption motivates the study of final states involving b-quarks as a complementary search to the $t\bar{t}$+DM models, to directly probe the b-quark coupling. In addition to the example illustrated in Fig. 2.22, an example of such a model can be found in Ref. [BFG15]. Note that, because of the kinematics features of b quark production relative to heavy t quark production, a $b\bar{b}$+DM final state may only yield one experimentally visible b quark, leading to a mono-b signature in a model that conserves b flavor.

The parameter scan for the dedicated $t\bar{t}$+$\not{E}_T$ searches has been studied in detail to target the production mechanism of DM associated with heavy flavor quarks, still sharing many details of the scan for the scalar model with a gluon radiation The benchmark points scanning the model parameters have been selected to ensure that the kinematic features of the parameter space are sufficiently represented. Detailed studies were performed to identify points in the m_{DM}, $m_{\phi,a}$, g_{DM}, g_q (and $\Gamma_{\phi,a}$) parameter space that differ significantly from each other in terms of expected detector acceptance. Because missing transverse momentum is the key observable for searches, the mediator p_T spectra is taken to represent the main kinematics of a model. Another consideration in determining the set of benchmarks is to focus on the parameter space where we expect the searches to be sensitive during the 2015 LHC run. Based on a projected integrated luminosity of $30\,\mathrm{fb}^{-1}$ expected for 2015, we disregard model points with a cross section times branching ratio smaller than 0.1 fb, corresponding to a minimum of one expected event assuming a 0.1% signal efficiency.

The kinematics is most dependent on the masses m_{DM} and $m_{\phi,a}$. Figure 2.23 and 2.24 show typical dependencies for scalar and pseudoscalar couplings respectively. Typically, the mediator p_T spectrum broadens with larger $m_{\phi,a}$. The kinematics are also different between on-shell ($M_{\mathrm{med}} > 2m_{\mathrm{DM}}$) and off-shell ($M_{\mathrm{med}} < 2m_{\mathrm{DM}}$) mediators as discussed in Section 2.2. Furthermore, the kinematic differences in the $\not{E}_T$ spectrum between scalar and pseudoscalar are larger for light mediator masses with respect to heavier mediators. It is therefore important to choose benchmark points covering on-shell and off-shell mediators with sufficient granularity, including the transition region between on-shell and off-shell mediators.

Typically only weak dependencies on couplings are observed (see Fig 2.25) where the variation with width of the integral over parton distributions is unimportant. As shown in Section 2.1.2, for couplings $\sim O(1)$ the width is large enough that the p_T of the mediator is determined mainly by the PDF.

At large mediator masses ($\sim 1.5\,\mathrm{TeV}$) or very small couplings ($\sim 10^{-2}$), width effects are significant, but these regimes have production cross sections that are too small to be relevant for $30\,\mathrm{fb}^{-1}$ and are not studied here. However, with the full Run 2 dataset, such models may be within reach.
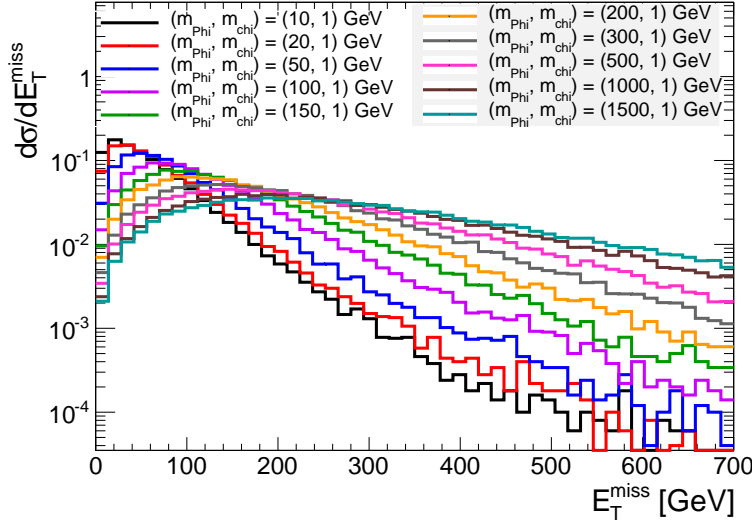
Figure 2.23: Example of the dependence of the kinematics on the scalar mediator mass. The Dark Matter mass is fixed to be m_{DM} =1GeV.
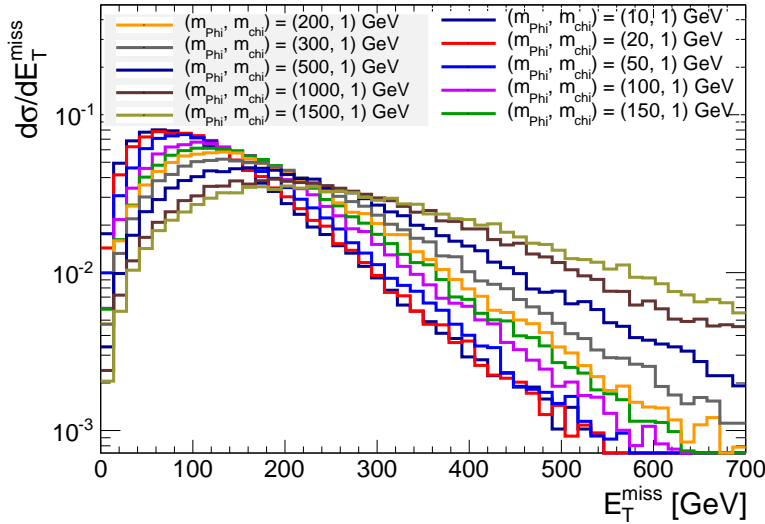

Figure 2.24: Example of the dependence of the kinematics on the pseudoscalar mediator mass. The Dark Matter mass is fixed to be m_{DM} =1GeV.

Another case where the width can impact the kinematics is when $m_{\phi,a}$ is slightly larger than $2m_\chi$. Here, the width determines the relative contribution between on-shell and off-shell mediators. An example is given in Fig. 2.26. As the minimal width choice pursued in this document is the most conservative one, this effect can be neglected in order to reduce the number of benchmark points to be generated.

The points for the parameter scan chosen for this model are listed in Table 2.3, chosen to be harmonized with those for other analyses employing the same scalar model as benchmark. Based on the sensitivity considerations above, DM masses are only simulated up to 500 GeV (but the 5 TeV mediator point is retained) leading to a total of 24 benchmark points. However for these searches we recommend to generate scalar and pseudoscalar models separately, as the kinematics differs due to the different coupling of the mediator to the final state top quarks in the two cases, as shown in Figs. 2.23
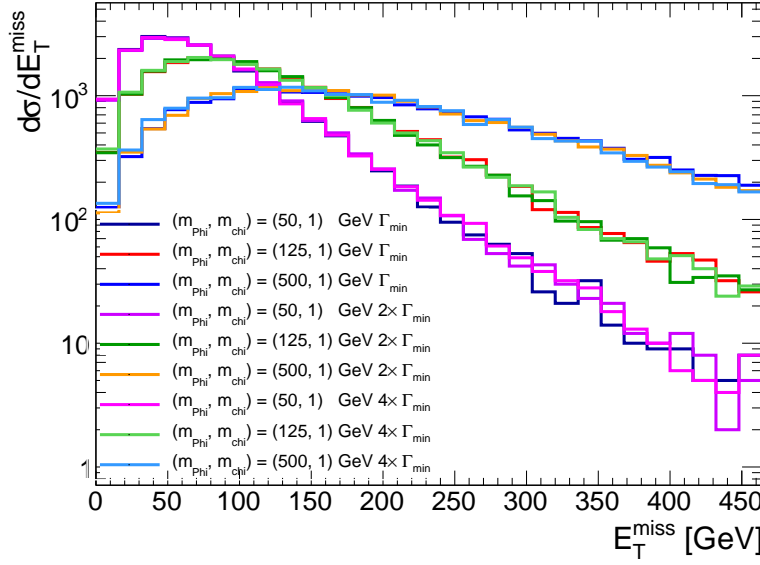
Figure 2.25: Study of the dependence of kinematics on the width of a scalar mediator. The width is increased up to four times the minimal width for each mediator and dark matter mass combination.
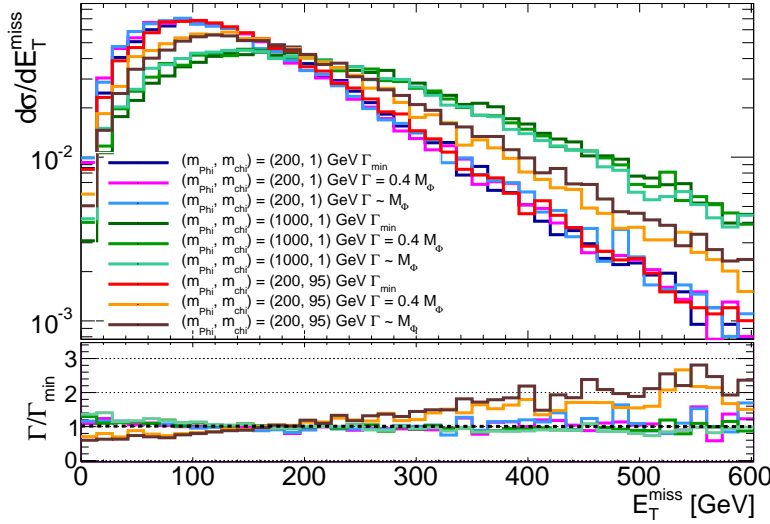

Figure 2.26: Dependence of the kinematics on the width of a scalar mediator. The width is increased up to the mediator mass. Choices of mediator and dark matter masses such that $m_{\phi,a}$ is slightly larger than $2m_\chi$ is the only case that shows a sizeable variation of the kinematics as a function of the width.

and 2.24.

Similar studies were performed in the $b\bar{b}$ case. It was found that they show the same weak dependence of the kinematics of the event on the mediator width. The same benchmark parameters of the $t\bar{t}$ case could then be chosen.

2.3 Colored scalar mediator, t-channel exchange

The preceding sections address models with a Dirac fermion coupled to the SM through exchange of a neutral spin-0 or spin-1 particle in an s-channel process. A t-channel process may couple the SM and DM directly, leading to a different phenomenology. For completeness, we examine a model where χ is a Standard Model (SM) singlet, a Dirac fermion; the mediating particle, labeled ϕ, is charged and colored; and the SM particle is a quark. Such mod-

els have been studied in Refs. [AWZ14, PVZ14, BB13, DNRT13, CEHL14, BDG⁺12]. However, this model has not been studied extensively in this forum.

Following the example of Ref. [PVZ14], the interaction Lagrangian is written as

$$\mathcal{L}_{\text{int}} = g \sum_{i=1,2} (\phi_{(i),L} \bar{Q}_{(i),L} + \phi_{(i),u,R} \bar{u}_{(i),R} + \phi_{(i),d,R} \bar{d}_{(i),R}) \chi \qquad (2.14)$$

where $Q_{(i),L}$, $u_{(i),R}$ and $d_{(i),R}$ are the SM quarks of the i-th generation and $\phi_{(i),L}$, $\phi_{(i),u,R}$ and $\phi_{(i),d,R}$ are the corresponding mediators, which (unlike the s-channel mediators) must be heavier than χ. These mediators have SM gauge representations under $(SU(3), SU(2))_Y$ of $(3,2)_{-1/6}$, $(3,1)_{2/3}$ and $(3,1)_{-1/3}$ respectively. Variations of the model previously studied in the literature include coupling to the left-handed quarks only [CEHL14, BDSJ⁺14], to the $\phi_{(i),u,R}$ [DNRT13] or $\phi_{(i),d,R}$ [PVZ14, A⁺14a], or some combination [BB13, AWZ14].

As for the s-channel models, we assume Minimal Flavor Violation (MFV), setting the mediator masses for each flavor equal; the same logic also applies to the couplings g. The free parameters are then

$$\{m_{\text{DM}}, M_\phi, g\}. \qquad (2.15)$$

To do **What about Tait model? (??)**

The minimal width of each mediator is expressed, using the example of decay to an up quark, as

$$\Gamma(\phi_{(i)} \to \bar{u}_{(i)} \chi) = \frac{g^2_{(i)}}{16\pi M^3_{\phi_{(i)}}} (M^2_{\phi_{(i)}} - m^2_{u_{(i)}} - m^2_{\text{DM}})$$
$$\times \sqrt{(M^2_{\phi_{(i)}} - (m_{u_{(i)}} + m_{\text{DM}})^2)(M^2_{\phi_{(i)}} - (m_{u_{(i)}} - m_{\text{DM}})^2)}, \qquad (2.16)$$

which reduces to

$$\frac{g^2_{(i)} M_{\phi_{(i)}}}{16\pi} \left(1 - \frac{m^2_{\text{DM}}}{M^2_{\phi_{(i)}}}\right)^2 \qquad (2.17)$$

in the limit $M_{\phi_{(i)}}, m_{\text{DM}} \gg m_{u_{(i)}}$.

The leading-order processes involved in $\not{E}_T$+jet production are shown in Fig. 2.27. Note that the generation index i for $\phi_{(i)}$ is linked to the incoming fermion(s), and it runs on all three quark generations due to the MFV assumption. However, if the coupling g includes a Yukawa coupling proportional to the quark mass, and g is sufficiently large, LHC searches will still be sensitive to this model, as explained in Section 2.3.3.

This model can also give a signal in the $\not{E}_T$ + di-jet channel when, for example, the χ is exchanged in the t-channel and the resulting ϕ pair each decay to a jet + χ. Fig. 2.28 shows the leading

order diagrams. Except for the gg induced process, di-jet produc-
tion through the third-generation mediator $\phi_{(3),u}$ is not possible,
and production through $\phi_{(3),d}$ is again suppressed. The diagram in-
volving the t-channel exchange of χ is strongly dependent upon the
Dirac fermion assumption. For a Majorana fermion, $q\bar{q}$, $\bar{q}\bar{q}$, and qq
production would be possible with the latter having a pronounced
enhancement at the LHC.

This model is similar to the simplified model considered in SUSY
searches, implemented as the MSSM with only light squarks and a
neutralino, except for two distinct points: the χ is a Dirac fermion
and the coupling g is not limited to be weak scale ($g \ll 1$). In the
MSSM, most of these processes are sub-dominant, even if reso-
nantly enhanced, because the production is proportional to weak
couplings. In the more general theories considered here, g is free
to take on large values of order 1 or more, and thus diagrams ne-
glected in MSSM simulation can occur at a much higher rate here.
While constraints from SUSY jets$+\not{E}_T$ analyses on MSSM mod-
els can be recast to apply to the specific model in this report, DM
searches should also directly test their sensitivity to the MSSM
benchmark models.

2.3.1   Parameter scan

Ref. [PVZ14] studies the parameter space and obtains bounds on
this model from LHC Run 1 mono-jet and dijets$+\not{E}_T$ data. The
Forum did not exhaustively compare the kinematic distributions
of this model as was done in the s-channel case. While this means
the recommendations below should be taken with more caution, the
model is plausible and distinctive, and it should be included in the
design of LHC searches.

As in the s-channel models, scans should be performed over
m_{DM} and M_ϕ. The viable ranges of both parameters nearly coin-
cide with the scan proposed for the s-channel; for simplicity we
recommend adopting the s-channel mono-jet grid. In contrast to the
s-channel case, the bounds one obtains from $\not{E}_T+X$ searches depend
strongly on the width of the mediator, as is visible in Figs. 5 and 6
of Ref. [PVZ14], except in the heavy mediator limit ($M_\phi \approx 2\,\mathrm{TeV}$).
A scan over the width was not available for this report. Thus we
recommend scanning a range of possible widths as discussed in a
more-limited way for the s-channel mono-jet, spanning from the
minimal width to a value approaching the particle limit (for exam-
ple, $\Gamma \approx M_\phi/3$ in Ref. [PVZ14]).

2.3.2   Additional considerations for $V + \not{E}_T$ signatures

The model parameters with emission of an EW boson generally
follow those in Section 2.3. even though fewer diagrams are in-
volved. A representative Feynman diagram can be constructed by
replacing a final-state gluon in Fig. 2.27 with a γ, W, Z boson. See
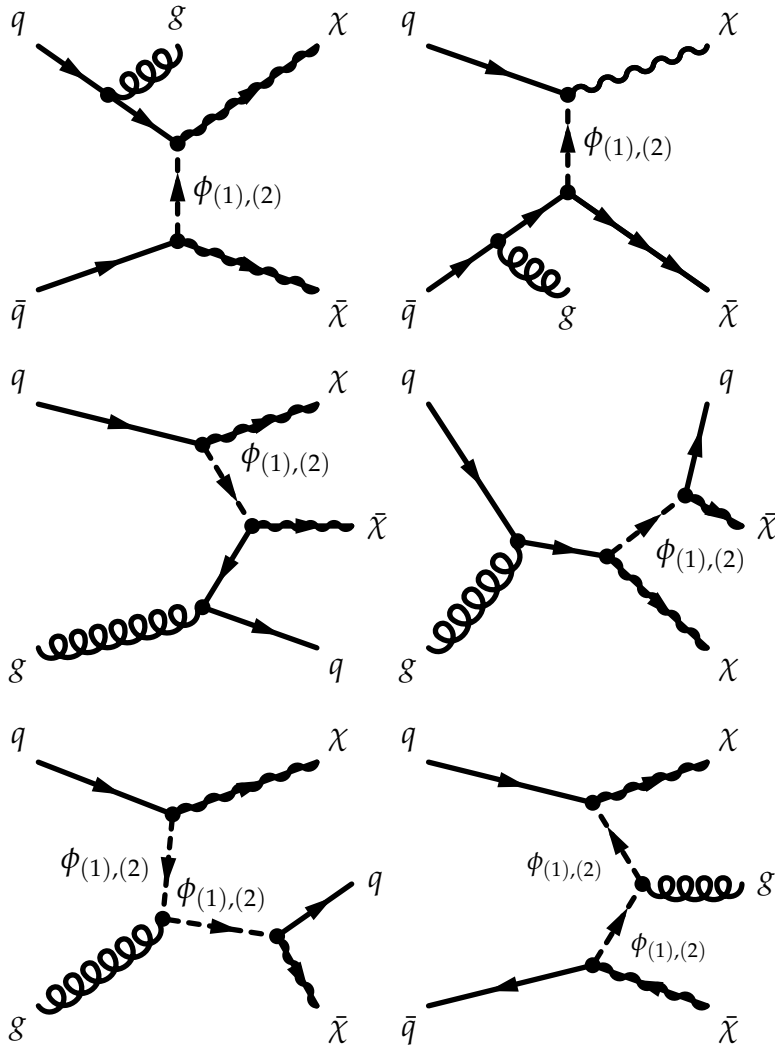Ref. [BDG$^+$12] for a theoretical overview of this model with specific

Figure 2.27: Leading order mono-jet t-channel processes, adapted from [PVZ14].
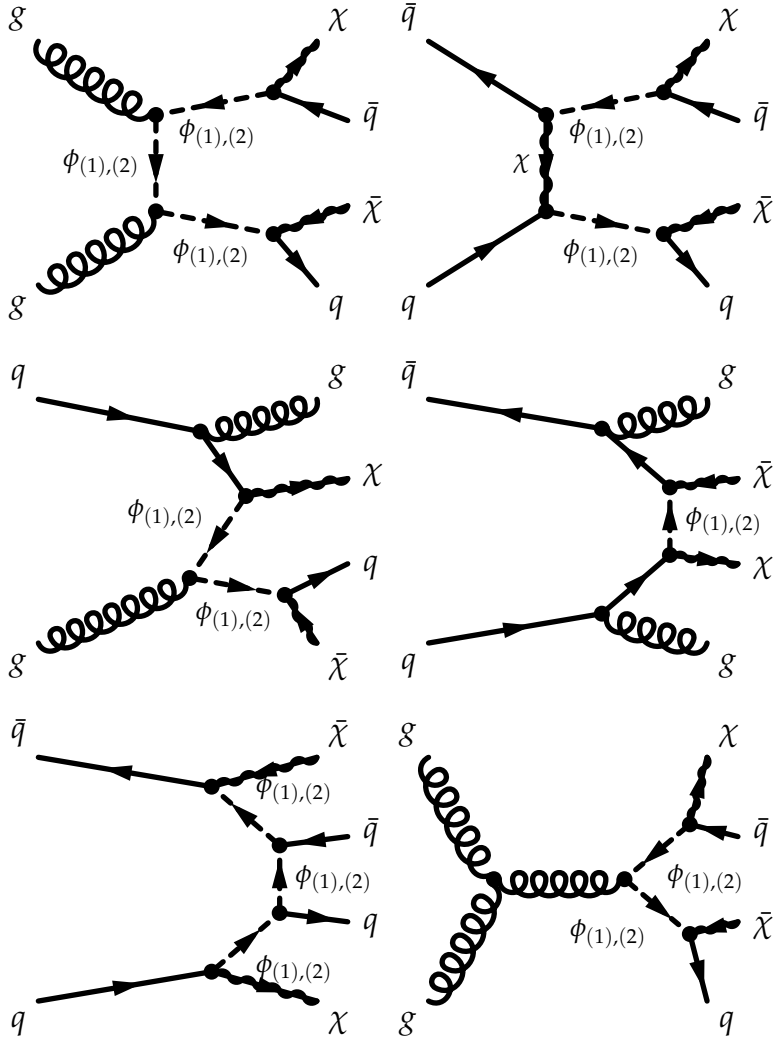
Figure 2.28: Leading order two-jet *t*-channel processes, adapted from [PVZ14].

examples for the Z+$\not{E}_T$ final state.

Figure 2.29 shows the $\not{E}_T$ distribution for the hadronic Z+$\not{E}_T$
final state, with varying dark matter and mediator mass, before any
selection. The acceptance for a series of basic analysis selections ($\not{E}_T$
>350 GeV, leading jet p_T > 40 GeV, minimum azimuthal angle
between jet and $\not{E}_T$ > 0.4) applied at the generator level is shown in
Figure 2.30.
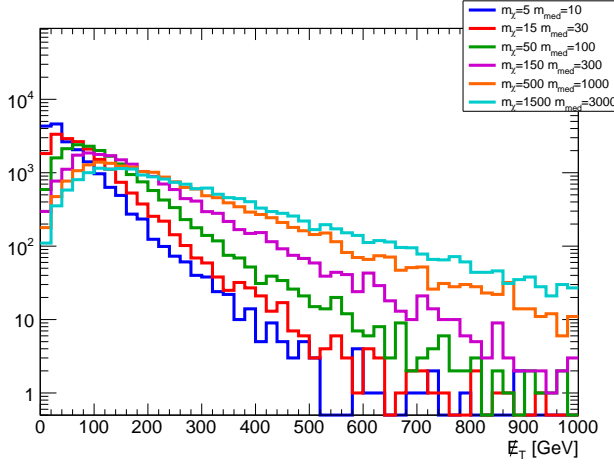
Figure 2.29: Missing transverse momentum distribution for the hadronic Z+$\not{E}_T$ final state, for the simplified model with a colored scalar mediator exchanged in the t-channel.
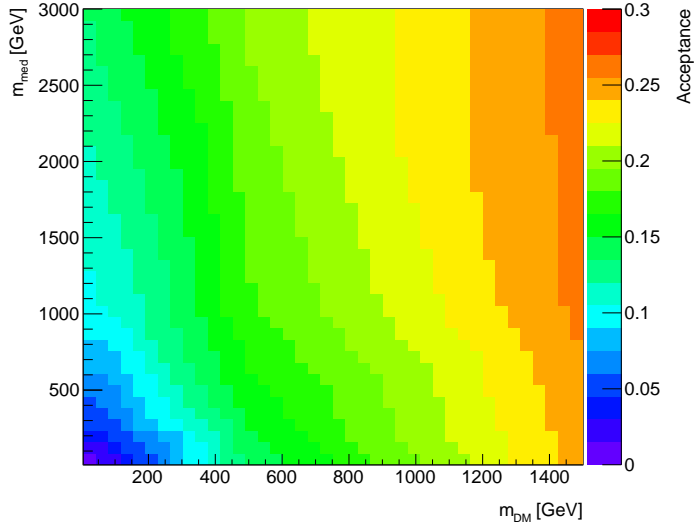
Figure 2.30: Acceptance for the hadronic Z+$\not{E}_T$ final state, for the simplified model with a colored scalar mediator exchanged in the t-channel.

The discussion of the parameter scan for the t-channel model
in the case of signatures including EW bosons parallels that of the
monojet case.

2.3.3   Additional considerations for signatures with b−quarks + $\not{E}_T$

Models of bottom-flavored Dark Matter that are closely related to
the t-channel mediated model from this Section have been pro-
posed in Refs. [LKW13, ABHL14]. Here, DM couples preferentially

to bottom quarks, with a decoupled third generation. We describe the *b*-FDM model of Ref. [ABHL14], created to explain the Galactic Center (GC) gamma-ray excess observed in data collected by the Fermi-LAT collaboration [DFH+14, CCW15]. This model favors couplings to third-generation quarks via Yukawa couplings, therefore respecting the MFV assumption.

This model produces an annihilation cross section consistent with the gamma-ray excess that has perturbative values for the couplings and is consistent with LHC constraints on the colored mediator. For parameters capable of explaining the anomalous gamma-ray signal in terms of Dark Matter coupling preferentially to *b*-quarks, the model predicts a direct detection cross section that is consistent with current constraints, but within the near future reach of Direct Detection experiments and of the upcoming LHC run.

The model contains a Dirac fermion transforming as a flavor triplet, exclusively coupling to right-handed down-type quarks. The third component of the triplet χ_b comprises the cosmological DM. Within the MFV framework, the other fermions in the flavor triplet can be made sufficiently heavy and weakly-coupled that they can be neglected in the analysis. A flavor singlet, color triplet scalar field Φ mediates the interactions between the DM and the Standard Model quarks. The model is similar to the MSSM with a light bottom squark and neutralino, and is thus a flavor-specific example of a *t*-channel model.

The Lagrangian considered is given by

$$-\mathcal{L} \supset g\Phi^*\bar{\chi}_b b_R + \text{h.c.} \qquad (2.18)$$

To do **Spell out implications on MFV assumption, and whether top-flavored could exist too. (??)**

Parameter scan   The nature of the model is not conducive to a simple scaling behavior that would allow us to reduce the number of points to be simulated. This is because of the interference of diagrams with QCD production of the mediator (which scale as g_s^2) with diagrams that are proportional to the coupling g in the $b+\not{E}_T$ and $b\bar{b}+\not{E}_T$ final states. Fixing the couplings also fixes the mediator width, when adopting the minimal width assumption.

A full study of the parameter scan for this model was not available for this report; thus we recommend scanning a range of possible widths as discussed in a more-limited way for the *s*-channel mono-jet, spanning from the minimal width to a value approaching the particle limit, e.g. $g = 0.5, 1, 2, 3$. A coupling benchmark such as $g = 1$ should be considered for each mass point since this would be a distinctive feature of this benchmark from SUSY models with sbottom squarks (see Section 2.3 for further discussion): Cross-sections for unit couplings can be found in Appendix **??**. The coupling could also be chosen to fulfill constraints from the relic density (see Appendix **??**, with corresponding cross sections in Tables **??** onwards).

A scan of Dark Matter and mediator masses should be done in the on-shell region $M_\Phi > m_{\text{DM}} + m_b$, since the cross-sections in

981 the off-shell region are too small to be probed with early LHC data,
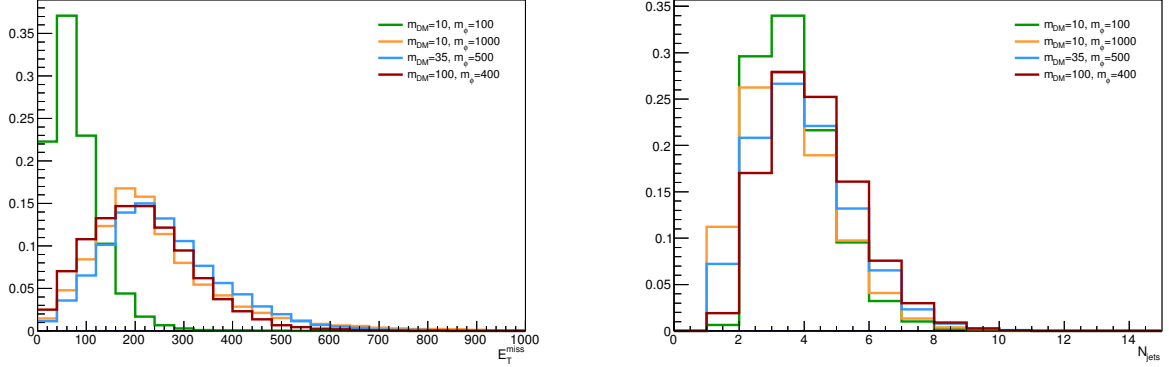982 spanning from 10 to 500 GeV in m_{DM} and from 10 to 1300 GeV in
983 M_Φ.

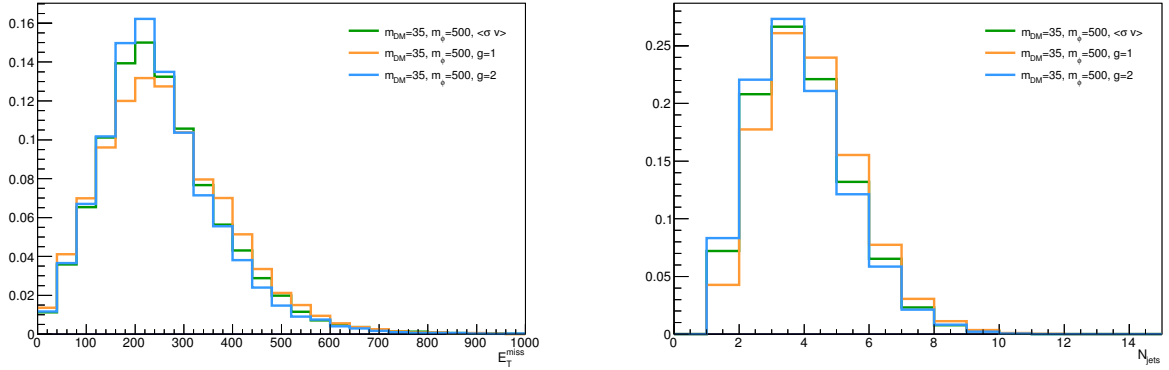Figure 2.31: $\not{E}_T$ (left) and jet multiplicity (right) for various DM and mediator masses and couplings per

Figure 2.32: $\not{E}_T$ (left) and jet multiplicity (right) for $m_{DM} = 35$ GeV and $M_\Phi = 500$ GeV for couplings corresponding to relic density weights and also $g = 1, 2$

984 ## 2.4 *Spin-2 mediator*

985 In models with extra dimensions, the Kaluza-Klein excitations of
986 the graviton could also serve as a mediator between the Standard
987 Model and dark sector physics. This kind of model was not studied
988 in the forum and is not included in the recommendations, but it
989 and models such as Ref. [LPS14] may warrant further study on a
990 longer timescale.

991 ## 2.5 *Presentation of results for reinterpretation of s-channel me-*
992   *diator models*

993 The aim of the parameter grid optimization done for the *s*-channel
994 models in the previous sections is to reduce the parameter space
995 that must be simulated. We then need a procedure for populating
996 the full parameter space by using the simulated grid points. We
997 recommend doing this as follows:

- When the dependences on parameters are known, the cross sections and efficiencies are general points can be calculated from the grid data.

- In other cases, this information can be obtained by interpolation between the grid points. We have chosen the grid points so that the dependence is sufficiently smooth that this will be possible.

The results of the scan over the couplings presented in the previous sections indicate that there are no changes in kinematic distributions for different choices of the coupling strengths. This means that the acceptance remains the same in the whole g_q–g_{DM} plane and it is sufficient to perform the detector simulation only for one single choice of g_q, g_{DM}. The resulting truth-level selection acceptance and the detector reconstruction efficiency can then be applied to all remaining grid points in the g_q–g_{DM} plane where only the generator-level cross section needs to be known. This significantly reduces the computing time as the detector response is by far the most CPU-intensive part of the Monte Carlo sample production. However, the number of generated samples can be reduced even further if a parameterization of the cross section dependence from one grid point to another exists. In this section, we describe the details of a cross section scaling procedure that can be used to reinterpret results for a fixed coupling for s-channel mediator models.

The propagator for the s-channel exchange is written in a Breit-Wigner form as $\dfrac{1}{q^2 - M_{med}^2 + iM_{med}\Gamma}$, where q is the momentum transfer calculated from the two partons entering the hard process after the initial state radiation, which is equivalent to the momentum of the Dark Matter pair. The size of the momentum transfer with respect to the mediator mass allows us to classify the production in the following way:

- off-shell production when $q^2 \gg M_{med}$ leading to suppressed cross sections,

- on-shell production when $q^2 \sim M_{med}$ leading to enhanced cross sections,

- effective field theory (EFT) limit when $q^2 \ll M_{med}$.

All three categories can be distinguished in Fig. 4.1 showing the upper limit on the interaction scale $M^* \equiv M_{med}/\sqrt{g_q g_{DM}}$ for vector mediator. In the case of the off-shell production and the EFT limit, the first and second term in the propagator dominate, respectively, which reduces the dependence on the mediator width. Therefore, in these cases one can approximate the cross section as

$$\sigma \propto g_q^2 g_{DM}^2. \qquad (2.19)$$

The on-shell production regime is the most interesting one as it gives the best chances for a discovery at the LHC given the cross section enhancement. The propagator term with the width cannot

be neglected in this case and, in the narrow width approximation which requires $\Gamma \ll M_{\text{med}}$ (this is not necessarily the case in the benchmarks considered in the scans), one can integrate

$$\int \frac{ds}{(s - M_{\text{med}}^2)^2 + M_{\text{med}}^2 \Gamma^2} = \frac{\pi}{M_{\text{med}} \Gamma} \qquad (2.20)$$

which further implies the cross section scaling

$$\sigma \propto \frac{g_q^2 g_{\text{DM}}^2}{\Gamma}. \qquad (2.21)$$

The narrow with approximation is important here as it ensures an integration over parton distribution functions (PDFs) can be neglected. In other words, it is assumed the integrand in Eq. 2.20 is non-zero only for a small region of s, such that the PDFs can be taken to be constant in this range. By simplifying the dependence of the minimal width on the couplings as $\Gamma \sim g_q^2 + g_{\text{DM}}^2$, one can approximate this scaling rule in the extreme cases as follows

$$\sigma \quad \propto \quad \frac{g_q^2 g_{\text{DM}}^2}{g_q^2 + g_{\text{DM}}^2} \xrightarrow{g_q \ll g_{\text{DM}}} g_q^2 \qquad (2.22)$$

$$\sigma \quad \propto \quad \frac{g_q^2 g_{\text{DM}}^2}{g_q^2 + g_{\text{DM}}^2} \xrightarrow{g_q \gg g_{\text{DM}}} g_{\text{DM}}^2 . \qquad (2.23)$$

However, it is important to keep in mind that this formula omits color and multiplicity factors as well as possible Yukawa suppression, and there is no simple scaling rule for how the cross section changes with the Dark Matter mass and the mediator mass, or for mediators with a large width, because PDFs matter in such cases as well. Therefore, the scaling procedure outlined above is expected to work only for fixed masses and fixed mediator width, assuming the narrow width approximation applies.

Figure 2.33 shows the minimal width over the mediator mass in the g_q–g_{DM} plane for vector and scalar mediators for $M_{\text{med}} = 100$ GeV and 1000 GeV, taking $m_{\text{DM}} = 10$ GeV. The individual colors indicate the lines of constant width, along which the cross section scaling may work for narrow mediators. The limiting case $\Gamma_{\text{min}} = M_{\text{med}}$ defines the upper values of the couplings below which the narrow width approximation can be considered and provides more stringent constraint than the perturbative limit $g_q = g_{\text{DM}} = 4\pi$. For vector and axial-vector mediators, the minimal width is predominantly defined by g_q due to the number of quark flavors and the color factor. On the contrary, both the Standard Model and Dark Matter partial width have comparable contributions in case of scalar and pseudo-scalar mediators if the top quark channel is open ($M_{\text{med}} > 2m_t$). However, mostly g_{DM} defines the minimal width for $M_{\text{med}} < 2m_t$ due to the Yukawa-suppressed light quark couplings.

The performance of the cross section scaling is demonstrated in Fig. 2.34 where two mass points $M_{\text{med}} = 100$ GeV and 1 TeV with
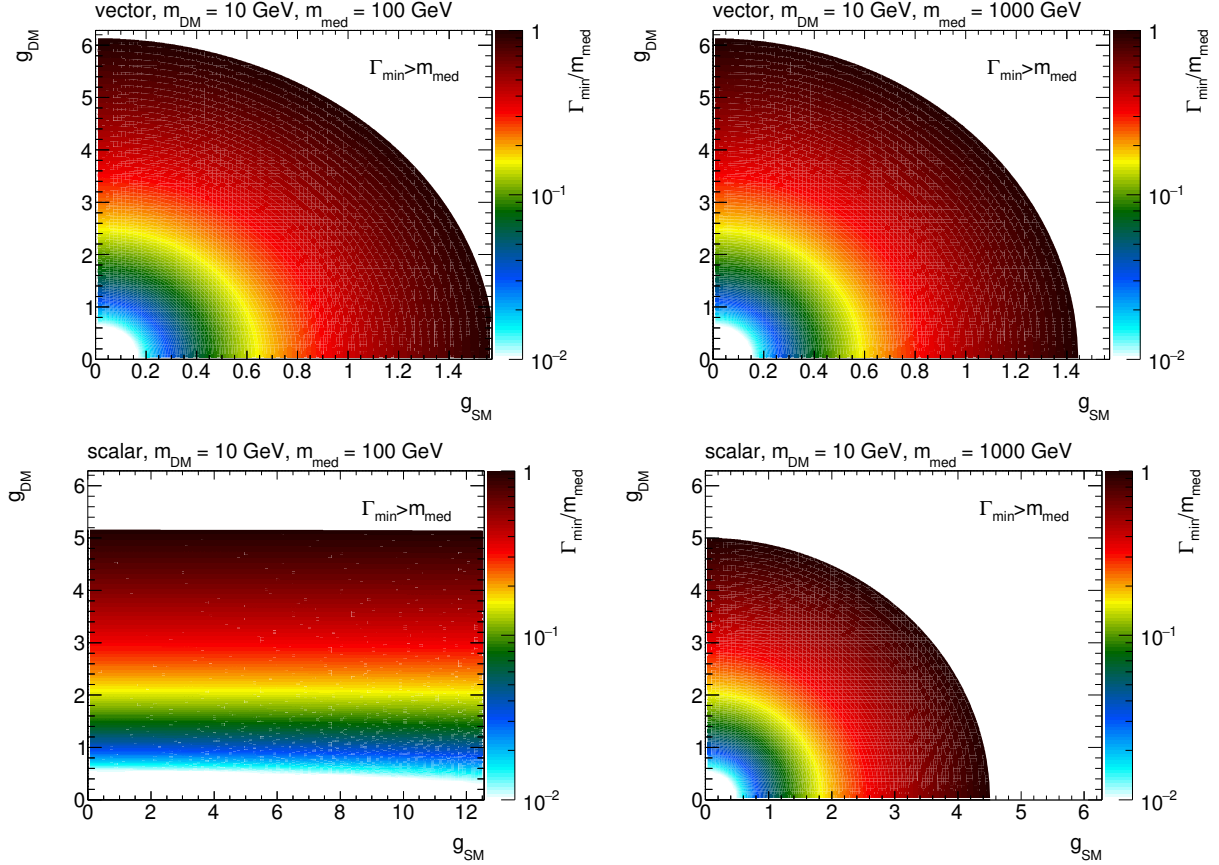
Figure 2.33: Minimal width over the mediator mass for vector (top) and scalar (bottom) mediators as a function of the individual couplings g_q and g_{DM}, assuming $M_{med} = 100$ GeV (left) and $M_{med} = 1$ TeV (right). $m_{DM} = 10$ GeV is considered in all cases. Only the cases with $\Gamma_{min} < M_{med}$ are shown.

$m_{DM} = 10$ GeV are chosen and rescaled from the starting point $g_q = g_{DM} = 1$ according to Eq. 2.21 to populate the whole g_q–g_{DM} plane. This means the width is not kept constant in this test and this is done in purpose in order to point out deviations from the scaling when the width is altered. For each mass point, the rescaled cross section is compared to the generator cross section and the ratio of the two is plotted. For the given choice of the mass points, the scaling seems to work approximately within the precision of $\sim 20\%$ in the region where $\Gamma_{min} < M_{med}$. Constant colors indicate the lines along which the cross section scaling works precisely and there is a remarkable resemblance of the patterns shown in the plots of the mediator width. To prove the scaling along the lines of constant width works, one such line is chosen in Fig. 2.35 for a scalar mediator, defined by $M_{med} = 300$ GeV, $m_{DM} = 100$ GeV, $g_q = g_{DM} = 1$, and the rescaled and generated cross sections are found to agree within 3%.

2.5.1 Proposed parameter grid for cross-section scaling

We propose to deliver collider results in the g_q–g_{DM} plane using the following prescription, to ease reinterpretation through cross-section scaling:

- Since the shapes of kinematic quantities do not change for different couplings, use the acceptance and efficiency for the available
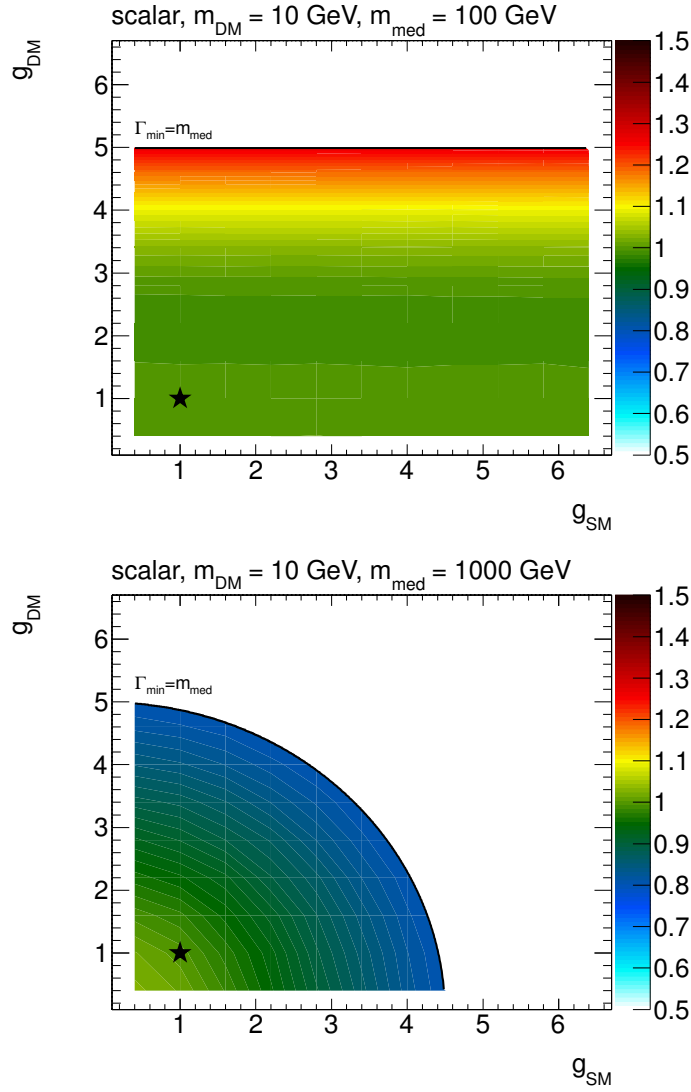
Figure 2.34: Ratio of the rescaled and generated cross sections in the g_q–g_{DM} plane. The point at $g_q = g_{DM} = 1$, taken as a reference for the rescaling, is denoted by a star symbol. Scalar model with $M_{med} = 100$ GeV (left) and 1 TeV (right) is plotted for $m_{DM} = 10$ GeV. The limiting case $\Gamma_{min} = M_{med}$ is indicated by a black line and no results are shown beyond.
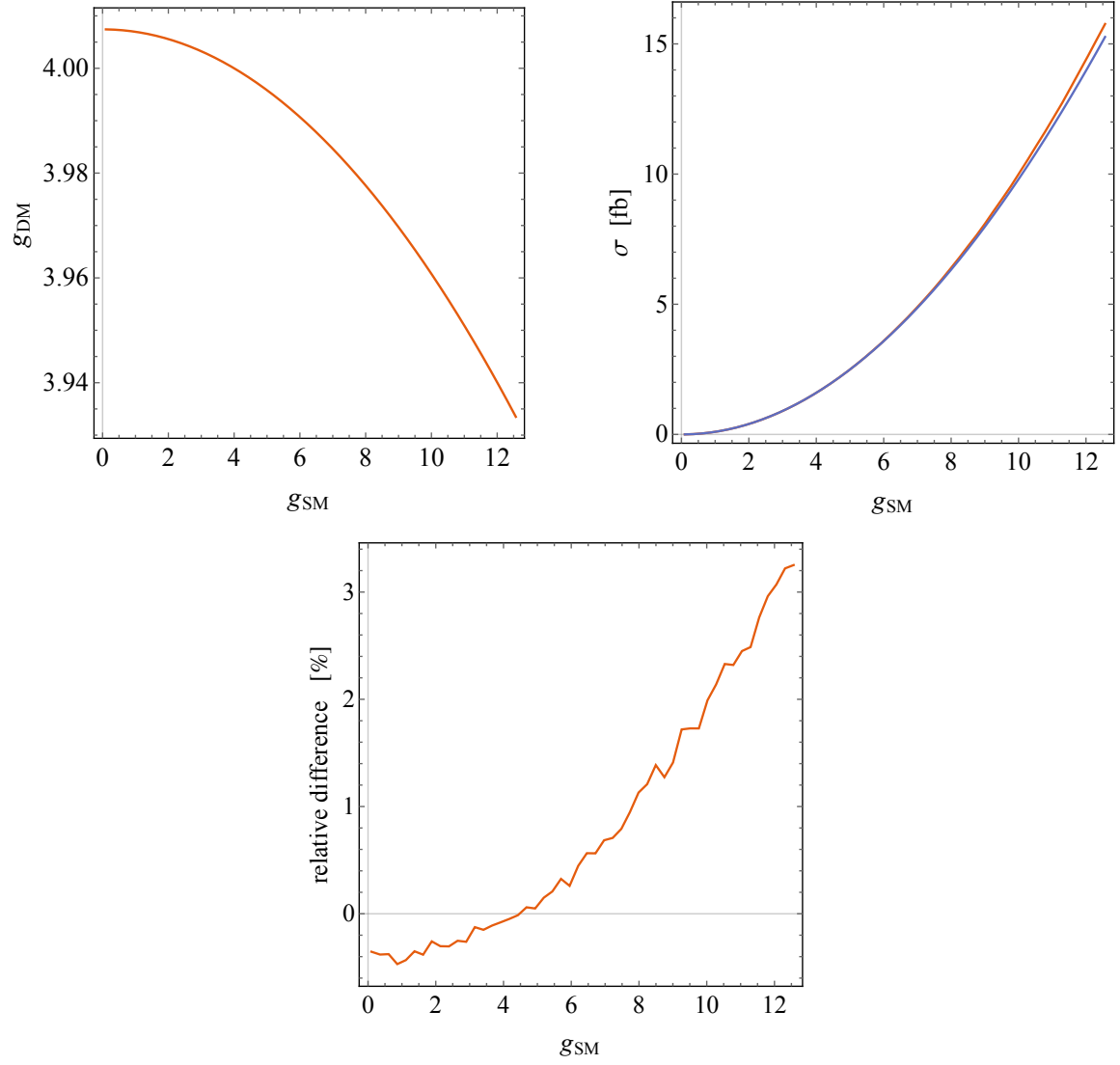
Figure 2.35: Scaling along the lines of constant width. The line of constant width for $M_{med} = 300$ GeV and $m_{DM} = 100$ GeV, intercepting $g_q = g_{DM} = 4$ is shown on left. The generated and rescaled cross sections are compared in the middle, the corresponding ratio is shown on right.

$m_{DM} = 50$ GeV, $M_{med} = 300$ GeV, $g_q = 0.25$, $g_{DM} = 1$ grid point from the M_{med}–m_{DM} plane for the scalar and pseudo-scalar mediator. In case of the vector and axial-vector mediator, use the grid point $m_{DM} = 150$ GeV, $M_{med} = 1$ TeV, $g_q = 0.25$, $g_{DM} = 1$.

• Generate additional samples in order to get generator cross sections only. For scalar and pseudo-scalar mediator, choose $m_{DM} = 50$ GeV, $M_{med} = 300$ GeV with the following values for $g_q = g_{DM}$: 0.1, 1, 2, 3. For vector and axial vector mediator, choose $m_{DM} = 150$ GeV, $M_{med} = 1$ TeV with the following values for $g_q = g_{DM}$: 0.1, 0.25, 0.5, 0.75, 1, 1.25, 1.5. The upper values are defined by the minimal width reaching the mediator mass.

To do **Waiting for scalar mediator calculation of perturbativity limit from J. Alcaraz.). (??)**

• Rescale the generator cross sections for on-shell resonance production along the lines of constant width in order to populate the whole g_q–g_{DM} plane in the region $\Gamma_{min} < M_{med}$. The scaling follows from Eq. 2.21 which for the constant width implies:

$$\sigma' = \sigma \times \frac{g_q'^2 g_{DM}'^2}{g_q^2 g_{DM}^2} . \qquad (2.24)$$

2.5.2   *Rescaling to different mediator width*

In general it is also important to consider a larger mediator width than Γ_{min} in order to accommodate additional interactions of the mediator with the visible and hidden sector particles [BFG15, HKSW15]. If the narrow width approximation applies, the cross section scaling method described above can be used to reinterpret the results presented for the minimal width, since multiplying the width by factor n is equivalent to changing the coupling strength by factor $\sqrt{n}$, i.e.

$$\sigma(g_q, g_{DM}, n\Gamma_{min}(g_q, g_{DM})) \propto \frac{g_q^2 g_{DM}^2}{\Gamma_{min}(\sqrt{n}g_q, \sqrt{n}g_{DM})} . \qquad (2.25)$$

The cross section for the sample with couplings g_q and g_{DM} and modified mediator width $\Gamma = n\Gamma_{min}$ can therefore be rescaled from a sample generated with the minimal width corresponding to the couplings scaled by $\sqrt{n}$ as described in the following formula.

$$\sigma(g_q, g_{DM}, n\Gamma_{min}(g_q, g_{DM})) = \frac{1}{n^2}\sigma(\sqrt{n}g_q, \sqrt{n}g_{DM}, \Gamma_{min}(\sqrt{n}g_q, \sqrt{n}g_{DM}))$$
$$(2.26)$$

The advantage of doing this is in the fact that no event selection and detector response needs to be simulated since the changes in couplings do not have an effect on the shapes of kinematic distributions.

It should be noted again that this procedure is only useful when the narrow width approximation applies. Care must be taken to ensure that is the case. For example, in the vector and axial-vector cases, one quickly breaks this approximation even for small n.

2.5.3   *Additional considerations for $t\bar{t}$ and $b\bar{b}+\not{E}_T$ signatures*

The cross-section scaling considerations shown in Sec. 2.5 still apply
for the reactions in the scalar and psuedoscalar models with explicit
b and t quarks. Here we detail the specific studies done for the $t\bar{t}$
model.

Given that the kinematics are similar for all couplings $g \simeq 1$,
we recommend to generate only samples with $g_{DM} = g_q = 1$. It
follows from this that these benchmark points should be a good
approximation for non-unity couplings and for $g_{DM} \neq g_q$, provided
that the sample is rescaled to the appropriate cross section times
branching ratio.

While the simple scaling function

$$\sigma' \times BR' = [\sigma \times BR] \times \left(\frac{g'_q}{g_q}\right)^2 \times \left(\frac{g'_{DM}}{g_{DM}}\right)^2 \times \frac{\Gamma}{\Gamma'} \tag{2.27}$$

is sufficient for a limited range of coupling values (see Fig. 2.36
for example), this scaling is only approximate (up to 20%) and
relies on the narrow width approximation, ignoring PDFs effects.
We also choose to provide instead a table of cross section times
branching ratio values over a large range of couplings to support
interpretation of search results (see the Appendix **??**). The table lists
couplings from $g = 0.1$ to $g = 3.5$, where the upper limit is chosen
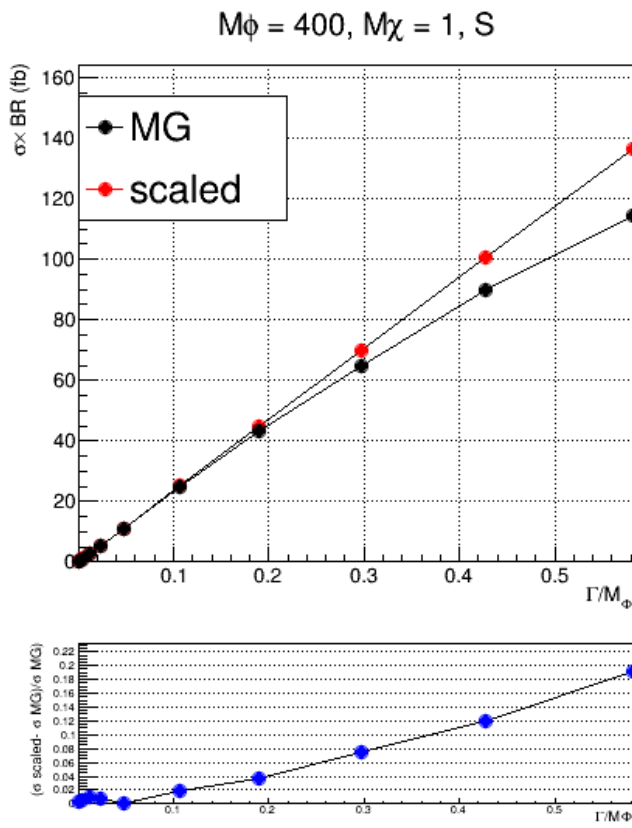to be close to but lower than the perturbative limit.

Figure 2.36: An example comparing a simple cross section scaling versus the computation from the MADGRAPH5_AMC@NLO generator, for a scalar $t\bar{t}+\not{E}_T$ model with $m_\phi = 400\,\text{GeV}$, $m_{\text{DM}} = 1\,\text{GeV}$ and all couplings set to unity. In this example, the scaling relationship holds for Γ_ϕ/m_ϕ below 0.2, beyond which finite width effects become important and the simple scaling breaks down.

3
Specific models for signatures with EW bosons

In this Section, we consider specific models with a photon, a W boson, a Z boson or a Higgs boson in the final state ($V+\not{E}_T$ signature), accompanied by Dark Matter particles that either couple directly to the boson or are mediated by a new particle. The common feature of those models is that they provide different kinematic distributions with respect to the models described in Section 2.

The models considered in this Section can be divided into two categories:

V-specific simplified models These models postulate direct couplings of new mediators to bosons, e.g. they couple the Higgs boson to a new vector or to a new scalar [CDM⁺14, BLW14].

Models involving a SM singlet operator including a boson pair that couples to dark matter through a contact interaction Shown on the right-hand side of Figure 3.1, these models allow for a contact interaction vertex that directly couples the boson to Dark Matter [CHLR13, CNS⁺13, CHH15, BLW14]. These models are included in this report devoted to simplified models since UV completions for most of these operators proceed through loops and are not available to date. These models provide a benchmark to motivate signal regions that are unique to searches with EW final states and would otherwise not be studied. However, we recommend to use these models as placeholders and emphasize model-independent results especially in signal regions tailored to these models. Wherever results are interpreted in terms of these operators, a truncation procedure to ensure the validity of the EFT should be employed, as detailed in the next Section (Sec. 4).

The following Sections describe the models within these categories, the parameters for each of the benchmark models chosen, the studies towards the choices of the parameters to be scanned.

3.1   *Specific simplified models including EW bosons, tailored to Higgs+MET searches*

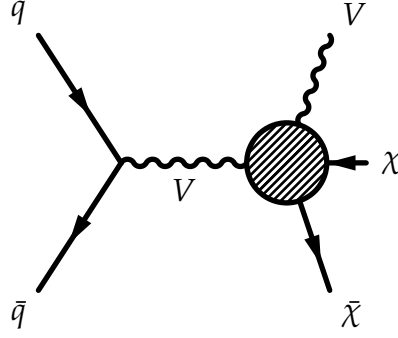Three benchmark simplified models [CDM⁺14, BLW14] are recommended for Higgs+$\not{E}_T$ searches:

Figure 3.1: Sketch of benchmark models including a contact interaction for V+MET searches, adapted from [NCC⁺14].

- A model where a vector mediator (Z'_B) is exchanged in the s-channel, radiates a Higgs boson, and decays into two DM particles (Fig. 3.2 (a)). As in Section 2.1, we conservatively omit couplings of the Z'_B to leptons.

- A model where a scalar mediator S is emitted from the Higgs boson and decays to a pair of DM particles (Fig. 3.3).

- A model where a vector Z' is produced resonantly and decays into a Higgs boson plus an intermediate heavy pseudoscalar particle A^0, in turn decaying into two DM particles (Fig. 3.2 (b)).
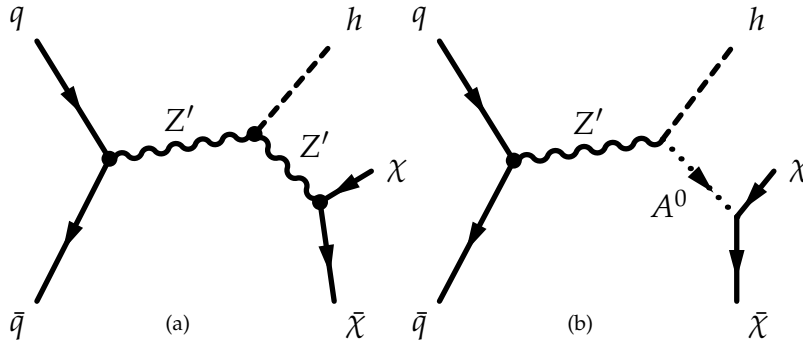
Figure 3.2: Examples of Feynman diagrams leading to Higgs+$\not{E}_T$ events: (a) a model with a vector mediator (Z') coupling with DM and with the Higgs boson h, and (b) a 2HDM model with a new invisibly decaying pseudoscalar A^0 from the decay of an on-shell resonance Z' giving rise to a Higgs+$\not{E}_T$ signature .

These models are kinematically distinct from one another, as shown in the comparison of the $\not{E}_T$ spectra in Fig. 3.4 for high and low masses of the pseudoscalar mediator. Figure 3.4 (a) shows the $\not{E}_T$ distribution for models with high mediator masses ($m_S = 1$ TeV, $m_{Z'} = 1$ TeV, $m_{A^0} = 1$ TeV) and DM mass of either 50 (Z'_B and A^0 models) or 65 GeV (scalar mediator model). Figure 3.4 (b) shows the $\not{E}_T$ distribution for models with low pseudoscalar mediator masses ($m_{Z'_B} = 100$ GeV, $m_{Z'} = 1$ TeV, $m_{A^0} = 100$ GeV) and DM mass of 1 TeV for all models.

3.1.1 $\not{E}_T$ +Higgs from a baryonic Z'

The model shown in Fig. 3.2 (a) postulates a new gauge boson Z' corresponding to a new $U(1)_B$ baryon number symmetry. The stable baryonic states included in this model are the DM candidate particles. The mass of the Z' boson is acquired through a baryonic Higgs h_B, which mixes with the SM Higgs boson.
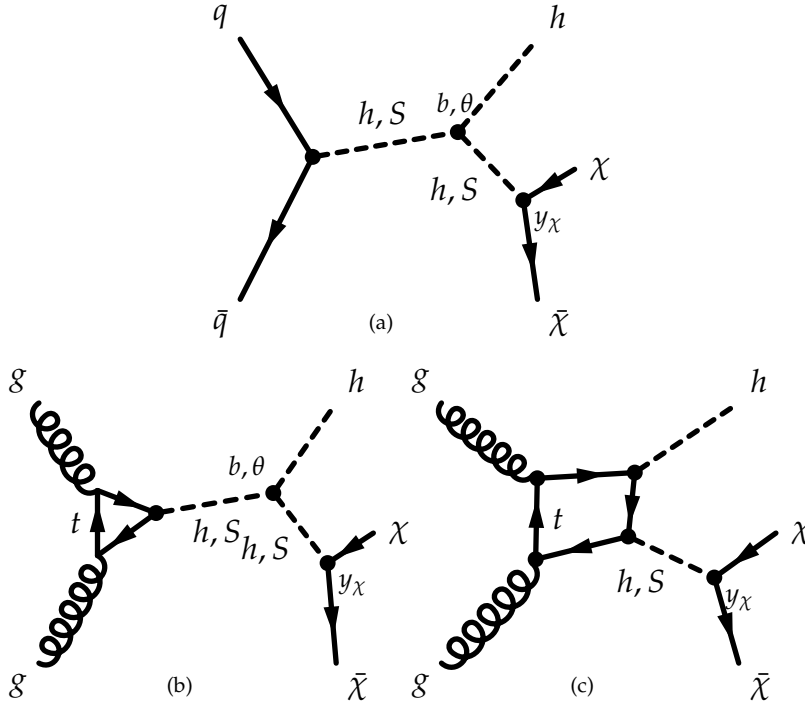
Figure 3.3: Examples of Feynman diagrams leading to Higgs+$\not{E}_T$ events for a model with a scalar mediator (S) coupling with DM and with the Higgs boson h.

The interactions between the Z', the quarks and the DM are described by the following Lagrangian:

$$L = g_q \bar{q} \gamma^\mu q Z'_\mu + g_{DM} \bar{\chi} \gamma^\mu \chi Z'_\mu. \tag{3.1}$$

The quark couplings g_q are fixed to be equal to one third of the gauge coupling g_B, while the DM coupling to the Z' are proportional to the baryon number and to the gauge coupling ($g_\chi = B g_B$). No leptonic couplings of the Z' are allowed, thus evading dilepton constraints. After incorporating the mixing of the baryonic and SM Higgs bosons, this model is is described by the following Lagrangian term at energies below $m_{Z'}$ [1]:

$$L_{eff} = -\frac{g_q g_{DM}}{m_{Z'}^2} \bar{q} \gamma^\mu q \bar{\chi} \gamma_\mu \chi \left(1 + \frac{g_{hZ'Z'}}{m_{Z'}^2} h\right), \tag{3.2}$$

The first term of this equation is the standard DMV model in the large $M_{Z'}$ limit. This term can lead to a monojet signature, which can be also used to constrain this model. The second term describes the interaction between the Z' and the SM Higgs boson, via the coupling $g_{hZ'Z'} = \frac{m_{Z'} 2 \sin\theta}{v_B}$, where $\sin\theta$ is the mixing angle between the SM Higgs and the baryonic Higgs h_B, and v_B is the Baryonic Higgs vacuum expectation value. In its most general form, this model can lead to mono-Z signals as well. However, in this case there is no $Z - Z'$ mixing from the $hZ'Z'$ term, since this term arises only after $U(1)_B$ is broken. A mixing angle can come from terms involving the field strengths of Z and Z': this is a free parameter, that is set to be small in the model considered for mono-Higgs signatures.

The predictions of the model depend upon the two additional parameters beyond an s-channel simplified model, namely the

[1] The operator in Eqn. 3.2 is an effective one, to highlight the two main terms. The full dimension-4 simplified model is used in the model for event generation.
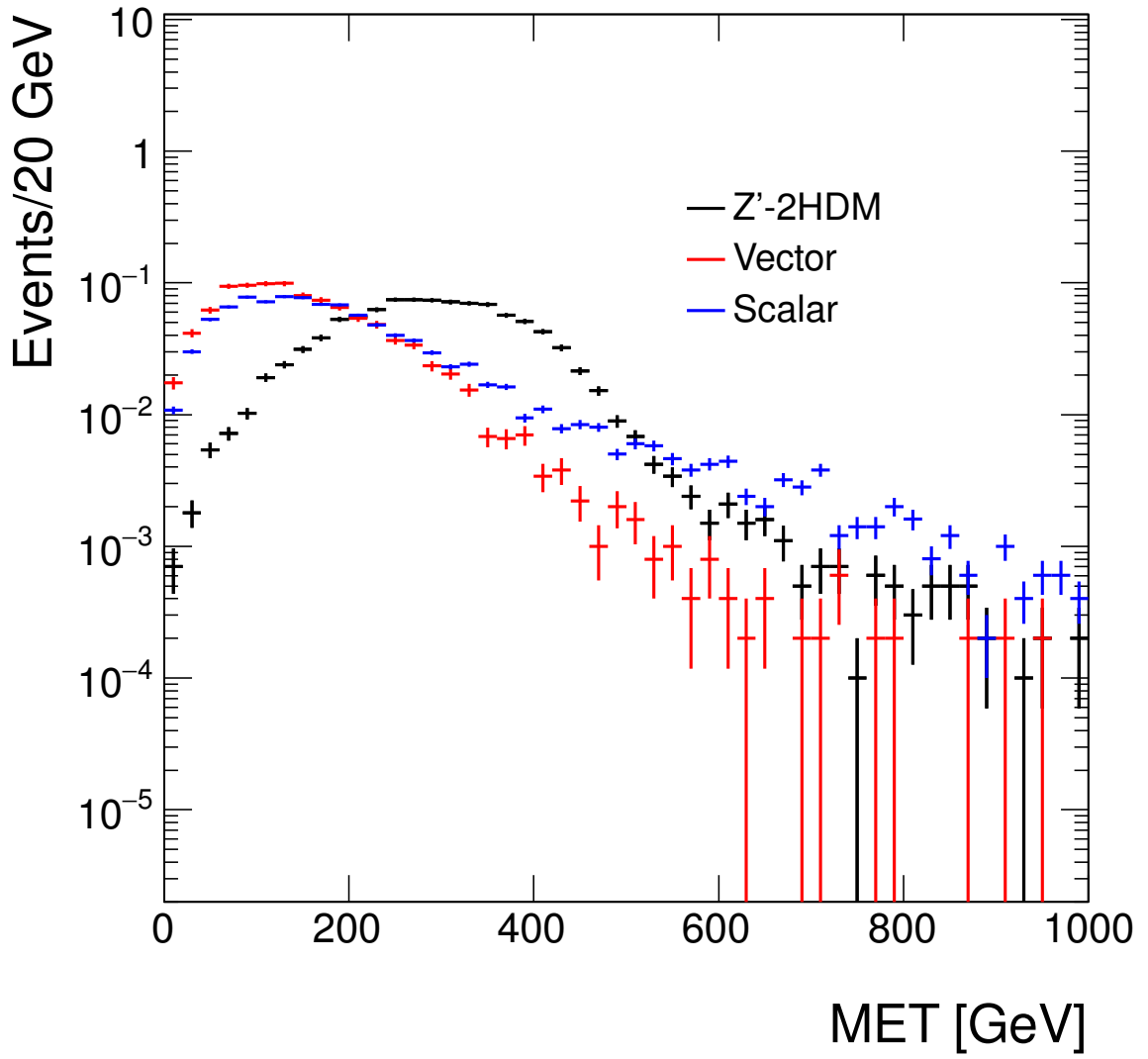
(a) High mediator mass
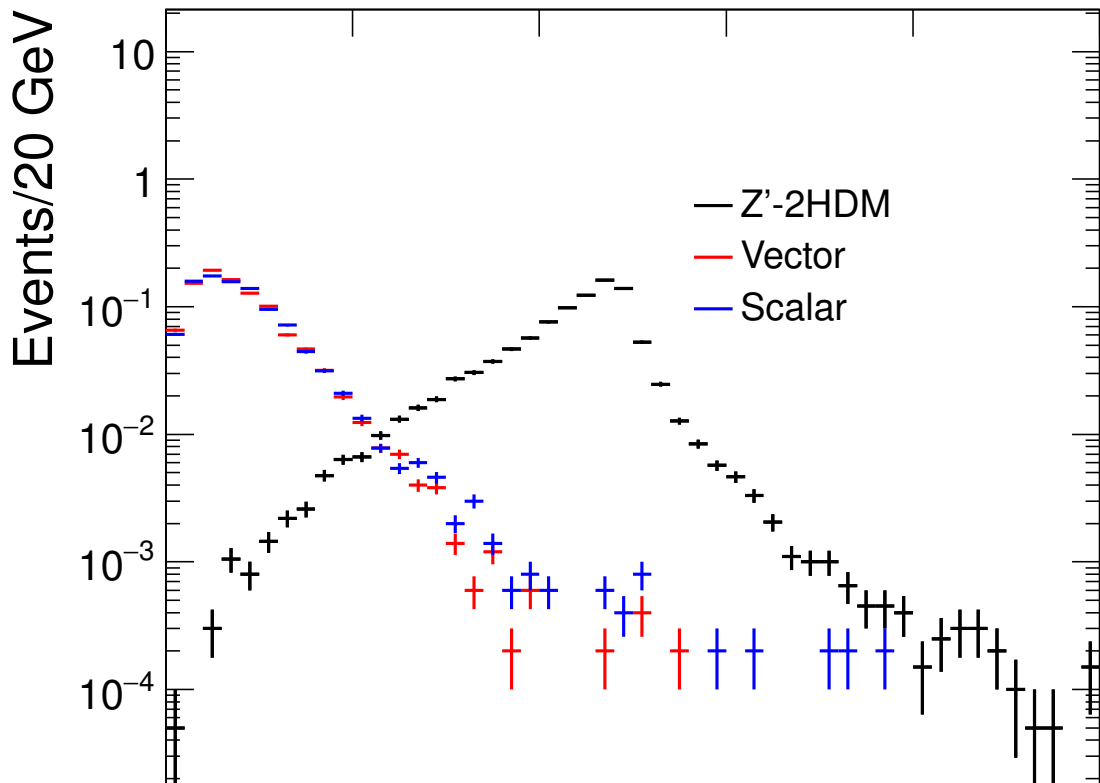
mixing angle between baryonic Higgs h_B and the SM-like Higgs boson $\sin\theta$ and the coupling of the mediator to SM-like Higgs boson, $g_{hZ'Z'}$. Thus, a full model is specified by:

$$\{M_{\text{med}}, m_{\text{DM}}, g_{\text{DM}}, g_{\text{q}}, \sin\theta, g_{hZ'Z'}\}. \tag{3.3}$$

3.1.1.1 *Parameter scan*

The width of the Z' mediator is calculated using all possible decays to SM particles (quarks) and to pairs of DM particles if kinematically allowed as in the DMV model.

The dependence of the missing transverse momentum ($\not{E}_T$) on the model parameters is studied by varying the parameters one at a time. The variation of parameters other than M_{med} and m_{DM} does not result in significant variations of the $\not{E}_T$ spectrum, as shown in Figures 3.5. Figure 3.6 shows that for an on-shell mediator, varying m_{DM} with the other parameters fixed does not affect the $\not{E}_T$ distribution, while the distribution broadens significantly in the case of an off-shell mediator. For this reason, the same grid in M_{med}, m_{DM} as for the vector mediator of the jet+$\not{E}_T$ search (Table 2.1) is chosen as a starting point. The coupling $g_{hZ'Z'}$, along with g_{q} and g_{DM}, are subject to perturbativity bounds:

$$g_{\text{q}}, g_{\text{DM}} < 4\pi$$

and

$$g_{hZ'Z'} < \sqrt{4\pi} m_{Z'} \sin\theta$$

The value $g_{hZ'Z'}/m_{Z'} = 1$ is chosen as a benchmark value for the generation of Monte Carlo samples since it maximizes the cross section (as shown in the following paragraph) without violating the bounds. The mediator-DM coupling g_{DM} is fixed to 1, and the mediator-quark g_q coupling is fixed to $1/3$. The kinematic distributions do not change as a function of these parameters, so results for other values of $g_{hZ'Z'}/m_{Z'}$, g_{DM} and g_{q} can be obtained through rescaling by the appropriate cross sections.

Figs 3.7 and 3.8 show the kinematic distributions for the two leading jets in the $H \to \bar{b}b$ decay channel, for two values of the mediator mass and varying the DM mass.

Analyses should perform further studies, beyond those studies performed for the forum, to estimate the reach of the analysis with respect to all points in the grid and therefore decide on a smaller set of grid points to be generated.

3.1.2 $\not{E}_T$ +*Higgs from a scalar mediator*

A real scalar singlet S coupling to DM can be introduced as a portal between SM and the dark sector through the Higgs field. The most general scalar potential is detailed in Ref. **??**, including terms that break $\mathbb{Z}_2$. This report does not cover the case in which $\mathbb{Z}_2$ holds
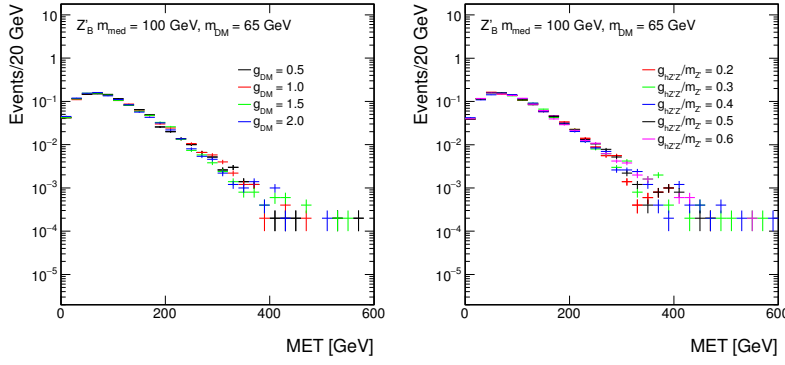
Figure 3.5: Missing transverse momentum distributions at generator level in the vector mediator scenario for different values of: the mediator-dark matter coupling g_{DM} (left), and the coupling between the mediator and the SM-like Higgs boson, scaled by the mediator mass, $g_{hZ'Z'}/m_{Z'}$ (right).

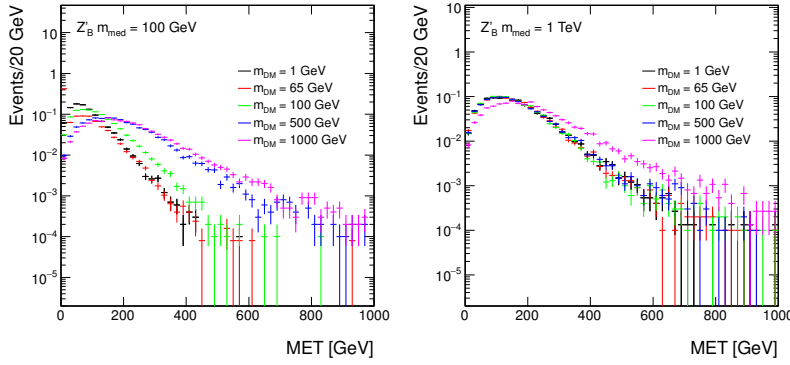Figure 3.6: Missing transverse momentum distributions at generator level in the vector mediator scenario: for different values of the dark matter mass m_{DM} and a mediator mass of M_{med} = 100 GeV (left) and M_{med} = 1 TeV (right).

and therefore the new scalar can be the DM candidate, but follows Ref. **??** introducing an additional coupling to DM that breaks $\mathbb{Z}_2$ and leads to a new invisible decay of S. For this reason, no symmetry is broken and no new interactions arise, so there is no dependence on the vacuum expectation value of S: a shift in the field leads to a redefinition of the model couplings. The new scalar S mixes with the SM Higgs boson, and couples to DM through a Yukawa term y_χ. The relevant terms in the scalar potential are:

$$V \supset a|H|^2 S + b|H|^2 S^2 + \lambda_h |H|^4$$
$$\longrightarrow \tfrac{1}{2}a(h+v)^2 S + \tfrac{1}{2}b(h+v)^2 S^2 + \frac{\lambda_h}{4}(h+v)^4, \qquad (3.4)$$

where a, b are new physics couplings and λ_h is the Higgs quartic coupling.

The additional Lagrangian terms for this model are:

$$L \supset -y_\chi \bar{\chi}\chi(\cos\theta\, S - \sin\theta\, h) - \frac{m_q}{v}\bar{q}q(\cos\theta\, h + \sin\theta\, S) \qquad (3.5)$$

where θ is the mixing angle between the Higgs boson and the new scalar.

Mono-Higgs signals in this second model arise through processes shown in Fig. 3.3 (a,b), or through the radiation of a Higgs boson from the t quark in the production loop, in Fig. 3.3 (c). The first two processes depend on the $h^2 S$ and hS^2 cubic terms
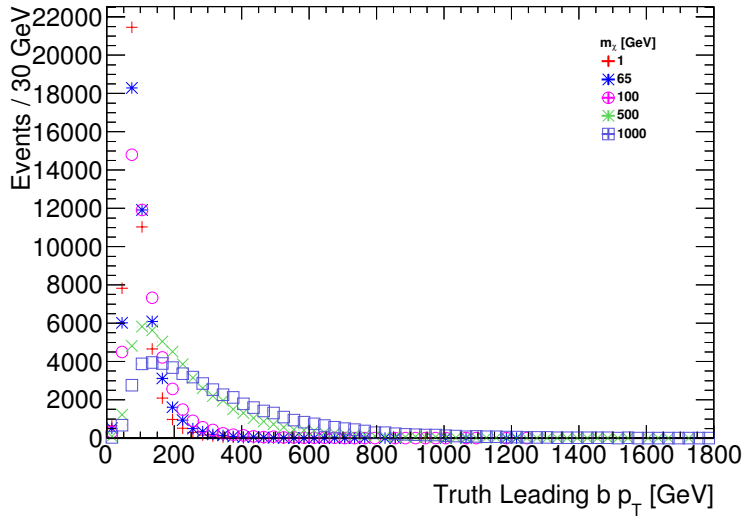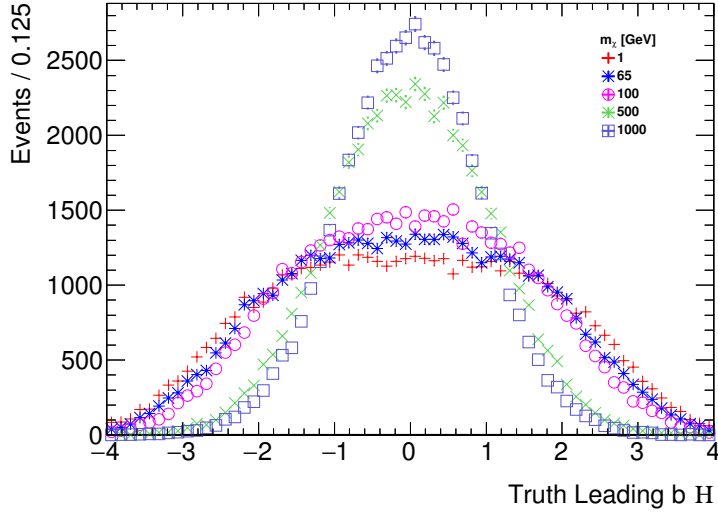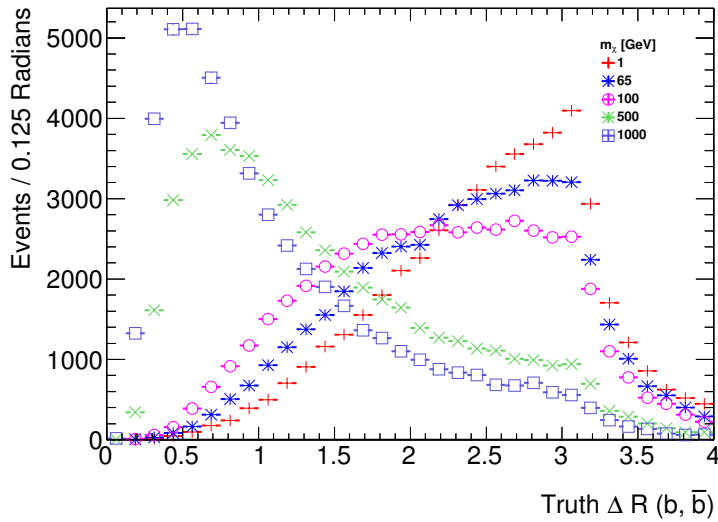
(a) Leading $b-$jet transverse momentum

(b) Leading $b-$jet pseudorapidity

(c) Angular distance between the two leading $b-$jets

Figure 3.7: Comparison of the kinematic distributions for the two leading $b-$jets (from the Higgs decay) in the vector Z' simplified model, when fixing the Z' mass to 100 GeV and varying the DM mass.

(a) Leading $b-$jet transverse momentum

Figure 3.8: Comparison of the kinematic distributions for the two leading jets from the Higgs decay in the vector Z' simplified model, when fixing the Z' mass to 1000 GeV and varying the DM mass.
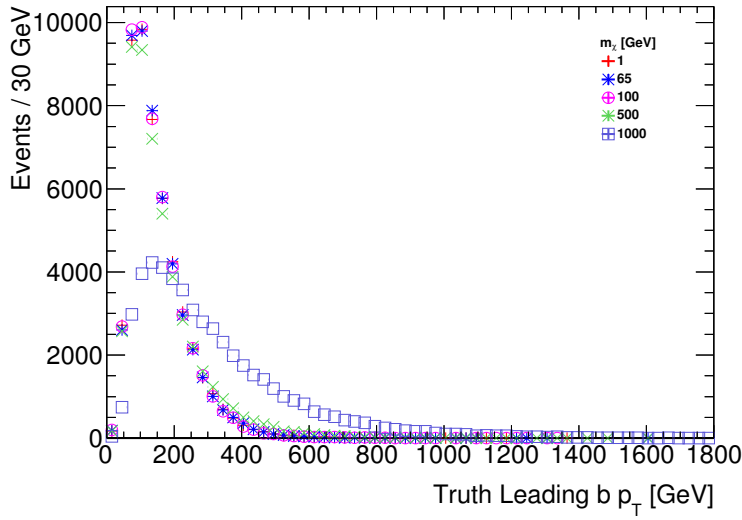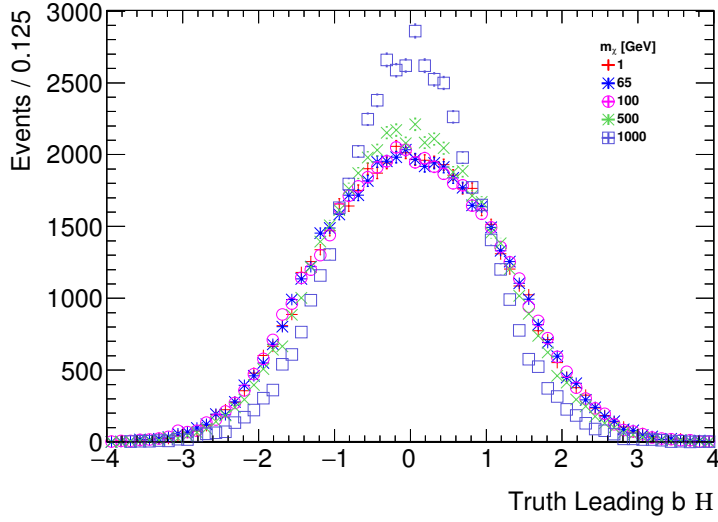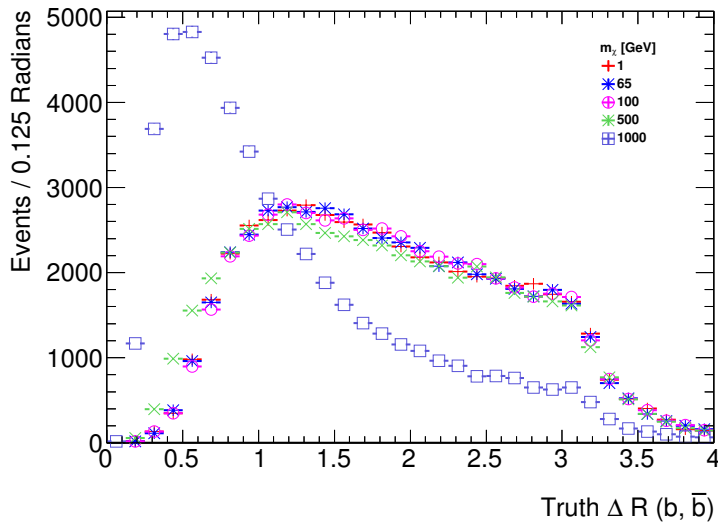

(b) Leading $b-$jet pseudorapidity

(c) Angular separation of the two leading b-jets

in Eq. (3.4). At leading order in $\sin\theta$, these terms are:

$$V_{\text{cubic}} \approx \frac{\sin\theta}{v}(2m_h^2 + m_S^2)h^2 S + b\,v\,h\,S^2 + \dots \qquad (3.6)$$

with a and λ_h expressed in terms of $\sin\theta$ and m_h^2, respectively. At leading order of $\sin\theta$, the $h^2 S$ term is fixed once the mass eigenvalues m_h, m_S and mixing angle are specified. The $h\,S^2$ term is not fixed and remains a free parameter of the model, depending on the new physics coupling b.

This model has mono-X signatures through h/S mixing. If $m_S \gg m_h$ or $m_h \gg m_S$, this model is a case of the scalar model discussed in Section 2.2, with M_{med} equal to the lighter of the two masses.

3.1.2.1 Parameter scan

The model is described by five parameters:

1. the Yukawa coupling of heavy scalar to dark matter, g_{DM} (also referred to as y_χ)

2. the mixing angle between heavy scalar and SM-like Higgs boson, $\sin\theta$;

3. the new physics coupling, b;

4. mass of heavy scalar, m_S, also termed M_{med};

5. mass of dark matter. m_{DM};

The mixing angle is constrained from current Higgs data to satisfy $\cos\theta = 1$ within 10% and therefore $\sin\theta \lesssim 0.4$. This provides a starting point for the parameter scan in this model: we recommend to set $\sin\theta = 0.3$. Figure 3.10 shows that there is no dependence of the kinematics from the value of this angle, and different values can be obtained via rescaling the results for this mixing angle according to the relevant cross-section. It can also be observed from Figures 3.11 and 3.9 that the kinematics of this model follows that of the equivalent jet+$\not{E}_T$ model: only small changes are observed in the on-shell region, while the relevant distributions diverge when the mediator is off-shell. For this reason, the same grid in M_{med}, m_{DM} as for the scalar mediator of the jet+$\not{E}_T$ search (Table 2.3) is chosen as a starting point. The Yukawa coupling to DM y_{DM} is set to 1, the new physics coupling between scalar and SM Higgs b = 3. Results for other values can be obtained via a rescaling of the results for these parameters.

To do **Estimate the sensitivity and possibly prune parameter scan. (??)**

Figs. 3.12 and 3.13 show the kinematic distributions for the two leading jets in the $H \to \bar{b}b$ decay channel, for two values of the mediator mass and varying the DM mass.

3.1.3 Higgs+$\not{E}_T$ signal from 2HDM model with a Z' and a new pseudoscalar

In this simplified model [BLW14], a new Z' resonance decays to a Higgs boson h plus a heavy pseudoscalar state A^0 in the 2HDM
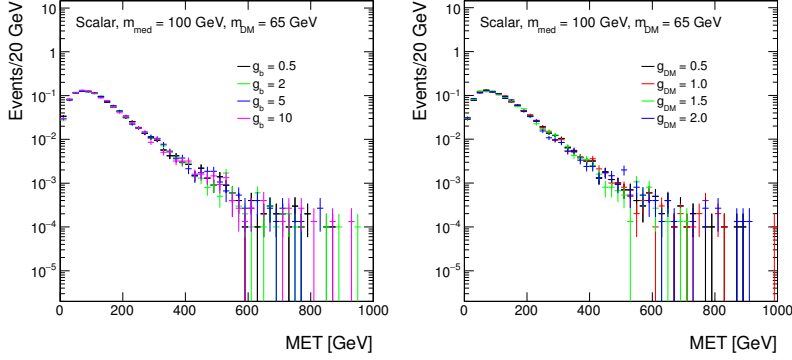
Figure 3.9: Missing transverse momentum distributions at generator level in the scalar mediator scenario, for different values of: the new physics coupling g_b (left), and the mediator-dark matter coupling g_{DM} (right).

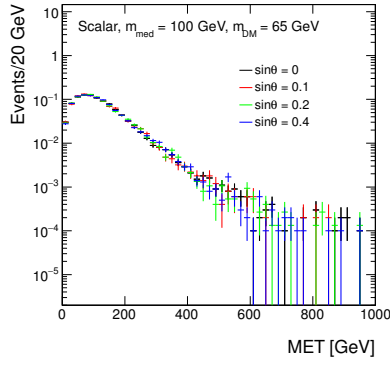Figure 3.10: Missing transverse momentum distributions at generator level in the scalar mediator scenario: for different values of the mixing angle $\sin\theta$.
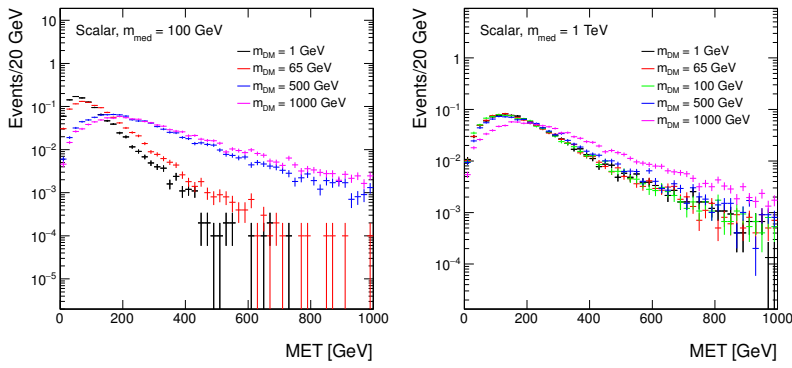
Figure 3.11: Missing transverse momentum distributions at generator level in the scalar mediator scenario: for different values of the dark matter mass m_{DM} and a mediator mass of $M_{med} = 100$ GeV (left) and $M_{med} = 1$ TeV (right).

(a) Leading $b-$jet transverse momentum

(b) Leading $b-$jet pseudorapidity

(c) Angular distance between the two leading $b-$jets

Figure 3.12: Comparison of the kinematic distributions for the two leading jets from the Higgs decay in the scalar simplified model, when fixing the new scalar mass to 100 GeV and varying the DM mass.

(a) Leading $b-$jet transverse momentum

(b) Leading $b-$jet pseudorapidity
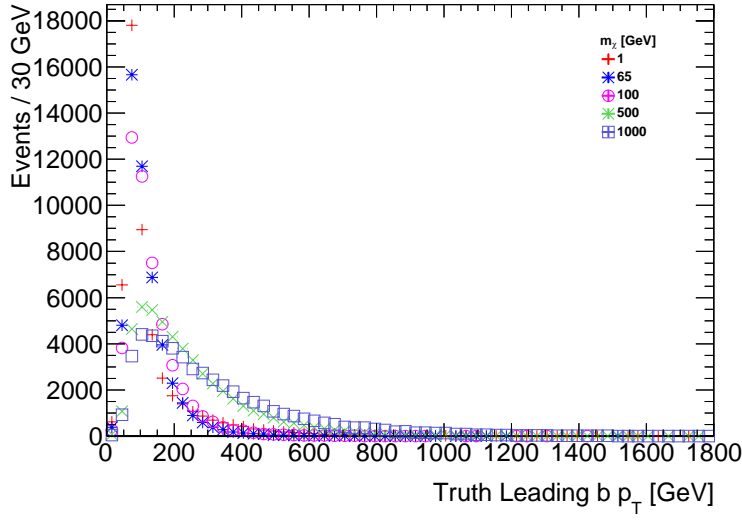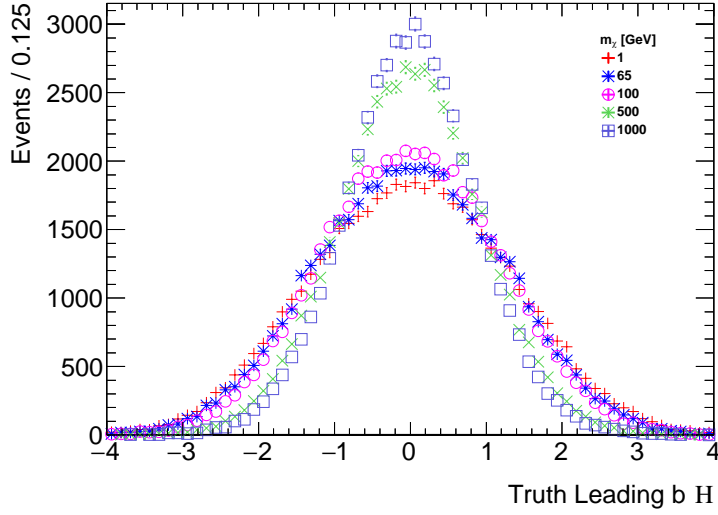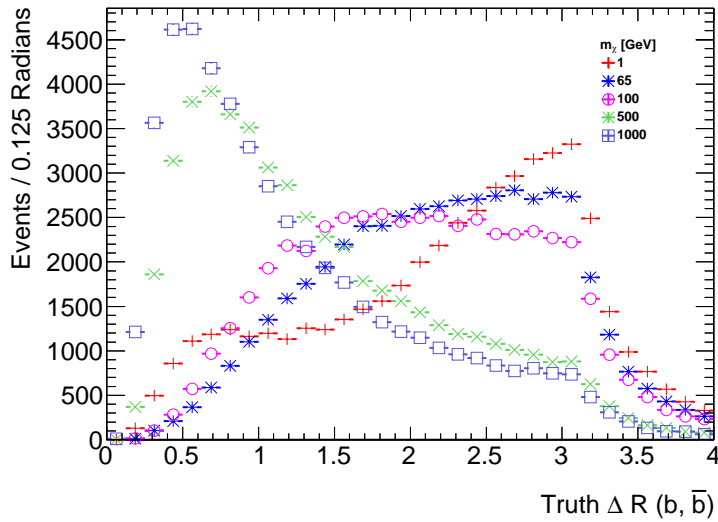

(c) Angular distance between the two leading $b-$jets

Figure 3.13: Comparison of the kinematic distributions for the two leading jets from the Higgs decay in the scalar simplified model, when fixing the new scalar mass to 1000 GeV and varying the DM mass.
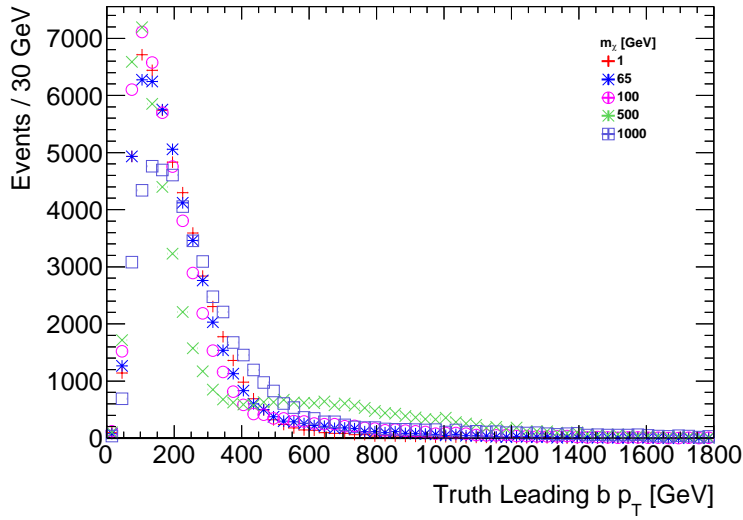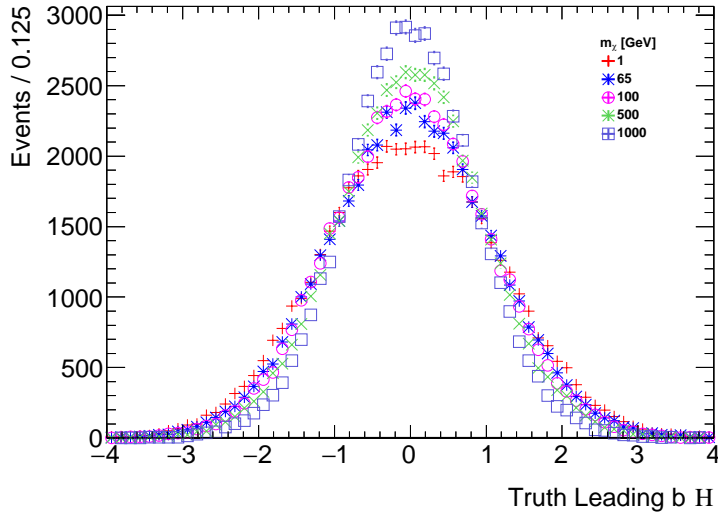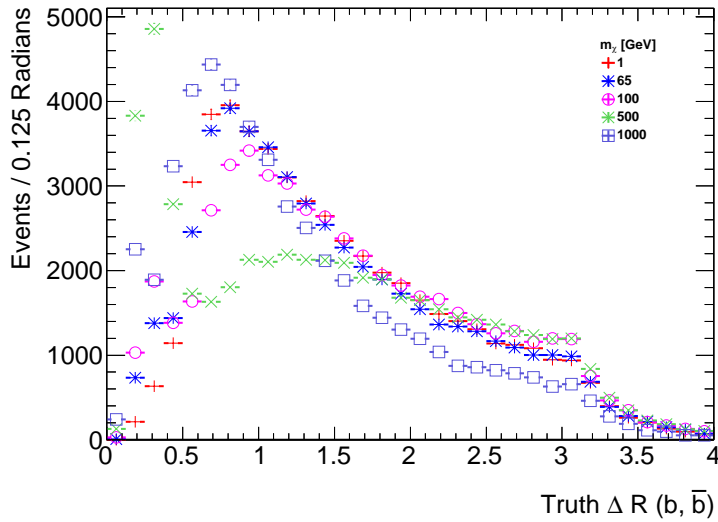
framework, which in turn decays to a DM pair. This model is represented in the diagram in Fig. 3.2 (b).

The motivation for coupling the dark matter to the pseudoscalar is that dark matter coupling to a Higgs or Z' boson is generically constrained by other signal channels and direct detection. A reason to consider this model is that it has different kinematics due to the on-shell Z' production, where for heavy Z' masses the $\not{E}_T$ and p_T spectra are much harder. This model can satisfy electroweak precision tests and constraints from dijet resonance searches, and still give a potentially observable Higgs+$\not{E}_T$ signal.

This model comprises two doublets, where Φ_u couples to up-type quarks and Φ_d couples to down-type quarks and leptons:

$$-\mathcal{L} \supset y_u Q \tilde{\Phi}_u \bar{u} + y_d Q \Phi_d \bar{d} + y_e L \Phi_d \bar{e} + \text{h.c.} \tag{3.7}$$

After electroweak symmetry breaking, the Higgs doublets attain vacuum expectation values v_u and v_d, and in unitary gauge the doublets are parametrized as

$$\Phi_d = \frac{1}{\sqrt{2}} \begin{pmatrix} -\sin\beta \; H^+ \\ v_d - \sin\alpha \; h + \cos\alpha \; H - i\sin\beta \; A^0 \end{pmatrix} \; ,$$

$$\Phi_u = \frac{1}{\sqrt{2}} \begin{pmatrix} \cos\beta \; H^+ \\ v_u + \cos\alpha \; h + \sin\alpha \; H + i\cos\beta \; A^0 \end{pmatrix} \tag{3.8}$$

where h, H are neutral CP-even scalars, $H^\pm$ is a charged scalar, and A^0 is a neutral CP-odd scalar. In this framework, $\tan\beta \equiv v_u/v_d$, and α is the mixing angle that diagonalizes the $h - H$ mass squared matrix. We take $\alpha = \beta - \pi/2$, in the limit where h has SM-like couplings to fermions and gauge bosons as per Ref. [CGT13], and $\tan\beta \geq 0.3$ as implied from the perturbativity of the top Yukawa coupling. The Higgs vacuum expectation values lead to $Z - Z'$ mass mixing, with a small mixing parameter given by

$$\epsilon \equiv \frac{1}{M_{Z'}^2 - M_Z^2} \frac{g g_z}{2\cos\theta_w}(z_d v_d^2 + z_u v_u^2)$$

$$= \frac{(M_Z^0)^2}{M_{Z'}^2 - M_Z^2} \frac{2 g_z \cos\theta_w}{g} z_u \sin^2\beta, \tag{3.9}$$

where z_i are the Z' charges of the two Higgs doublets, and g and g_z related to the mass-squared values in absence of mixing $(M_Z^0)^2 = g^2(v_d^2 + v_u^2)/(4\cos^2\theta_w)$ and $(M_{Z'}^0)^2 = g_z^2(z_d^2 v_d^2 + z_u^2 v_u^2 + z_\phi^2 v_\phi^2)$.

The production cross section for this model scales as $(g_z)^2$, as the decay width for this process to leading order in ϵ (Eq. 3.9) is

$$\Gamma_{Z' \to hA^0} = (g_z \cos\alpha \cos\beta)^2 \frac{|p|}{24\pi} \frac{|p|^2}{M_{Z'}^2}. \tag{3.10}$$

where the center of mass momentum for the decay products $|p| = \frac{1}{2M_{Z'}} \sqrt{(M_{Z'}^2 - (m_h + m_{A^0})^2)(M_{Z'}^2 - (m_h - m_{A^0})^2)}.$

To do **Steve Mrenna (?): Total width still comes from qqZ' and chichiZ' couplings? CD: what do you mean? (??)**

3.1.3.1 *Parameter scan*

The model is described by five parameters:

- the pseudoscalar mass M_{A^0},

- the DM mass m_{DM},

- the Z' mass, $M_{Z'}$,

- $\tan\beta(\equiv v_u/v_d)$,

- the Z' coupling strength g_z.

To study the signal production and kinematic dependencies on these parameters, we produced signal samples varying each of the five parameters through MadGraph5_aMC@NLO for the matrix element, PYTHIA for the parton shower, and DELPHES[dF+14] for a parameterized detector-level simulation.

As seen in Fig. 3.14, variations of $\tan\beta$ does not lead to any kinematic difference and the production cross section simply scales as a function of $\tan\beta$. Hence we recommend to fix $\tan\beta$ to unity in the signal generation.

Similarly, variations of g_z do not lead to any kinematic changes. The value of g_z for a given $M_{Z'}$ and $\tan\beta$ can be set according to the maximum value allowed by electroweak global fits and dijet constraints, as described in [BLW14]. Since this parameter does not influence the kinematics, we leave it up to individual analyses on whether they generate benchmark points only according to these external constraints.

Since the DM pair are produced as a result of the decay of A^0, there are minimal kinematic changes when varying m_{DM} as long as $m_{\mathrm{DM}} < M_{A^0}/2$ so that A^0 production is on-shell, as shown in Fig. 3.15 and 3.16 (before detector simulation).

We recommend to produce signal events for a fixed $g_z = 0.8$, $\tan\beta = 1$ and $m_{\mathrm{DM}} = 100$ GeV. For these values, we scan the 2-D parameter space of $M_{Z'}, M_{A^0}$ with $M_{Z'} = 600, 800, 1000, 1200, 1400$ GeV, and $M_{A^0} = 300, 400, 500, 600, 700, 800$ GeV with $M_{A^0} < M_{Z'} - m_h$, for a total of 24 points. The choice of scan is justified by the sensitivity study in [BLW14]: the expected LHC sensitivity for Run-2 is up to $M_{Z'} \sim 1.5$ TeV. For the parameter scan, the DM mass is fixed to 100 GeV. For two $M_{Z'}, M_{A^0}$ value sets, we vary the DM mass to obtain sample cross section for rescaling results. All LO cross sections for the various parameter scan points are reported in Appendix B. The parameter scan excludes the off-shell region, as the cross-sections are suppressed and the LHC would not have any sensitivity to these benchmark points in early data.

The kinematic distributions with varying $M_{Z'}$ for fixed M_{A^0} are shown in Fig. 3.17, while the dependency on M_{A^0} is shown in Fig. 3.18.

This model also allows for an additional source of Higgs plus $\not{E}_T$ signal with a similar kinematics (Fig. 3.19, shown with detector

To do **What about Z' coupling to q and DM? CD: isn't this the DMV model? (??)**

(a) $\not{E}_T$ distribution
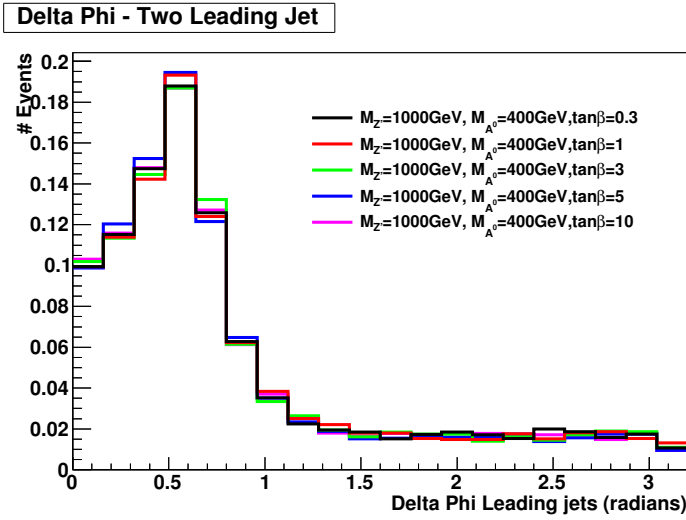
(b) $\Delta\phi$ distance between the two $b-$ jets

Figure 3.14: Kinematic distributions of the signal process varying $\tan\beta$, in the case of a Higgs boson decaying into two b quarks, after parameterized detector simulation: no kinematic dependency is observed

simulation samples) to the signal process from the decay of $Z' \rightarrow hZ$, where the Z decays invisibly. The partial decay width for the Z' is:

$$\Gamma_{Z' \rightarrow hZ} = (g_z \cos\alpha \sin\beta)^2 \frac{|p|}{24\pi} \left(\frac{|p|^2}{M_{Z'}^2} + 3\frac{M_Z^2}{M_{Z'}^2} \right), \qquad (3.11)$$

The values for the Z' masses scanned for those samples should follow those of the previous samples, namely values of $M_{Z'} = 600, 800, 1000, 1200, 1400$ GeV. This signal process has no M_A dependence.

To do **What about visible decays of Z? And isn't monojet still more sensitive? (??)**

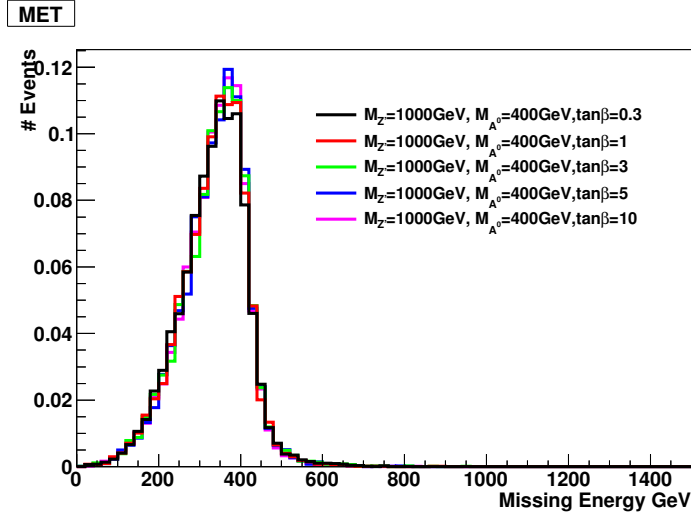THE IMPLEMENTATION OF THESE MODELS IS DISCUSSED IN AP- PENDIX A.2.1.

(a) $\not{E}_T$ distribution

(b) $\Delta\phi$ distance between the two $b-$ jets

Figure 3.15: Kinematic distributions of the signal process varying m_{DM}: minimal kinematic dependency on m_{DM} as expected when A^0 is produced on-shell. Plots shown for $M_{Z'}$ = 1000 GeV, M_{A^0} = 300 GeV.
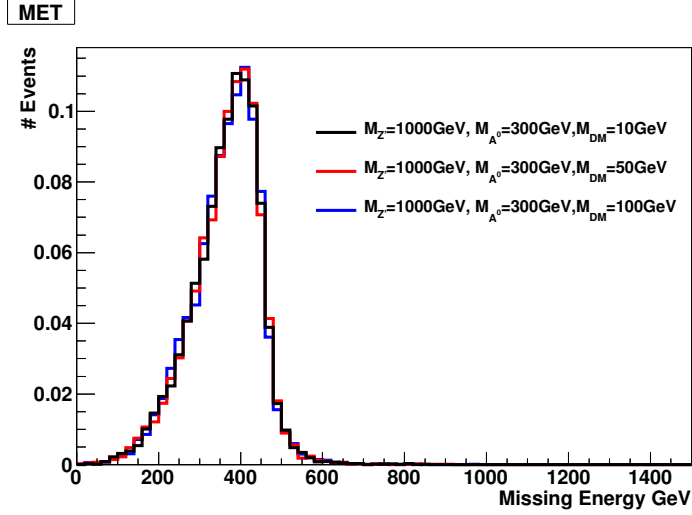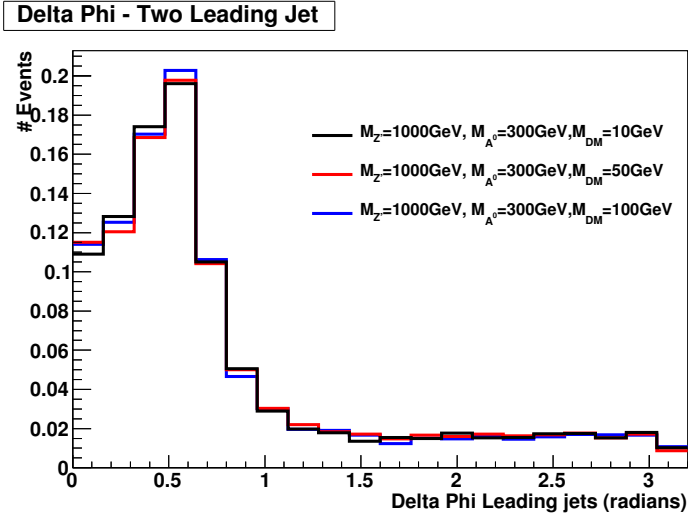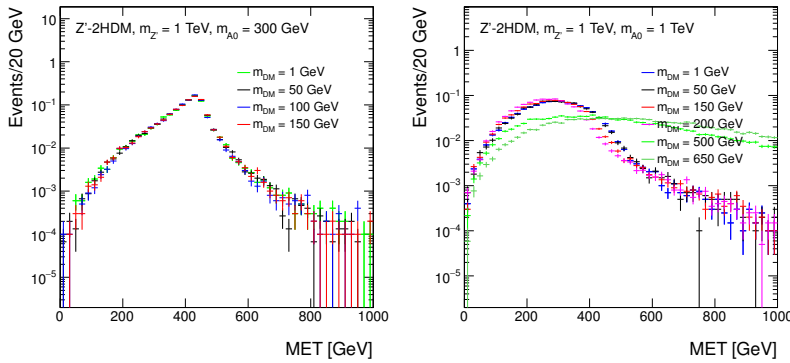
Figure 3.16: Missing transverse momentum distributions at generator level in the Z' +2HDM scenario for different values of the dark matter mass m_{DM}, with $m_{Z'}$ = 1 TeV and m_{A^0} = 300 GeV (left) and m_{A^0} = 1 TeV (right).

3.2 EFT models with direct DM-boson couplings

The EFT operators considered in this section do not have a simplified model completion for Dirac fermion Dark Matter available to date. They provide kinematic distributions that are unique to

mono-boson signatures, and that in most cases are not reproduced by an equivalent simplified model.[2]

A complete list of effective operators with direct DM/boson couplings for Dirac DM, up to dimension 7, can be found in [CHLR13, CNS$^+$13, CHH15]. Higher dimensional operators, up to dimension 8, leading to Higgs+$\not{E}_T$ signatures, are mentioned in [CNS$^+$13, BLW14]. The first part of this Section outlines the main characteristics for a limited number of these models that could be considered in Run-2 searches. However, the EFT approximation made for these operators can be problematic, see Ref. **??** for discussion. For this reason, model-independent results as in Appendix C should be privileged over considering these operators as realistic benchmarks.

However, another consideration that emerged from the Forum discussion was that the EFT approach allows more model-independence when reinterpreting results, making it worth still having results available in terms of these operators. Furthermore, once simplified models are available for those operators, EFT results can be used as a limiting case for consistency checks. We devote the end of this Section to a discussion on the presentation of results from this model, including an assessment of their reliability using a conservative procedure that is only dependent on EFT parameters.

3.2.1 *Dimension 5 operators*

The lowest dimension benchmark operators we consider are effective dimension 5, such as the one depicted in Figure 3.20.

Following the notation of [CNS$^+$13], models from this category have a Lagrangian that includes terms such as:

$$\frac{m_W^2}{\Lambda_5^3}\,\bar{\chi}\chi\,W^{+\mu}W_\mu^- + \frac{m_Z^2}{2\Lambda_5^3}\,\bar{\chi}\chi\,Z^\mu Z_\mu\,, \qquad (3.12)$$

where m_Z and m_W are the masses of the Z and W boson, W^μ and Z^μ are the fields of the gauge bosons, χ denotes the Dark Matter fields and Λ_5 is the effective field theory scale . Note that these operators are of true dimension 7, but reduce to effective dimension 5 once the Higgs vacuum expectation values, contained in the W and Z mass terms, are inserted. As such, one expects these that operators would naturally arise in UV complete models where Dark Matter interacts via a Higgs portal where heavy mediators couple to the Higgs or other fields in an extended Higgs sector. In such models the full theory may be expected to contain additional operators with Higgs-Dark Matter couplings [DFMQ13].

Concentrating on mono-gauge boson signals, the above operator induces signatures with $\not{E}_T$ in conjunction with Z and W bosons at tree level, while at loop level it induces couplings to photon pairs and $Z\gamma$ through W loops. In these models, a clear relation exists between final states with photons, EW bosons and Higgs boson.

[2] Wherever this is the case, we recommend only the generation of simplified model result as the results can be rescaled and reinterpreted.

To do **The nomenclature in different models differs from literature: Λ_5 vs λ (??)**

As shown in Fig. 3.21 kinematics of this model can be approximated by that of a simplified model including a high-mass scalar mediator exchanged in the s-channel described in Section 2.2.2. For this reason, the list of benchmark models with direct boson-DM couplings for photon, Z and W only includes dimension 7 operators: the scalar model with initial state radiation of an EW boson is already recommended and its results can be rescaled.

The Higgs+$\not{E}_T$ analysis, however, will not consider the scalar simplified model as benchmark, due to the very low sensitivity in early LHC analyses, and will instead use this dimension 5 operator.

3.2.1.1 Parameter scan

The two parameters of this model are the scale of new physics λ and the DM particle mass. SM-DM coupling and new physics scale are related by $g_{DM} = (246 \text{ GeV})/\lambda$. .

The initial value of the new physics scale λ chosen for the sample generation is 3 TeV; this is a convention and does not affect the signal kinematics; the cross-section of the samples can be rescaled according to the λ^3 dependence when deriving the constraints on this scale. However, more care should be given when rescaling Higgs+$\not{E}_T$ operators of higher dimensions, as different diagrams have a different λ dependence.

The DM mass values for the benchmark points to be simulated are chosen to span a sufficient Dark Matter range leading to different kinematics, that is within the LHC sensitivity for early searches and that is consistent across the various signatures and EFT operators. We therefore start the mass scan at $m_{DM} =$1 GeV, where collider experiments are complementary to direct and indirect detection and choose the last point corresponding to a DM mass of 1 TeV. We recommend a scan in seven mass points, namely:

$$m_{DM} = 1, 10, 50, 100, 200, 400, 800, 1300 \text{ GeV}.$$

A set of kinematic distributions from the Higgs+$\not{E}_T$ signature where the Higgs decays into two $b-$quarks is shown in Fig. 3.22, for points similar to those of the grid scan proposed.

3.2.2 Dimension 7 operators

The dimension-7 benchmark models contain the $SU(2)_L \times U(1)_Y$ gauge-invariant couplings between DM fields and the kinetic terms of the EW bosons. The CP-conserving scalar couplings of this type can be written as

$$\frac{c_1}{\Lambda_S^3} \bar{\chi}\chi \, B_{\mu\nu} B^{\mu\nu} + \frac{c_2}{\Lambda_S^3} \bar{\chi}\chi \, W_{\mu\nu}^i W^{i,\mu\nu} . \qquad (3.13)$$

Here $B_{\mu\nu} = \partial_\mu B_\nu - \partial_\nu B_\mu$ and $W_{\mu\nu}^i = \partial_\mu W_\nu^i - \partial_\nu W_\mu^i + g_2 \epsilon^{ijk} W_\mu^j W_\mu^k$ are the $U(1)_Y$ and $SU(2)_L$ field strength tensor, respectively, and g_2 denotes the weak coupling constant. In the case of the pseudoscalar

To do **Clarify the reason why this happens in MadGraph5_aMC@NLO through explicit Lagrangian terms? (??)**

To do **Waiting for plot by Bhawna Gomber showing this (??)**

To do **Include unpublished study of rescaling for dimension-8 operators by N. Whallon in dimension-8 section. (??)**

couplings, one has instead

$$\frac{c_1}{\Lambda_P^3} \, \bar{\chi}\gamma_5\chi \, B_{\mu\nu}\tilde{B}^{\mu\nu} + \frac{c_2}{\Lambda_P^3} \, \bar{\chi}\gamma_5\chi \, W_{\mu\nu}^i \tilde{W}^{i,\mu\nu} \, , \qquad (3.14)$$

where $\tilde{B}_{\mu\nu} = 1/2\,\epsilon_{\mu\nu\lambda\rho}B^{\lambda\rho}$ and $\tilde{W}_{\mu\nu}^i = 1/2\,\epsilon_{\mu\nu\lambda\rho}W^{i,\lambda\rho}$ are the dual field strength tensors. In addition to the CP-conserving interactions (3.13) and (3.14), there are also four CP-violating couplings that are obtained from the above operators by the replacement $\bar{\chi}\chi \leftrightarrow \bar{\chi}\gamma_5\chi$.

The effective interactions introduced in (3.13) and (3.14) appear in models of Rayleigh DM [WY12]. Ultraviolet completions where the operators are generated through loops of states charged under $U(1)_Y$ and/or $SU(2)_L$ have been proposed in [WY13] and their LHC signatures have been studied in [LSWY13]. If these new charged particles are light, the high-p_T gauge bosons that participate in the $\not{E}_T$ processes considered here are able to resolve the substructure of the loops. This generically suppresses the cross sections compared to the EFT predictions [HKU13], and thus will weaken the bounds on the interaction strengths of DM and the EW gauge bosons to some extent. Furthermore, the light charged mediators may be produced on-shell in pp collisions, rendering direct LHC searches potentially more restrictive than $\not{E}_T$ searches. Making the above statements precise would require further studies beyond the timescale of this forum.

Since for $\Lambda_S = \Lambda_P$ the effective interactions (3.13) and (3.14) predict essentially the same value of the mono-photon, mono-Z and mono-W cross section [CNS+13, CHH15], we consider below only the former couplings. We emphasize however that measurements of the jet-jet azimuthal angle difference in $\not{E}_T + 2j$ events may be used to disentangle whether DM couples more strongly to the combination $B_{\mu\nu}B^{\mu\nu}$ ($W_{\mu\nu}^i W^{i,\mu\nu}$) or the product $B_{\mu\nu}\tilde{B}^{\mu\nu}$ ($W_{\mu\nu}^i \tilde{W}^{i,\mu\nu}$) of field strength tensors [CHLR13, CHH15].

After EW symmetry breaking the interactions (3.13) induce direct couplings between pairs of DM particles and gauge bosons. The corresponding Feynman rule reads:

$$\frac{4i}{\Lambda_S^3} \, g_{V_1 V_2} \left(p_1^{\mu_2} p_2^{\mu_1} - g^{\mu_1\mu_2} \, p_1 \cdot p_2 \right) , \qquad (3.15)$$

where p_i (μ_i) denotes the momentum (Lorentz index) of the vector field V_i and for simplicity the spinors associated with the DM fields have been dropped. The couplings $g_{V_i V_j}$ take the form:

$$
\begin{aligned}
g_{\gamma\gamma} &= c_w^2 c_1 + s_w^2 c_2 \, , \\
g_{\gamma Z} &= -s_w c_w \left(c_1 - c_2 \right) , \\
g_{ZZ} &= s_w^2 c_1 + c_w^2 c_2 \, , \\
g_{WW} &= c_2 \, ,
\end{aligned}
\qquad (3.16)
$$

with s_w (c_w) the sine (cosine) of the weak mixing angle. Note that our coefficients c_1 and c_2 are identical to the coefficients C_B and

C_W used in [CHH15], while they are related via $k_1 = c_w{}^2 c_1$ and $k_2 = s_w{}^2 c_2$ to the coefficients k_1 and k_2 introduced in [CNS$^+$13].

The coefficients c_1 and c_2 appearing in (3.16) determine the relative importance of each of the $\not{E}_T$ channels and their correlations. For example, one observes that:

- Only c_2 enters the coupling between DM and W bosons, meaning that only models with $c_2 \neq 0$ predict a mono-W signal;

- If $c_1 = c_2$ the mono-photon (mono-Z) signal does not receive contributions from diagrams involving Z (photon) exchange;

- Since numerically $c_w^2/s_w^2 \simeq 3.3$ the mono-photon channel is particularly sensitive to c_1.

3.2.2.1 *Parameter scan*

As stated above and shown in Ref. [NCC$^+$14], the kinematic distributions for dimension-7 scalar and pseudoscalar operators only shows small differences. This has been verified from a generator-level study: the signal acceptance after a simplified analysis selection ($\not{E}_T > 350$ GeV, leading jet $p_T > 40$ GeV, minimum azimuthal difference between either of the two jets and the $\not{E}_T$ direction > 0.4) is roughly 70% for both. We therefore only suggest to generate one of the two models.

The differences in kinematics for the various signatures are negligible when changing the coefficients c_1 and c_2, since these coefficient factorize in the matrix element. Only the case $c_1 = c_2 = 1$ is generated as benchmark; other cases are left for reinterpretation as they will only need a rescaling of the cross-sections.

3.2.3 *Higher dimensional operators*

Many higher dimensional operators can induce signals of photons or $W/Z/H$ bosons in the final state. A complete list can be found in Refs. [CDM$^+$14, BLW14, PS14] and references therein.

Although with lower priority with respect to the operators above, a representative dimension-8 operators can be chosen as benchmark, with the form:

$$\frac{1}{\Lambda^4} \bar{\chi} \gamma^\mu \chi B_{\mu\nu} H^\dagger D^\nu H$$

In this case, the new physics scale is Λ is connected with the coupling of the DM as $y_\chi = \dfrac{1}{\Lambda^4}$. An advantage of this operator is that it includes all signatures with EW bosons, allowing to assess the relative sensitivity of the various channels with the same model. The kinematics for this operator is different with respect to other operators, leading to a harder $\not{E}_T$ spectrum, as illustrated by comparing the leading $b-$jet distribution for the dimension 5 operator to the dimension 8 operator.

To do **Is more detail needed here? (??)**

3.2.4   *Validity of EW contact operators and possible completions*

It is important to remember that the operators described in this section may present problems in terms of the validity of the contact interaction approach for the energy scales reached at the LHC.

As outlined in [BLW14], designing very high $\not{E}_T$ search signal regions that are exclusively motivated by the hard $\not{E}_T$ spectra of the dimension 7 and 8 operators will mean that the momentum transfer in the selected events is larger. This in turn means that processes at that energy scale (mediators, particles exchanged in loops) are accessible, and a simple contact interaction will not be able to correctly describe the kinematics of these signals.

Contact interaction operators like the ones in this section remain useful tools for comparison of the sensitivity of different search channels, and for reinterpretation of other models under the correct assumptions. To date, there are no UV-complete models available for most of those operators: dimension-7 operators are particularly challenging since their completion involves loops [3].
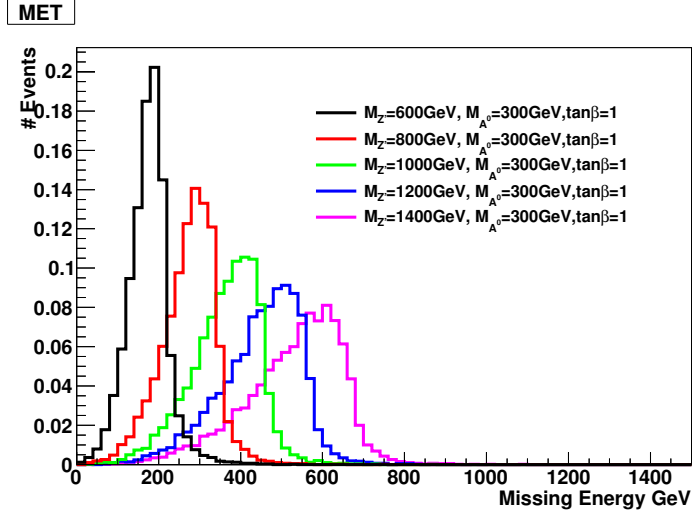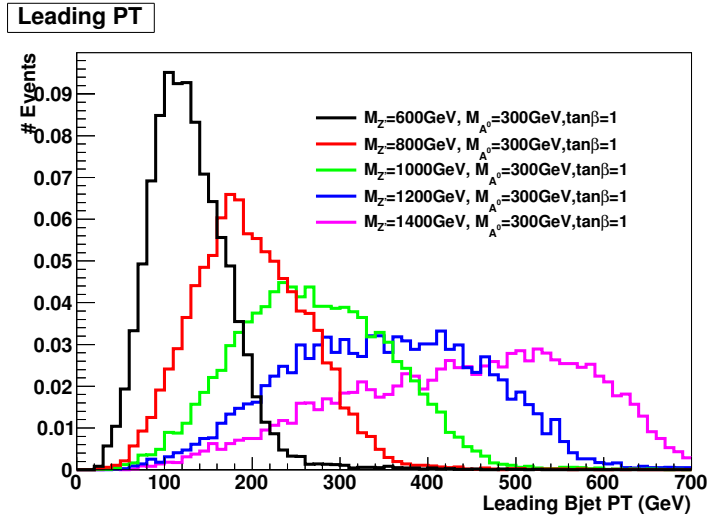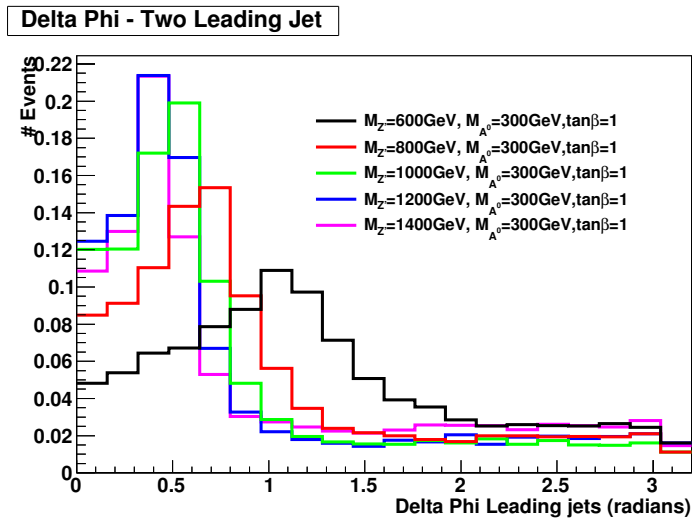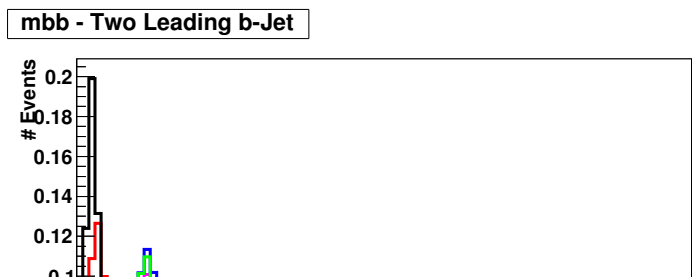
However, this may be the focus of future theoretical exploration, as discussed in Ref. [CHH15]. An example of a complete model for scalar DM corresponding to the dimension-5 operator is provided in the Appendix B. Providing results for the pure EFT limit of these models will prove useful to cross-check the implementation of future.

Given these considerations, the recommendations on the presentation of the results for these models are:

- Deliver fiducial limits on the cross section of any new physics events, without any model assumption, according to the guidelines in Appendix C.

- Assess the percentage of events that pass a condition of validity for the EFT approximation that only depends, and present results removing of the invalid events using the procedure in Section 4 alongside the raw EFT results;

THE IMPLEMENTATION FOR THESE MODELS IS DISCUSSED IN APPENDIX A.2.2.

[3] An example case for the need of loop completions is a simplified model with an additional scalar exchanged at tree level. The scalar couples to *WW* and *ZZ* in a gauge-invariant way, Integrating out the mediator does not lead to the Lorentz structure of a dimension-7 operator, so it is not possible to generate dimension-7 operators that satisfy gauge and Lorentz invariance at the same time. A model with a spin-1 mediator cannot be considered as an candidate for completion either, since dimension-7 operators only have scalar or pseudoscalar couplings.

MET

(a) $\not{E}_T$ distribution

Leading PT

(b) Leading $b-$jet p_T distribution

Delta Phi - Two Leading Jet

(c) $\Delta\phi$ distance between the two $b-$ jets

mbb - Two Leading b-Jet

Figure 3.17: Kinematic distributions of the signal process varying $M_{Z'}$, for $m_{DM} = 100$ GeV, $M_{A^0} = 300$ GeV.
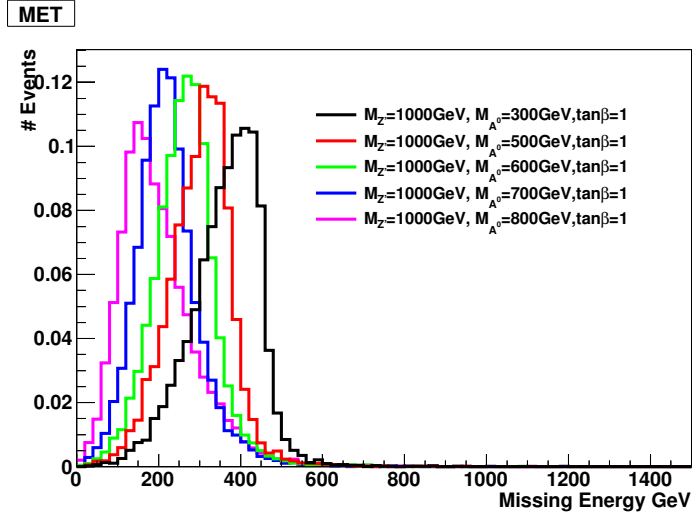
(a) $\not{E}_T$ distribution
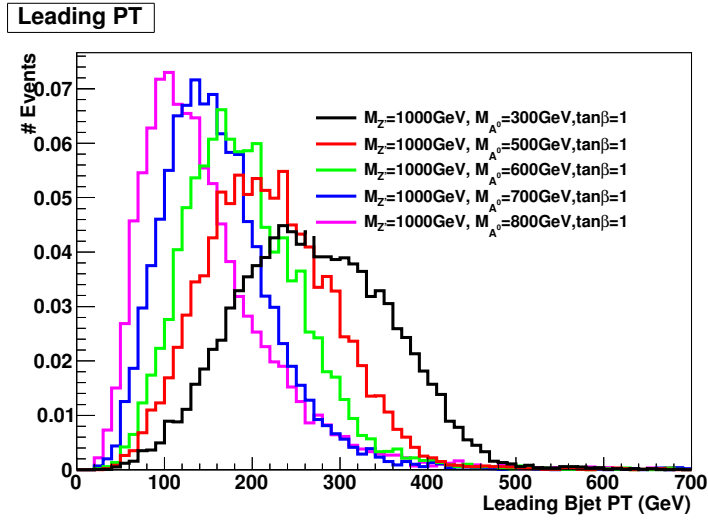
(b) Leading $b-$jet p_T distribution
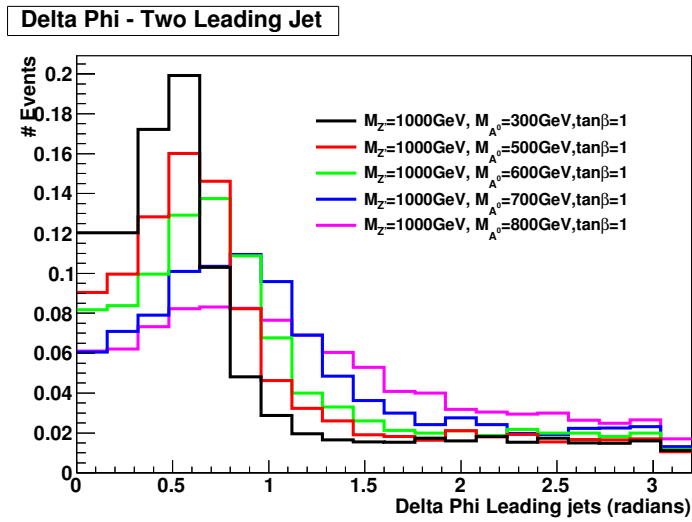
(c) $\Delta\phi$ distance between the two $b-$ jets
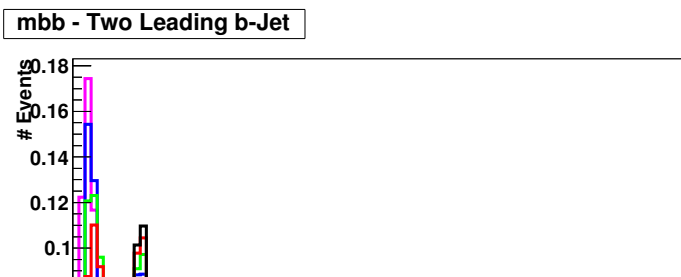
Figure 3.18: Kinematic distributions of the signal process varying M_{A^0}, for $m_{\mathrm{DM}} = 100$ GeV, $M_{Z'} = 1000$ GeV.
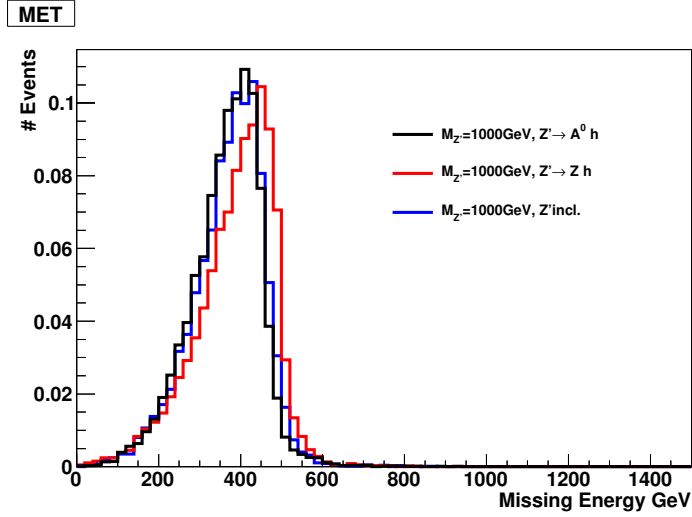
(a) $\not{E}_T$ distribution
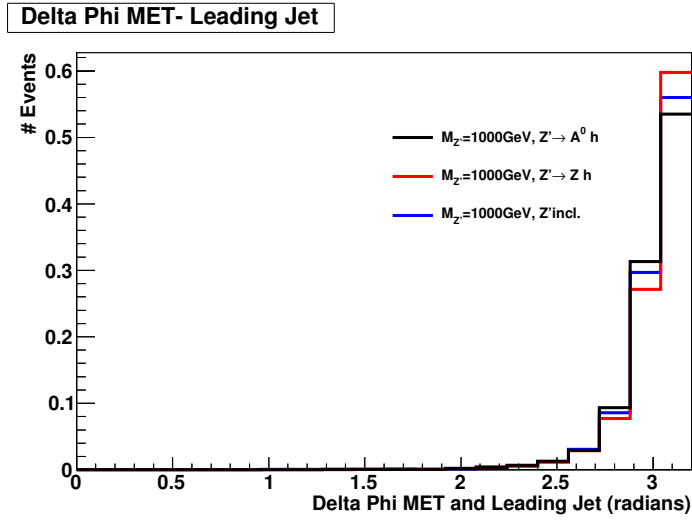
(b) Leading $b-$jet p_T distribution
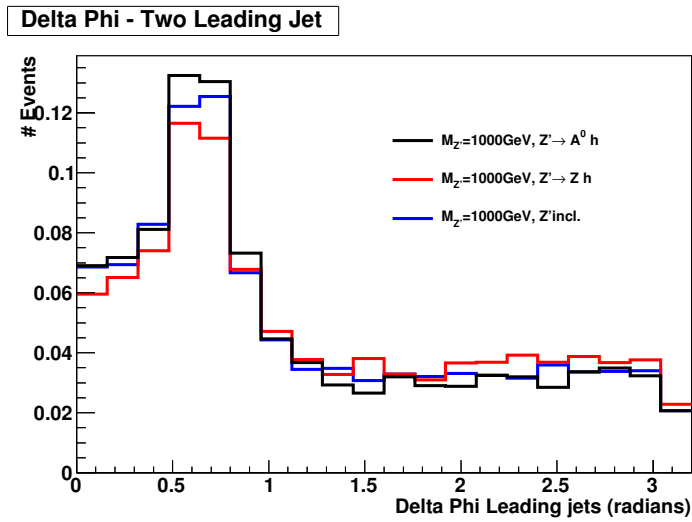
(c) $\Delta\phi$ distance between the two $b-$ jets
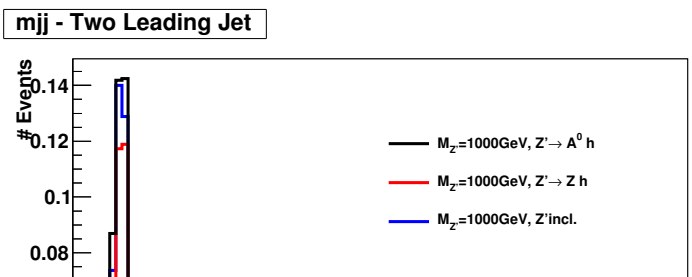
Figure 3.19: Kinematic distributions of $Z' \rightarrow A^0 h$ exclusive production, $Z' \rightarrow Zh$ exclusive production and Z' inclusive production for $M_{Z'} = 1000$ GeV and $M_{A^0} = 300$ GeV
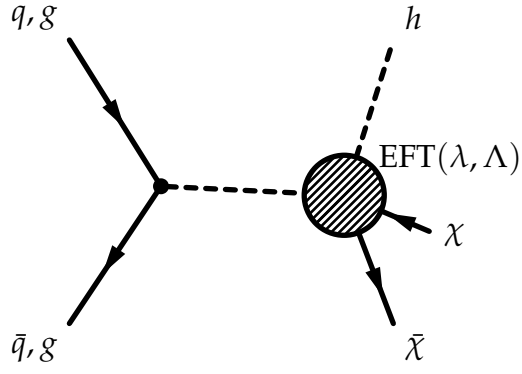
Figure 3.20: Diagram for EFT operators giving rise to a Higgs+$\not{E}_T$ signature.
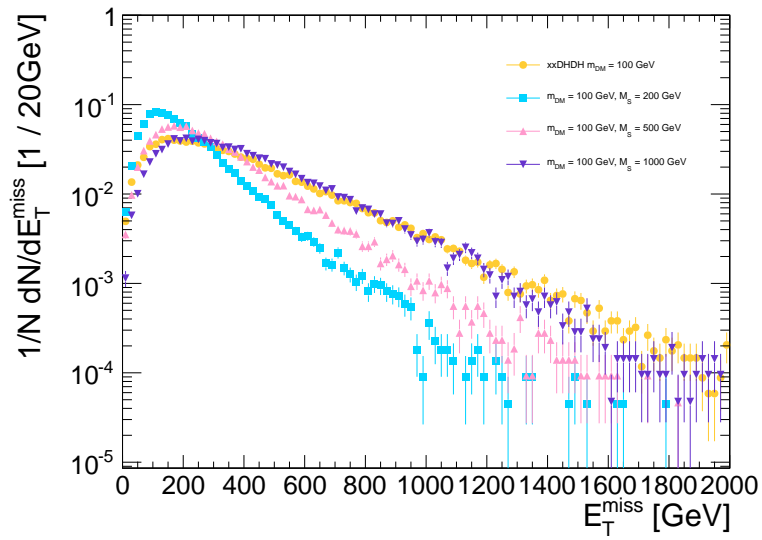
Figure 3.21: Comparison of the missing transverse momentum for the simplified model where a scalar mediator is exchanged in the s-channel and the model including a dimension-5 scalar contact operator, in the leptonic $Z+\not{E}_T$ final state
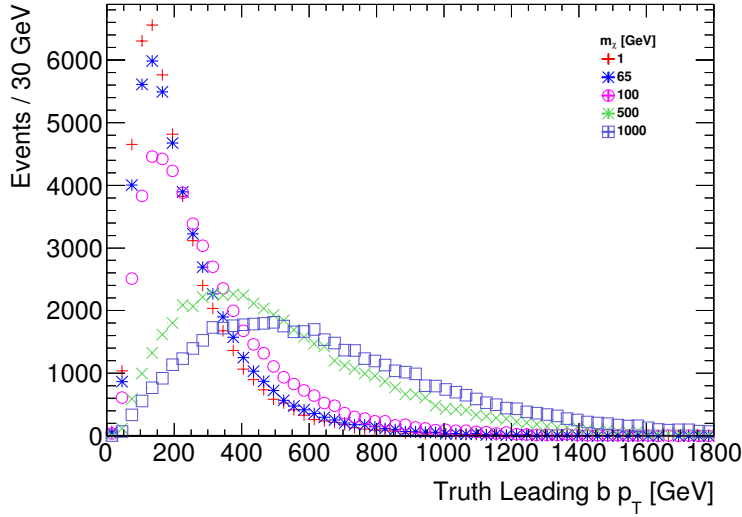
(a) Leading $b-$jet transverse momentum
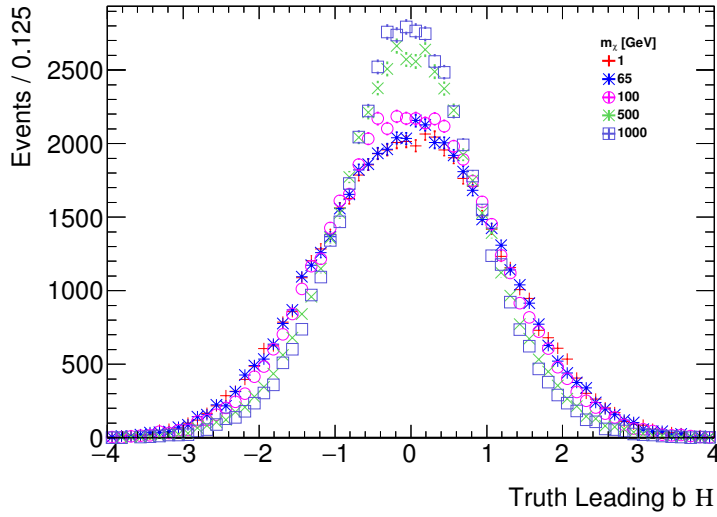
(b) Leading $b-$jet pseudorapidity
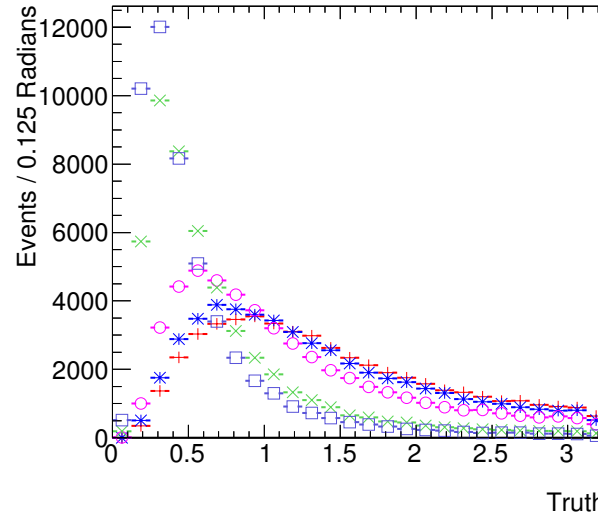
(c) Angular distance between the two leading $b-$je

Figure 3.22: Comparison of the kinematic distributions for the two leading $b-$ jets (from the Higgs decay) in the model with direct interactions between the Higgs boson and the DM particle, when varying the DM mass.
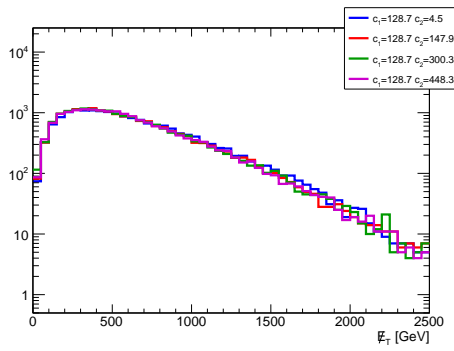
(a) Missing transverse momentum distribution.
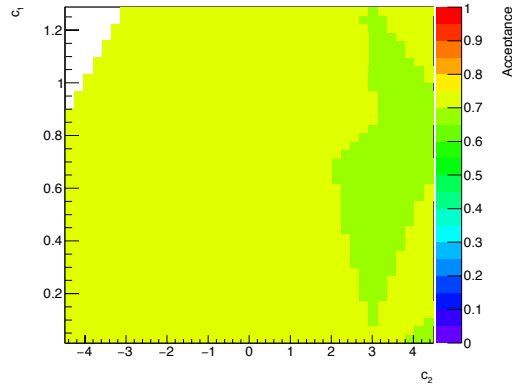
Figure 3.23: $\not{E}_T$ distribution and acceptance for the dimension-7 model with a hadronically decaying Z in the final state, for the scalar and pseudoscalar operators representing direct interactions between DM and bosons. The y axis units are multiplied by 100.

(b) Acceptance.
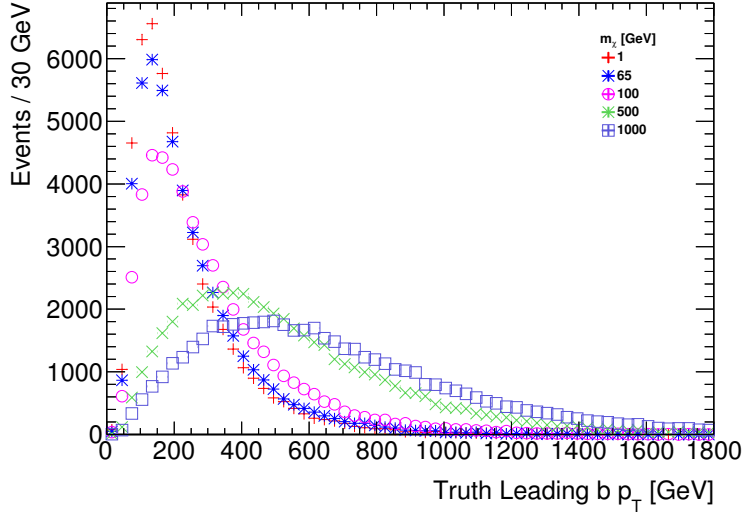
(a) Dimension 5 operator
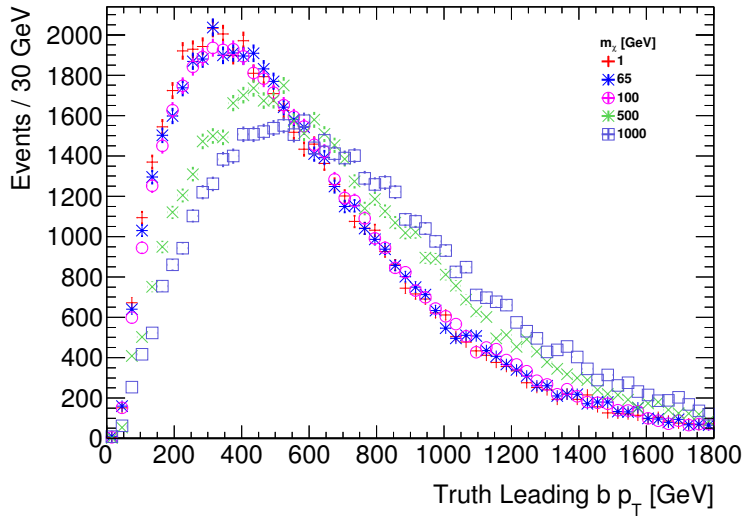
(b) Dimension 7 operator

Figure 3.24: Comparison of the transverse momentum for the leading $b-$ jet from the Higgs decay for a dimension 5 and dimension 7 operator with direct boson-DM couplings.

4

Presentation of EFT results

Most of this report has focused on simplified models. In this Chapter, we wish to emphasize the applicability of Effective Field Theories (EFTs) in the interpretation of DM searches at the LHC. Given our current lack of knowledge about the nature of a DM particle and its interactions, it appears mandatory to provide the necessary information for a model independent interpretation of the collider bounds. This approach should be complemented with an interpretation within a choice of simplified models. We note that, even though EFT benchmarks are only valid in given conditions, the results provided by the current list of simplified models cannot always characterize the breadth of SM-DM interactions. In at least one case, composite WIMPs [Nus85, Kap92, BFT10], the contact interaction framework is the correct one to constrain new confinement scales.

A problematic situation is the attempt to derive a limit on nucleon-dark matter scattering cross sections from EFT results based on collider data. Experiments that directly probe the nucleon-dark matter scattering cross section are testing the regime of small momentum transfers, where the EFT approximation always holds. Collider experiments, though, are sensitive to large momentum transfers: this is a regime where careful treatment is necessary since the condition of applicability of the EFT may not hold [1] The correct approach is to assess the applicability of EFT, not abandon it.

Ideally, experimental constraints should be shown as bounds of allowed signal events in the kinematic regions considered for the search, as detailed in Appendix C. Comparisons between constraints from different experiments meant to highlight their complementarity should be expressed as a function of the model parameters rather than on derived observables; however this is a point that should be developed further after the conclusion of the work of this Forum. Until the various communities have agreed upon how to present this comparison, collider results using contact interaction operators can be presented using one of the several prescriptions in the literature [BDSMR14, BDSG$^+$14, BDSJ$^+$14, ATL15d, RWZ15] that can be used to quote bounds on EFTs.

We first illustrate the problem that can arise with EFTs at collid-

[1] Furthermore, mapping EFT results from high to low momentum requires particular care for some of the operators, see Ref. ?? for a thorough discussion.

ers by considering an effective interaction

$$\mathcal{L}_{\text{int}} = (\bar{\psi}\gamma_\mu\psi)(\bar{\chi}\gamma^\mu\chi)\frac{g}{\Lambda^2}$$

that couples SM ψ and DM χ fields.[2] The strength of this inter-action can be parametrized by $\frac{1}{M_*^2} = \frac{g}{\Lambda^2}$. A monojet signature can be generated from this operator by applying perturbation theory in the QCD coupling (assuming ψ is a quark, for example). An experimental search will place a limit on M_*. For a fixed M_*, a small value of g will correspond to a small value of Λ. The EFT approximation breaks down if $Q > \Lambda$, where Q is a typical hard scale of the process. The limit on small g can only be reliable if the kinematic region $Q > \Lambda$ is removed from the event generation. However, if a fraction of events is removed from the prediction, the corresponding value of g must increase. On the other hand, if, for the same value of M_*, a large Λ is assumed so that the full set of events fulfill the EFT validity condition, a large value of g is required, raising the question if perturbation theory is even applicable.

In the first part of this Chapter, we summarize two methods that have been advocated to truncate events that do not fulfill the condition necessary for the use of an EFT. These methods are described in detail in Refs. [BDSMR14, BDSG⁺14, BDSJ⁺14, ATL15d, RWZ15, BLW14]. We then propose a recommendation for the presentation of EFT results for early Run-2 LHC searches.

4.1   *Procedures for the truncation of EFT benchmark models*

4.1.1   *EFT truncation using the momentum transfer and information on UV completion*

In the approach described in Ref. [BDSG⁺14], the main modification to the EFT prediction is to incorporate the propagator of a relatively light mediator. For a tree-level interaction between DM and the SM via some mediator with mass M_{med}, the EFT approximation corresponds to expanding the propagator for the mediator in powers of $Q_{\text{tr}}^2/M_{\text{med}}^2$, truncating at lowest order, and combining the remaining parameters into a single parameter M_* (connected to the scale of the interaction Λ in the literature). For an example scenario with a Z'-type mediator (leading to some combination of operators D5 to D8 in the notation of **??** for the EFT limit), this corresponds to setting

$$\frac{g_{\text{DM}}g_{\text{q}}}{Q_{\text{tr}}^2 - M_{\text{med}}^2} = -\frac{g_{\text{DM}}g_{\text{q}}}{M_{\text{med}}^2}\left(1 + \frac{Q_{\text{tr}}^2}{M_{\text{med}}^2} + \mathcal{O}\left(\frac{Q_{\text{tr}}^4}{M_{\text{med}}^4}\right)\right) \simeq -\frac{1}{M_*^2},$$

$$(4.1)$$

where Q_{tr} is the momentum carried by the mediator, and g_{DM}, g_{q} are the DM-mediator and quark-mediator couplings respectively.[3] A minimal condition that must be satisfied for this approximation

[2] The *exact* operator chosen is not important.

[3] Here, we ignore potential complications from the mediator width when the couplings are large.

to be valid is that $Q_{tr}^2 < M_{med}^2 = g_{DM}g_q M_*^2$. This requirement avoids the regions: $Q_{tr}^2 \sim M_{med}^2$, in which case the EFT misses a resonant enhancement, and it is conservative to ignore this enhancement; and $Q_{tr}^2 \gg M_{med}^2$, in which case the signal cross section should fall according to a power of Q_{tr}^{-1} instead of M_{med}^{-1}. The latter is the problematic kinematic region.

The condition $Q_{tr}^2 < M_{med}^2 = g_{DM}g_q M_*^2$ was applied to restrict the kinematics of the signal and remove events for which the high-mediator-mass approximation made in the EFT would not be reliable. This leads to a smaller effective cross-section, after imposing the event selection of the analysis. This truncated signal was then used to derive a new, more conservative limit on M_* as a function of $(m_{DM}, g_{DM}g_q)$.

For the example D5-like operator, $\sigma \propto M_*^{-4}$, and there is a simple rule for converting a rescaled cross section into a rescaled constraint on M_*. if the original limit is based on a simple cut-and-count procedure. Defining σ_{EFT}^{cut} as the cross section truncated such that all events pass the condition $\sqrt{g_{DM}g_q}M_*^{rescaled} > Q_{tr}$, we have

$$M_*^{rescaled} = \left(\frac{\sigma_{EFT}}{\sigma_{EFT}^{cut}(M_*^{rescaled})} \right)^{1/4} M_*^{original}, \qquad (4.2)$$

which can be solved for $M_*^{rescaled}$ via either iteration or a scan. Similar relations exist for a given UV completion of each operator. The details and application of this procedure to ATLAS results can be found in Ref. [ATL15d] for a range of operators. We reiterate: knowledge of the UV completion for a given EFT operator was necessary for this procedure; this introduces a model-dependence that was not present in the non-truncated EFT results.

Currently, simplified models are available for comparison with the data, and since knowledge of the simplified models is needed, there is no reason to apply this prescription. Instead, the simplified model limit for large M_* can be presented for interpretation in terms of EFT operators.

4.1.2   EFT truncation using the center of mass energy

The procedure presented in the previous section was predicated on some knowledge of the simplified model. This led to the identification of the mass of the DM pair as the relevant kinematic quantity to use in a truncation procedure. In general, if no assumption is made about the underlying dynamics, it is more conservative to place a limit on the total center of mass energy E_{cm} of the DM production process. Furthermore, the direct connection between the mass scale of the EFT validity, M_{cut}, and the

mass scale that normalizes the EFT operator, M_*, is unknown. For such cases, Refs.[RWZ15, BLW14] proposed a procedure to extract model independent and consistent bounds within the EFT that can be applied to any effective Lagrangian describing the interactions between the DM and the SM. This procedure provides

conservative limits that can be directly reinterpreted in any completion of the EFT. The condition ensuring that the EFT approximation is appropriate is:

$$E_{\rm cm} < M_{\rm cut} \,. \tag{4.3}$$

The relationship between $M_{\rm cut}$ and M_* can be parameterized by an *effective coupling strength* g_*, such that $M_{\rm cut} = g_* M_*$. A scan over values of g_* provides an indication of the sensitivity of the prediction to the truncation procedure. In the Z'-type model considered above, g_* is equal to $\sqrt{g_{\rm DM} g_{\rm q}}$. The resulting plots are shown in [RWZ15] for a particular effective operator.

The advantage of this procedure is that the obtained bounds can be directly and easily recast in any completion of the EFT, by computing the parameters M_*, $M_{\rm cut}$ in the full model as functions of the parameters of the complete theory. On the other hand, the resulting limits will be weaker than those obtained using $Q_{\rm tr}$ and a specific UV completion.

4.1.3 *Comments on unitarity considerations*

A further consideration applicable to EFT operators at hadron colliders is the potential violation of unitarity. An analysis of the operator $\dfrac{\bar{q}\gamma_\mu q \bar{\chi}\gamma^\mu\chi}{M_*^2}$ provides the limit:

To do **Waiting for input from J. Alcaraz (??)**

$$M_* > \sqrt{s}\sqrt{\frac{\sqrt{3}}{4\pi}\beta(s)}, \tag{4.4}$$

where $\sqrt{s}$ is (maximally) the collider energy and $\beta(s)$ is the DM velocity [SV12]. Constraints for other operators have also been derived [?]. This constraint on M_* still is open to interpretation, since the relation to $M_{\rm cut}$ is not resolved, except for a specific simplified model.

4.1.4 *Consideration for shape analyses*

If a search is not simply a counting experiment and exploits the shapes of kinematic distributions, any of the two conditions on the momentum transfer should be applied on the benchmarks using generator level information, by discarding events that are invalid, and the limit derived from the truncated shape must be recalculated. This provides the necessary rescaling of the cross section while keeping the information on the change in the kinematic distributions due to the removal of the invalid events.

4.1.5 *Sample results of EFT truncation procedures*

An example of the application of the two procedures to the limit on M_* from Ref. [ATL14d] as a function of the product of the couplings is shown in Figure 4.3. Only the region between the dashed and the solid line is excluded. It can be seen that the procedure

1744 from [RWZ15] outlined in Section 4.1.2, shown in blue, is more
1745 conservative than the procedure from Refs. [BDSG⁺14, ATL15d],
1746 described in Section 4.1.1.

Figure 4.1: 95% CL lower limits on the scale of the interaction of the D5 operator at 14 TeV, after the two truncation procedures. The procedure from [RWZ15] outlined in Section 4.1.2 is shown in blue, while the procedure from Refs. [BDSG⁺14, ATL15d], described in Section 4.1.1 is shown in red. Only the region between the dashed and the solid lines is excluded.

1747 A further consideration applicable to EFT operators at hadron
1748 colliders is the potential violation of unitarity. An analysis of the
1749 operator $\frac{\bar{q}\gamma_\mu q \bar{\chi}\gamma^\mu \chi}{M_*^2}$ provides the limit:

$$M_* > \sqrt{s}\sqrt{\frac{\sqrt{3}}{4\pi}\beta(s)}, \tag{4.5}$$

1750 where $\sqrt{s}$ is (maximally) the collider energy and $\beta(s)$ is the DM
1751 velocity [SV12]. Constraints for other operators have also been de-
1752 rived [?]. This constraint on M_* still is open to interpretation, since
1753 the relation to M_{cut} is not resolved, except for a specific simplified
1754 model.

4.2   *Recommendation for presentation of EFT results*

1756 In this report, we make two recommendations for the presenta-
1757 tion of collider results in terms of Effective Field Theories for the
1758 upcoming Run-2 searches. A full discussion of the presentation of
1759 collider results in relation to other experiments is left to work be-
1760 yond this Forum, where ATLAS, CMS, the theory community and
1761 the Direct and Indirect Detection communities are to be involved.
1762 We divide the EFT operators in two categories: those that can
1763 be mapped to one or more UV-complete simplified models, such
1764 as those commonly used in LHC searches so far and detailed
1765 in [GIR⁺10], and those for which no UV completion is available,
1766 such as those outlined in Section 3.2.

4.2.1   *EFT benchmarks with corresponding simplified models*

1768 If a simplified model can be mapped to a given EFT, then the
1769 model's high-mediator-mass limit will converge to the EFT. Numer-

ically, for 14 TeV studies, we have determined that to fully repro-

duce the kinematics of a contact interaction and have no remaining

dependence on the presence of a resonance that is as narrow as

the choice made in Section 2.1.2 (g_q = 0.25 and g_{DM} = 1), the me-

diator mass needs to be at least 10 TeV. A comparison of the main

kinematic variables for the *s*-channel vector mediator model with a

width of $0.1 M_{med}$[4] is shown in Fig. 4.2.

[4] The use of a fixed width rather than the minimal width is exclusive of these plots

Figure 4.2: Comparison of the kinematic distributions at 14 TeV between a narrow *s*-channel mediator and the corresponding D5 contact operator, at generator level for a jet+$\not{E}_T$ signature.
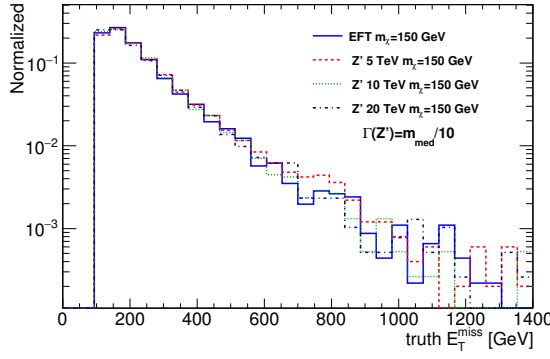
(a) $\not{E}_T$
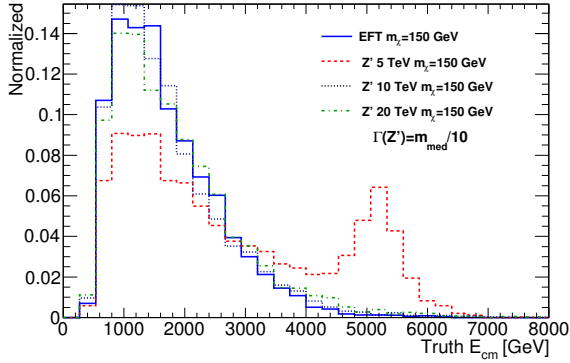
(b) Center of mass energy E_{cm}
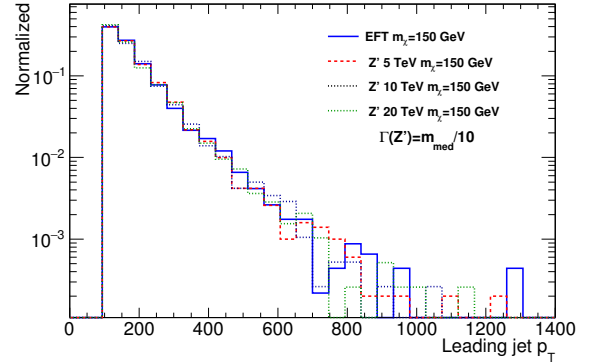
(c) Mediator transverse momentum
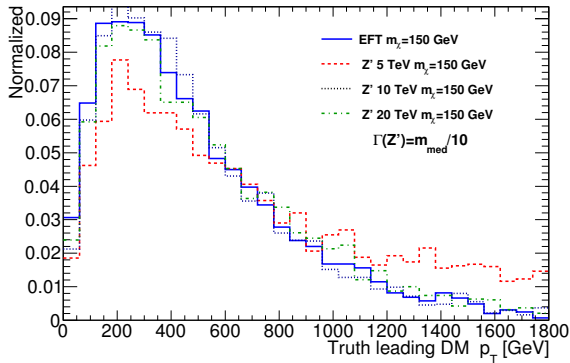
(d) DM transverse momentum (leading)
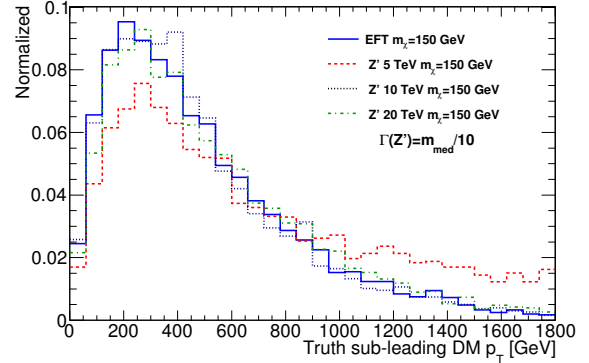
(e) DM transverse momentum (sub-leading)

To do We may get plots with a width.mass ratio of 0.05, which is closer to the minimal width. (??)

As already observed in Section 2.1.2, varying the DM mass

changes the kinematics, both in the simplified model and in the

EFT case. This can be seen in Fig. 4.3.
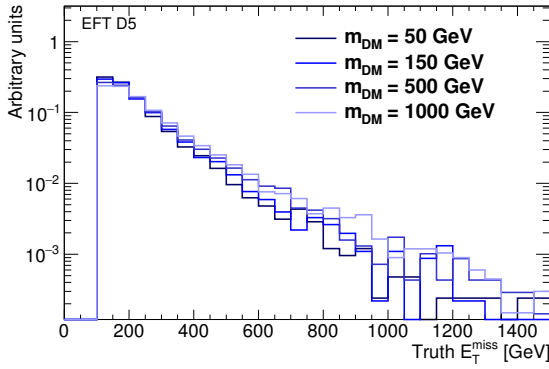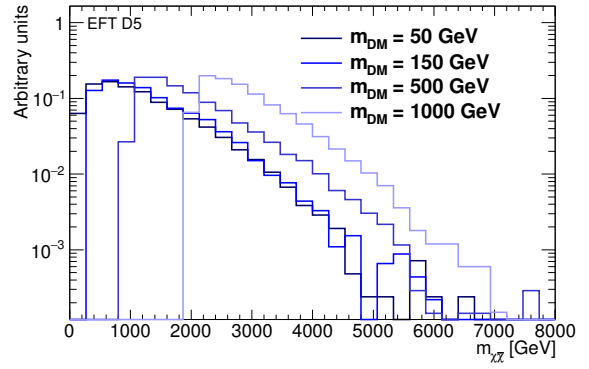
(a) $\not{E}_T$, D5 operator

(b) Invariant mass of the two WIMPs $m_{\chi\chi}$, D5 operator
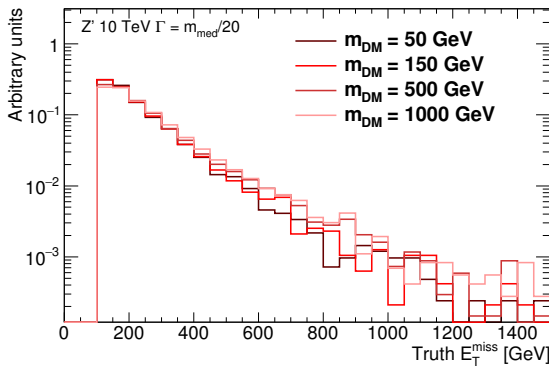
(c) $\not{E}_T$, simplified model
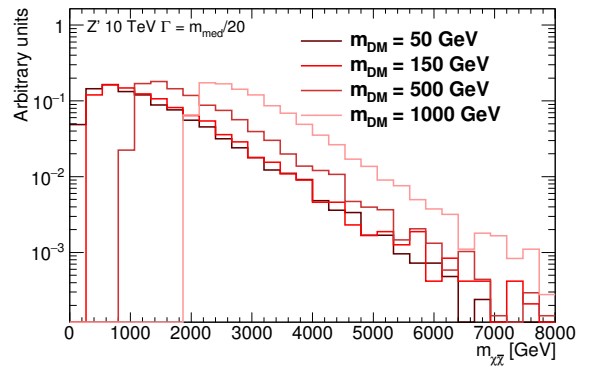
(d) Invariant mass of the two WIMPs $m_{\chi\chi}$, simplified model

Based on these studies, the Forum recommends experimental collaborations to deliver results for mediators with a mass of 10 TeV instead of fully simulated EFT results for each of the DM masses considered in the scan, and leave further reinterpretation to theorists. It should be checked that the high-mass mediator case for the simplified model is correctly implemented We therefore advise to add one grid scan point at very high mediator mass (10 TeV) to the scan, for each of the DM masses for the simplified models described in Section 2.

Figure 4.3: Comparison of the kinematic distributions for a narrow *s*-channel mediator, at generator level for a jet+$\not{E}_T$ signature, for varying DM masses.

To do **The extrapolation to other couplings and mediator masses can be done using the Q_{tr} prescription for that model. CD: I think this was Steve M - what do you mean? (??)**

4.2.2   *EFT benchmarks with no corresponding simplified models*

Whenever a UV completion is not available, EFT results are still a source of useful information as described in Section 3.2.4. However, we can only roughly control how well the EFT approximation holds. Despite the fact that a propagator was introduced to motivate the truncation procedure for *s*-channel models, the prescription from Sec. 4.2.1 depends upon the simplified model to derive the energy scaling that is used for the comparison with the momentum transfer. The simple fact remains that the effective coupling of the operator – g/Λ^n – should not allow momentum flow $Q > \Lambda$ or $g > 4\pi$. Given our ignorance of the actual kinematics, the truncation procedure recommended for this purpose is the one described in Section 4.1.2, as it is independent from any UV completion de-

1802 tails.

1803   Because there is no UV completion, the parameter M_{cut} can be
1804 treated more freely than an explicit function of g and Λ. It makes
1805 sense to choose M_{cut} such that we identify the transition region
1806 where the EFT stops being a good description of UV complete
1807 theories. This can be done using the ratio R, which is defined as the
1808 fraction of events for which $\hat{s} > M_{\text{cut}}^2$. For large values of M_{cut}, no
1809 events are thrown away in the truncation procedure, and R=1. As
1810 M_{cut} becomes smaller, eventually all events are thrown away in the
1811 truncation procedure, i.e. $R = 0$, and the EFT gives no exclusion
1812 limits for the chosen acceptance.

1813   We propose a rough scan over M_{cut}, such that we find the values
1814 of M_{cut} for which R ranges from 0.1 to 1. The analysis can then
1815 perform a scan over several values of M_{cut}, and show the truncated
1816 limit for each one of them alongside the naive limit corresponding
1817 to R =1.

5
Evaluation of signal theoretical uncertainties

[Comment on proper PDF sets to use, concerns about sea quark PDF in b-initiated diagrams (perhaps the latter belongs in the b-flavored DM section]

5.1 POWHEG

A comprehensive and careful assessment of theoretical uncertainties plays a much more important role for the background estimations (especially when their evaluation is non-entirely data-driven) than it does for signal simulations. Nevertheless, when using POWHEG it is possible to study scale and PDF errors for the dark matter signals. A fast reweighting machinery is available in POWHEG-BOX that allows one to add, after each event, new weights according to different scale or PDF choices, without the need to regenerate all the events from scratch.

To enable this possibility, the variable `storeinfo_rwgt` should be set to 1 in the POWHEG input file when the events are generated for the first time[1]. After each event, a line starting with

`#rwgt`

is appended, containing the necessary information to generate extra weights. In order to obtain new weights, corresponding to different PDFs or scale choice, after an event file has been generated, a line

`compute_rwgt 1`

should be added in the input file along with the change in parameters that is desired. For instance, `renscfact` and `facscfact` allow one to study scale variations on the renormalization and factorization scales around a central value. By running the program again, a new event file will be generated, named `<OriginalName>-rwgt.lhe`, with one more line at the end of each event of the form

`#new weight,renfact,facfact,pdf1,pdf2`

followed by five numbers and a character string. The first of these numbers is the weight of that event with the new parameters

[1] Notice that even if the variable is not present, by default it is set to 1.

chosen. By running in sequence the program in the reweighting
mode, several weights can be added on the same file. Two remarks
are in order.

- The file with new weights is always named

  ```
  <OriginalName>-rwgt.lhe
  ```

  hence care has to be taken to save it as

  ```
  <OriginalName>.lhe
  ```

  before each iteration of the reweighting procedure.

- Due to the complexity of the environment where the program
  is likely to be run, it is strongly suggested as a self-consistency
  check that the first reweighting is done keeping the initial pa-
  rameters. If the new weights are not exactly the same as the
  original ones, then some inconsistency must have happened, or
  some file was probably corrupted.

It is possible to also have weights written in the version 3 Les
Houches format. To do so, in the original run, at least the token

```
lhrwgt_id 'ID'
```

must be present. The reweighting procedure is the same as de-
scribed above, but now each new run can be tagged by using a
different value for the lhrwgt_id keyword. After each event, the
following lines will appear:

```
<rwgt>
<wgt id='ID'>
<wgt id='ID1'>
</rwgt>
```

A more detailed explanation of what went into the computation
of every single weight can be included in the <header> section of
the event file by adding/changing the line

```
lhrwgt_descr 'some info'
```

in the input card, before each "reweighting" run is performed.
Other useful keywords to group together different weights are
lhrwgt_group_name and lhrwgt_group_combine.

More detailed information can be obtained by inspecting the
document in /Docs/V2-paper.pdf under the common POWHEG-
BOX-V2 directory.

5.2   MADGRAPH5_AMC@NLO *and* SYSCALC

SYSCALC is a package for use with MADGRAPH5_AMC@NLO that
can calculate dedicated event weights for certain theoretical system-
atic uncertainties. The output is an XML-based file with all relative

weights embedded. These weights can then be used to account for the different systematic uncertainties, namely variations on the α_s emission scale factors, factorization (μ_F) and normalization (μ_R) scales, matching scales, and different parton distribution function (PDF) sets.

The requirements of the package as inputs are :

- A systematics file (which can be generated by MadGraph 5 v. 1.6.0 or later) [A$^+$14b, AHM$^+$11].

- The Pythia-PGS package (v. 2.2.0 or later) [SMS06]. This is needed only in the case of matching scales variations.

- The availability of LHAPDF5 [WBG05].

- A configuration file (i.e. a text file) specifying the parameters to be varied.

SysCalc supports all leading order computations generated in MadGraph5_aMC@NLO including fixed-order computation and matched-merged computation performed in the MLM scheme [MMPT07]. MadGraph5_aMC@NLO stores additional information inside the event in order to have access to all the information required to compute the convolution of the PDFs with the matrix element for the various supported systematics.

Below follows an example configuration file which could serve as an example:

```
# Central scale factors
scalefact:
0.5 1 2
# Scale correlation
# Special value -1:  all combination (N**2)
# Special value -2:  only correlated variation
# Otherwise list of index N*fac_index + ren_index
#    index starts at 0
scalecorrelation:
-1
# αₛ emission scale factors
alpsfact:
0.5 1 2
# matching scales
matchscale:
30 40 80
# PDF sets and number of members (optional)
PDF:
CT10.LHgrid 53
MSTW2008nlo68cl.LHgrid
```

Without matching/merging, SysCalc is able to compute the variation of renormalisation and factorisation scale (parameter `scalefact`) and the change of PDFs. The variation of the scales can be done in a correlated and/or uncorrelated way, basically following the value of the `scalecorrelation` parameter which can take the following values:

- -1 : to account for all N^2 combinations.

- -2 : to account only for the correlated variations.

- A set of positive values corresponding to the following entries (assuming *0.5, 1, 2* for the `scalefact` entry):

  0: $\mu_F = \mu_F^{\text{orig}}/2$, $\mu_R = \mu_R^{\text{orig}}/2$

  1: $\mu_F = \mu_F^{\text{orig}}/2$, $\mu_R = \mu_R^{\text{orig}}$

  2: $\mu_F = \mu_F^{\text{orig}}/2$, $\mu_R = \mu_R^{\text{orig}} * 2$

  3: $\mu_F = \mu_F^{\text{orig}}$, $\mu_R = \mu_R^{\text{orig}}/2$

  4: $\mu_F = \mu_F^{\text{orig}}$, $\mu_R = \mu_R^{\text{orig}}$

  5: $\mu_F = \mu_F^{\text{orig}}$, $\mu_R = \mu_R^{\text{orig}} * 2$

  6: $\mu_F = \mu_F^{\text{orig}} * 2$, $\mu_R = \mu_R^{\text{orig}}/2$

  7: $\mu_F = \mu_F^{\text{orig}} * 2$, $\mu_R = \mu_R^{\text{orig}}$

  8: $\mu_F = \mu_F^{\text{orig}} * 2$, $\mu_R = \mu_R^{\text{orig}} * 2$

Without correlation, the weight associated to the renormalisation scale is the following:

$$\mathcal{W}_{\text{new}}^{\mu_R} = \frac{\alpha_S^N(\Delta * \mu_R)}{\alpha_S^N(\mu_R)} * \mathcal{W}_{\text{orig}}, \tag{5.1}$$

where Δ is the scale variation considered, $\mathcal{W}_{\text{orig}}$ and $\mathcal{W}_{\text{new}}$ are respectively the original/new weights associated to the event. N is the power in the strong coupling for the associated event (interference is not taken account on an event by event basis). The weight associated to the scaling of the factorisation scale is:

$$\mathcal{W}_{\text{new}}^{\mu_F} = \frac{f_{1,\text{orig}}(x_1, \Delta * \mu_F) * f_{2,\text{orig}}(x_2, \Delta * \mu_F)}{f_{1,\text{orig}}(x_1, \mu_F) * f_{2,\text{orig}}(x_2, \mu_F)} * \mathcal{W}_{\text{orig}}, \tag{5.2}$$

where $f_{i,\text{orig}}$ are the probabilities from the original PDF set associated to the incoming partons, which hold a proton momentum fraction x_1 and x_2 for the first and second beam respectively.

The variations for the PDF are given by the corresponding weights associated to the new PDF sets:

$$\mathcal{W}_{\text{new}}^{\text{PDF}} = \frac{f_{1,\text{new}}(x_1, \mu_F) * f_{2,\text{new}}(x_2, \mu_F)}{f_{1,\text{orig}}(x_1, \mu_F) * f_{2,\text{orig}}(x_2, \mu_F)} * \mathcal{W}_{\text{orig}}, \tag{5.3}$$

where $f_{i,\text{new}}$ is the new PDF probability associated to parton i.

In presence of matching, MADGRAPH5_AMC@NLO performs already a scale and PDF rescaling, such that the scale of the strong interaction is set according to a parton shower history (selected via a k_T clustering). SYSCALC can perform the associated re-weighting (parameter `alpsfact`) by dividing and multiplying by the associated factor.

For each vertex of the clustering (associated to a scale μ_i), this corresponds to the following factor for a Final State Radiation :

$$\mathcal{W}_{\text{new}}^{\text{FSR}} = \frac{\alpha_s(\Delta * \mu_i)}{\alpha_s(\mu_i)} * \mathcal{W}_{\text{orig}}, \tag{5.4}$$

and the following expression for Initial State Radiation (associated to a scale μ_i and fraction of energy x_i):

$$\mathcal{W}_{\text{new}}^{\text{ISR}} = \frac{\alpha_s(\Delta * \mu_i)}{\alpha_s(\mu_i)} \frac{\frac{f_a(x_i, \Delta * \mu_i)}{f_b(x_i, \Delta * \mu_{i+1})}}{\frac{f_a(x_i, \mu_i)}{f_b(x_i, \mu_{i+1})}} * \mathcal{W}_{\text{orig}}, \tag{5.5}$$

where μ_{i+1} is the scale of the next vertex in the initial state clustering history.

SysCalc can include the weight associated to different merging scales in the MLM matching/merging mechanism (for output of the `pythia6` package or `pythia-pgs` package). In that case, the parton-shower keeps track of the scale of the first emission and applies then a veto to account for the minimal allowed value for the matching scale according to the cut performed at parton-level. SysCalc will then test for each of the values specified in the parameter `matchscale` if the event passes the MLM criteria or not. If it does not, then a zero weight is associated to the event, while if it does, then a weight 1 is kept. As a reminder, those weights are the equivalent of having a (approximate) Sudakov form-factor and removing at the same time the double counting between the events belonging to different multiplicities.

Finally, we give an example of the SysCalc output which follows the LHEF v3 format. The following block appears in the header of the output file:

```
<header>
  <initrwgt>
    <weightgroup type="Central scale variation" combine="envelope">
      <weight id="1"> mur=0.5 muf=0.5 </weight>
      <weight id="2"> mur=1 muf=0.5 </weight>
      <weight id="3"> mur=2 muf=0.5 </weight>
      <weight id="4"> mur=0.5 muf=1 </weight>
      <weight id="5"> mur=1 muf=1 </weight>
      <weight id="6"> mur=2 muf=1 </weight>
      <weight id="7"> mur=0.5 muf=2 </weight>
      <weight id="8"> mur=1 muf=2 </weight>
      <weight id="9"> mur=2 muf=2 </weight>
    </weightgroup>
    <weightgroup type="Emission scale variation" combine="envelope">
      <weight id="10"> alpsfact=0.5</weight>
      <weight id="11"> alpsfact=1</weight>
      <weight id="12"> alpsfact=2</weight>
    </weightgroup>
    <weightgroup type="CT10nlo.LHgrid" combine="hessian">
      <weight id="13">Member 0</weight>
      <weight id="14">Member 1</weight>
      <weight id="15">Member 2</weight>
      <weight id="16">Member 3</weight>
      ...
      <weight id="65">Member 52</weight>
    </weightgroup>
  </initrwgt>
</header>
```

For each event, the weights are then written as follows:

```
<rwgt>
  <wgt id="1">83214.7</wgt>
  <wgt id="2">61460</wgt>
  <wgt id="3">47241.9</wgt>
  <wgt id="4">101374</wgt>
  ...
  <wgt id="64">34893.5</wgt>
  <wgt id="65">41277</wgt>
</rwgt>
```

6

Conclusions

The conclusions will contain a summary of the recommendation
from the ATLAS/CMS DM Forum report, together with the sum-
mary table below.

Benchmark models for ATLAS and CMS Run-2 DM searches			
vector/axial vector mediator, *s*-channel			
Signature	State of the art calculation	Link to implementation	References
jet + $\not{E}_T$	**NLO+PS (powheg, r3059)**	[For15i, For15l]	[HKR13, ANOR10, Nas04, FNO07, HR15]
	NLO (MCFM)	TBC	[FW13]
	LO+PS (MADGRAPH5_aMC@NLO, v2.2.3)	TBC	[AFF$^+$14, ACD$^+$14, DDF$^+$12]
$W/Z/\gamma + \not{E}_T$	**LO+PS (MadGraph5_aMC@NLO), v2.2.3**	[For15a]	[AFF$^+$14, ACD$^+$14, DDF$^+$12]
scalar/pseudoscalar mediator, *s*-channel			
Signature	State of the art calculation	Link to implementation	References
jet + $\not{E}_T$	**LO+PS, top loop (powheg, r3059)**	[For15k, For15j]	[HKR13, ANOR10, Nas04, FNO07, HR15]
	NLO (MCFM)	TBC	[FW13]
	NLO+PS (MADGRAPH5_aMC@NLO, v2.3.0)	TBC	[AFF$^+$14, HFF$^+$11, ACD$^+$14, DDF$^+$12]
$W/Z/\gamma + \not{E}_T$	**LO+PS (MadGraph5_aMC@NLO), v2.2.3**	TBC	[AFF$^+$14, ACD$^+$14, DDF$^+$12]
$t\bar{t}, b\bar{b} + \not{E}_T$	**LO+PS (MadGraph5_aMC@NLO), v2.2.3**	TBC	[AFF$^+$14, ACD$^+$14, DDF$^+$12]
	NLO+PS (POWHEG, r3059)	TBC	[HKR13, ANOR10, Nas04, FNO07, HR15]
scalar mediator, *t*-channel			
Signature	State of the art calculation	Link to implementation	References
jet(s) + $\not{E}_T$	**LO+PS (MadGraph5_aMC@NLO), v2.2.3**	[For15h]	[PVZ14]
$W/Z/\gamma + \not{E}_T$	**LO+PS (MadGraph5_aMC@NLO), v2.2.3**	TBC	[AFF$^+$14, ACD$^+$14, DDF$^+$12]

Table 6.1: Summary table for recommended benchmark models and
their implementation.

They will also include a series of points to be developed further
beyond the timescale of the Forum. These points will be discussed
at the meeting that marks the conclusion of the works of the Forum,
to be held during the week of June 10th.

A

Appendix: Implementation of Models

A.1 Implementation of s-channel and t-channel models for $\not{E}_T$ +X analyses

There are several matrix element implementations of the DM production through spin-0 and spin-1 mediators. This Appendix collects the generator recommendations and available implementations of these models for different final states, together with studies of the matching between the matrix element and the parton shower.

A.1.1 Implementation of models for mono-jet signature

For a spin-1 mediator, the implementation in POWHEG generates DM pair production with 1 parton at next-to-leading order (NLO), whilst MADGRAPH5_AMC@NLO and MCFM are at leading order (LO) [1]. As shown in POWHEG Ref. [HKR13], including NLO corrections result in an enhancement in the cross section as compared to LO and though this is not significant, it does lead to a substantial reduction in the dependence on the choice of the renormalization and factorization scale and hence the theoretical uncertainty on the signal prediction. Since NLO calculations are available for the process in POWHEG, we recommend to proceed with POWHEG as the generator of choice.

For a spin-0 mediator in the mono-jet final state, the top-quark loop is the most important consideration. The matrix element implementation of the s-channel spin-0 mediated DM production is available in MCFM [FW13, HKSW15] and POWHEG [HR15] with the full top-loop calculation at LO. The POWHEG and MCFM implementations include the full calculation of the top loop for DM pair production with 1 parton at LO. For consistency with the spin-1 generation, we recommend using POWHEG for this case as well.

Here, we document some specific settings needed to run the POWHEG generation for the Dark Matter models. POWHEG parameter cards for all models can be found on the Forum SVN repository [For15i, For15l, For15k?].

- POWHEG can handle the generation of events (be it at LO or NLO) in two different modes explained in the following. The second one is the recommended one. The relevant keywords in the input

[1] spin-0 and spin-1 mediator models will also be provided in the near future to the same precision in MADGRAPH5_AMC@NLO [A+14b].

card are `bornsuppfact` and `bornktmin`.

1. unweighted events:

   `bornsuppfact`: negative or absent

   `bornktmin <PT>`

   This runs the program in the most straightforward way, but most likely it is not the more convenient choice, as will be explained below. POWHEG will generate unweighted events using a sharp lower cut (with value `PT`) on the leading-jet p_T. Since this is a generation cut, the user should make sure that the value used for `bornktmin` is lower than the actual analysis cut to be eventually used. It is good practice to use as a value in the input card a transverse momentum 10-20% smaller than the final analysis cut, and check that the final result is independent, by exploring an even smaller value of `bornktmin`. The drawback of this running mode is that it's difficult to populate well and in a single run both the low-p_T region as well as the high-pT tail.

2. weighted events:

   `bornsuppfact <PTS>`

   `bornktmin <PT>`

   POWHEG will now produce weighted events, thereby allowing to generate a single sample that provides sufficient statistics in all signal regions. Events are still generated with a sharp lower cut set by `bornktmin`, but the `bornsuppfact` parameter is used to set the event suppression factor according to

$$F(k_T) = \frac{k_T^2}{k_T^2 + \texttt{bornsuppfact}^2} \ . \tag{A.1}$$

   In this way, the events at, for instance, low $\not{E}_T$, are suppressed but receive an higher weight, which ensures at the same time higher statistics at high $\not{E}_T$. We recommend to set `bornsuppfact` to 1000.

   The `bornktmin` parameter allows to suppress the low $\not{E}_T$ region even further by starting the generation at a certain value of k_T also in this running mode. It is recommended to set this parameter to half the lower analysis $\not{E}_T$ cut. For instance for the event selection used in the CMS/ATLAS monojet analyses, assuming the lowest $\not{E}_T$ region being defined above 300 GeV, the proposed value for `bornktmin` is 150. However, this parameter should be set keeping in mind the event selection of all the analyses that will use these signal samples and hence a threshold lower than 150 may be required.

- Remove the `runningwidth` keyword, or set it to 0, which is the default value. Running with fixed widths is the recommended option. Although there are limitations, this is the more straightforward, simple and transparent option, and it was used for Forum studies.

To do **Emanuele:"On the usage of fixed or running width. It is my opinion that one should use fixed widths. Although clearly there are limitations, I think this goes into the direction of making all as simple and transparent as possible. Moreover, all the discussions in the last months as well as the large majority of runs were done with fixed widths. Since there was some interest over the last couple of weeks, here is my suggestion for the POWHEG section."** (??)

To do **Steve: The reason I originally asked the question was because we**

While not recommended, the alternative, a running width for the propagator of the s-channel mediator, can be selected by setting runningwidth to 1. In this case the denominator of the mediator's propagator

$$Q^2 - M^2 + i M \Gamma$$

is replaced by

$$Q^2 - M^2 + i Q^2 \frac{\Gamma}{M}$$

where Q is the virtuality of the mediator, and M and Γ are its mass and width respectively. See Ref. [BBB$^+$89] for a discussion.

- Set the parameters defining the bounds on the invariant mass of the Dark Matter pair, mass_low and mass_high, to -1. In this way, POWHEG will assign values internally.

- The minimal values for ncall1, itmx1, ncall2, itmx2 are 250000, 5, 1000000, 5 for the vector model, respectively.

- The minimal values for ncall1, itmx1, ncall2, itmx2 are 100000, 5, 100000, 5 for the scalar top-loop model, respectively.

- When NLO corrections are included (as for instance in the vector model), negative-weighted events could happen and should be kept in the event sample, hence withnegweights should be set to 1. If needed, their fraction can be decreased by setting foldsci and foldy to bigger value (2 for instance). foldphi can be kept to 1.

- Since the scalar model with top-loop is computed as a leading order process, set LOevents and bornonly are set to 1 internally.

- One can benefit from the automatic calculation of systematic uncertainties associated with the choice of hard scale and PDFs as described in Section 5.

A.1.2 Sampling Considerations for Heavy Narrow Mediators

Observations of kinematic changes or cross section suppression in the generated samples do not always come from physics, but may be a consequence of under-sampling phase space in the generator implementation, where a cutoff for the regions far away from the mediator mass is generally used. One must take care to correctly set the width of the Breit-Wigner used for the sampling. This is illustrated in Fig. A.1 showing the invariant mass of the Dark Matter pair in the samples generated in MADGRAPH5_AMC@NLO for a $M_{\text{med}} = 7$ TeV scalar mediator with different coupling strengths, using the default settings bwcutoff equal to 15. In all cases, it is expected to observe a peak around the mediator mass with a tail extending to $m_{\bar{\chi}\chi} \to 0$, significantly enhanced by parton distribution functions at low Bjorken x. For coupling strength 1 and 3, the

massive enhancement at $m_{\bar\chi\chi} \to 0$ implies that resonant production at $m_{\bar\chi\chi} = 7$ TeV is statistically suppressed such that barely any events are generated there. However, for narrower mediators with couplings below 1, the peak around 7 TeV is clearly visible in the generated sample and the dominant tail at $m_{\bar\chi\chi} \to 0$ is artificially cut off, leading to unphysical cross section predictions and kinematic shapes.
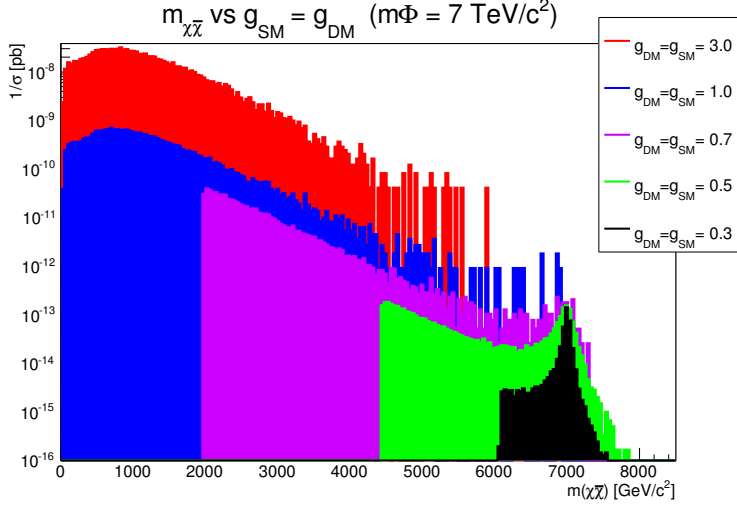
Figure A.1: Invariant mass of the Dark Matter pair in the scalar mediator samples with $m_{DM} = 1$ GeV, $M_{med} = 7$ TeV and different coupling strengths.

A.1.3   *Parton matching studies*

Whenever models for mono-jet final states are generated in MAD-GRAPH5_AMC@NLO, it is necessary to avoid double counting the partons from matrix elements and parton showering in PYTHIA 8 using a parton matching technique. Based on the comparative study in Ref. [A+08], there is some advantage to using the CKKW-L matching scheme. However, the current CKKW-L matching scheme is not amenable to the event generation model of the experimental collaborations. Most large scale event generation is performed using LHE files that have a mix (or "soup") of different parton level processes in each file. This is easy to handle using the MLM matching scheme provided as a PYTHIA 8 plugin.

A.1.3.1   *Implementation of MLM matching*

Here, add the process generation steps, and the matching parameters for LHE file production. Also, provide the PYTHIA 8 configuration to produce hadronic events.

To do **This is probably a TODO for Steve M. (??)**

The validation of matching has been performed extensively by the collaborations for a large number of SM and BSM models, and need not be reproduced here.

In order to describe the signal kinematics correctly and save time during MC production, the parton emissions will only be generated up to a certain multiplicity. The higher multiplicity samples usually have small enough cross sections and the corresponding parts of

To do **CD: I would like to uncomment the details on the implementation of CKKW-L matching as this is what was done in ATLAS so far. (??)**

the phase space can be sufficiently approximated by parton showering in PYTHIA 8. A dedicated study comparing samples generated with up to 1-, 2-, or 3-parton multiplicities was performed, using again the settings for the CKKW-L k_t-merging with the 80 GeV matching scale and the Merging:nJetMax parameter adjusted accordingly. Figure A.2 shows the $\not{E}_T$ distribution of the samples at $\not{E}_T > 250$ GeV.

With an event selection requiring $\not{E}_T$ and the leading jet p_T being larger than 250 GeV and allowing for up to 3 jets with $p_T > 30$ GeV, the sample generated with up to 1 parton has 17.4% smaller yield compared to the sample with up to 3 partons, while the yield of the sample with up to 2 partons is only 2.2% smaller. Note the jet multiplicity cut is important here as the agreement between the two samples improves at higher $\not{E}_T$ when the cut is not applied. A similar comparison is shown in Fig. A.3 for the jet multiplicity in the events with the leadning jet $p_T > 250$ GeV, where an agreement at the level of $\sim 3\%$ between the samples with up to 2 and 3 parton emissions is observed for number of jets up to 7. This justifies it is sufficient to produce samples with up to 2 parton emissions only at the generator level and ignore generating higher parton emissions.

A.1.4 *Implementation of models for EW final states*

These models are generated at leading order with MADGRAPH5_AMC@NLO 2.2.2, using Pythia8 for the parton shower. Parameter cards can be found on the Forum SVN repository [For15a]. No parton matching is required.

A.1.5 *Implementation of models with heavy flavor quark signatures*

The models for the $t\bar{t}$ and $b\bar{b}$ signatures are generated at leading order with MADGRAPH5_AMC@NLO 2.2.2, using Pythia8 for the parton shower. No matching is needed. Parameter cards can be found on the Forum SVN repository [For15d]. No parton matching is required.

We simulate the bFDM model using the MG5_aMC v2.2.3, using Pythia8 for the parton shower. No matching is needed. The corresponding card files can be found on the Forum SVN repository [For15f].

A.1.5.1 *Quark flavor scheme and masses*

In this particular model we recommend an additional care when choosing the flavor scheme generation and whether quarks should be treated as massive or massless.

The production of DM+$b\bar{b}$, Dark Matter in association with b jets via a decay of a (pseudo) scalar boson, is dominated in simplified mediator models by the gluon-gluon initiated production, similar to the production of Z+$b\bar{b}$ at the LHC. The Z+$b\bar{b}$ process has been studied in detail in the Z(ll)+b-jets final state, which can be used to
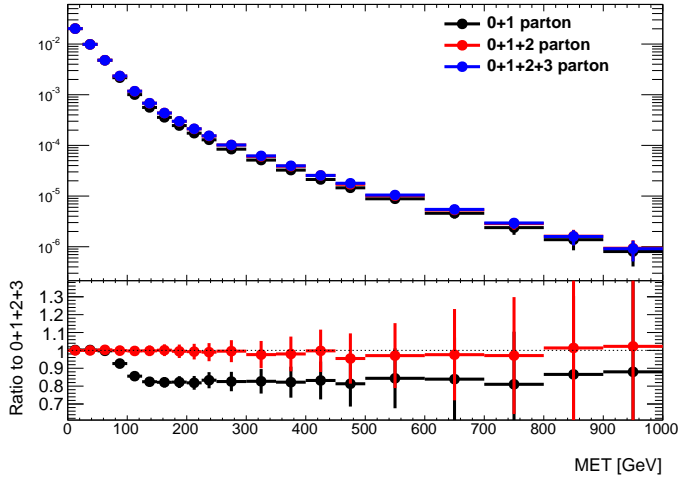
Figure A.2: Missing transverse momentum distributions for EFT D5 sample with CKKW-L matching scale at 80 GeV produced with maximum 1 (black), 2 (red) and 3 (blue) partons emitted at the generator level. The ratios are shown with respect to the latter sample.

(a) No jet multiplicity cut

(b) $N_{jet} \leqslant 3$

Figure A.3: Multiplicity of jets with $p_T > 30$ GeV and $|\eta| < 2.8$ for EFT D5 sample with CKKW-L matching scale at 80 GeV produced with maximum 1 (black), 2 (red) and 3 (blue) partons emitted at the generator level. The ratios are shown with respect to the latter sample. The leading jet p_T is required to be larger than 250 GeV.

validate both the modeling of DM+bb and, its main background, $Z(\nu\nu)+b\bar{b}$. In this context, the p_T of the Z boson is related to the

observed MET, whereas the *b*-jet kinematics determines the ratio of mono-*b*/di-*b* signatures in the detector.

For basic kinematic criteria applied to Z+$b\bar{b}$ production, this process leads in $\sim$ 90% of the events to a signature with only 1 *b*-jet in the acceptance ('Z+1*b*-jet production') and only in $\sim$ 10% of the events to a signature with 2 *b*-jets in the detector ('Z+2*b*-jets production). The production cross section of the Z+$b\bar{b}$ process are calculated in the 'five-flavor scheme', where b quarks are assumed massless, and the 'four-flavor scheme', where massive b quarks are used [CEMW04, MMW05, CEMW06], and data favor the cross-section predictions in the five-flavor scheme [C$^+$14]. We therefore recommend to calculate the cross sections of these models in the 5-flavor scheme, as in the repository. The PDF used to calculate these cross section is NNPDF3.0 (lhaid 263000).

It is found that the best modeling of two *b*-quarks final states is achieved using a 4-flavor scheme and a massive treatment of the *b*-quarks [C$^+$14, C$^+$13, Col15]. We recommend to use in the generation NNPDF3.0 set (lhaid 263400). Since figure A.4 shows that there is no significant difference in the kinematics between either flavor scheme used for DM+$b\bar{b}$ production, we recommend the 4-flavor scheme to follow the observation in the Z+$b\bar{b}$ measurements.
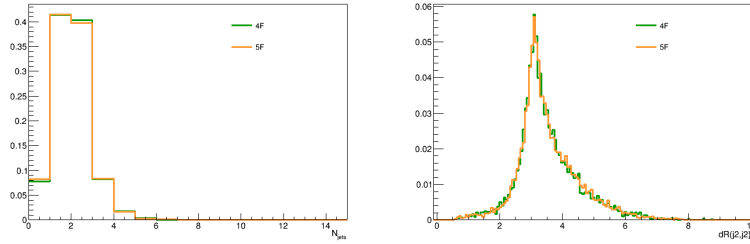
Figure A.4: Comparison of the jet multiplicity (left) and angular correction $\Delta R(j_1, j_2)$ (right) for the DM+$b\bar{b}$ scalar model generated in the 4-flavor and 5-scheme. The samples are generated for $m_\chi = 1$ GeV and $m_\phi = 10$ GeV.

A.2   Implementation of specific models for $V + \not{E}_T$ analyses

A.2.1   Model implementation for mono-Higgs models

All three Higgs+$\not{E}_T$ models are generated at leading order with MadGraph5_aMC@NLO 2.2.2, using pythia 8 for the parton shower. No matching is needed. The MadGraph5_aMC@NLO implementations of the scalar and vector models can be found on the Forum SVN repository [For15g], while the 2HDM model can be found at this link [For15b].

In all cases, it is recommended not to handle the *h* decay through MadGraph5_aMC@NLO as it does not include the proper *h* branching ratios, or, if using MadGraph5_aMC@NLO, then the resulting cross section should be rescaled to match onto the correct branching ratio.

MadGraph5_aMC@NLO details for scalar mediator Higgs+MET model

In this model, the contribution from the *gghS* box is included

through an effective Lagrangian evaluated in the large m_t limit. This may overestimate the rates of the $h + \not{E}_T$ signal [HKU13], but a full evaluation is left to future studies.

MADGRAPH5_AMC@NLO DETAILS FOR 2HDM HIGGS+MET MODEL

The two couplings that can be changed in the implemented model follow the nomenclature below:

- Tb - $\tan \beta$

- gz - g_z, gauge coupling of Z' to quarks

The other couplings are not changed, including gx (the $A\bar{\chi}\chi$ coupling) which has little impact on the signal. $\sin \alpha$ is fixed internally such that $\cos(\beta - \alpha) = 0$. The width of the Z' and A can be computed automatically within MADGRAPH5_AMC@NLO. The couplings here don't affect the signal kinematics, so they can be fixed to default values and then the signal rates can be scaled appropriately.

The nomenclature for the masses in the implemented model is:

- MZp - PDG ID 32 - Z'

- MA0 - PDG ID 28 - A

- MX - PDG ID 1000022 - dark matter particle

The other masses are unchanged and do not affect the result. Both $Z' \to hZ(\bar{\nu}\nu)$ and $Z' \to hA(\bar{\chi}\chi)$ contribute to the final state, scaling different with model parameters. We recommend to generate them separately, and then add the two signal processes together weighted by cross sections.

A.2.2   *Implementation of EFT models*

These models are generated at leading order with MADGRAPH5_AMC@NLO 2.2.2, using PYTHIA 8 for the parton shower. No matching is performed. Parameter cards can be found on the Forum SVN repository: [For15g] for operators with Higgs+MET final states and [For15c] for $W/Z/\gamma$ final states.

B

Appendix: Additional models for Dark Matter searches

B.1 *Models with a single top−quark + $\not{E}_T$*

Many different theories predict final states with a single top and associated missing transverse momentum (monotop), some of them including dark matter candidates. A simplified model encompassing the processes leading to this phenomenology is described in Refs. [AFM11, AAB$^+$14, BCDF15], and is adopted as one of the benchmarks for Run 2 LHC searches.

The simplified model is constructed by imposing that the model Lagrangian respects the electroweak $SU(2)_L \times U(1)_Y$ gauge symmetry and by requiring minimality in terms of new states to supplement to the Standard Model fields. As a result, two monotop production mechanisms are possible. In the first case, the monotop system is constituted by an invisible (or long-lived with respect to detector distances) fermion χ and a top quark. It is produced, as shown in the diagram of B.1 (a) where a colored resonance φ lying in the triplet representation of $SU(3)_C$ decays into a top quark and a χ particle. In the second production mode, the monotop state is made of a top quark and a vector state V connected to a hidden sector so that it could decay invisibly into, e.g., a pair of dark matter particles as studied in [BCDF15]. The production proceeds via flavor-changing neutral interactions of the top quark with a quark of the first or second generation and the invisible V boson (see the diagrams of B.1 (b) and (c)).

Resonant production

In this case, a colored 2/3-charged scalar (φ) is produced and decays into a top quark and a spin-1/2 invisible particle, χ. The dynamics of the new sector is described by the following Lagrangian:

$$\mathcal{L} = \left[\varphi \bar{d}^c \left[a_{SR}^q + b_{SR}^q \gamma_5 \right] d + \varphi \bar{u} \left[a_{SR}^{1/2} + b_{SR}^{1/2} \gamma_5 \right] \chi + \text{h.c.} \right], \qquad \text{(B.1)}$$

where u (d) stands for any up-type (down-type) quark, the notation SR refers to the monotop production mechanism via a scalar resonance and all flavor and color indices are understood for clarity.

In the notation of [AAB$^+$14], the couplings of the new colored fields to down-type quarks are embedded into the 3×3 antisym-
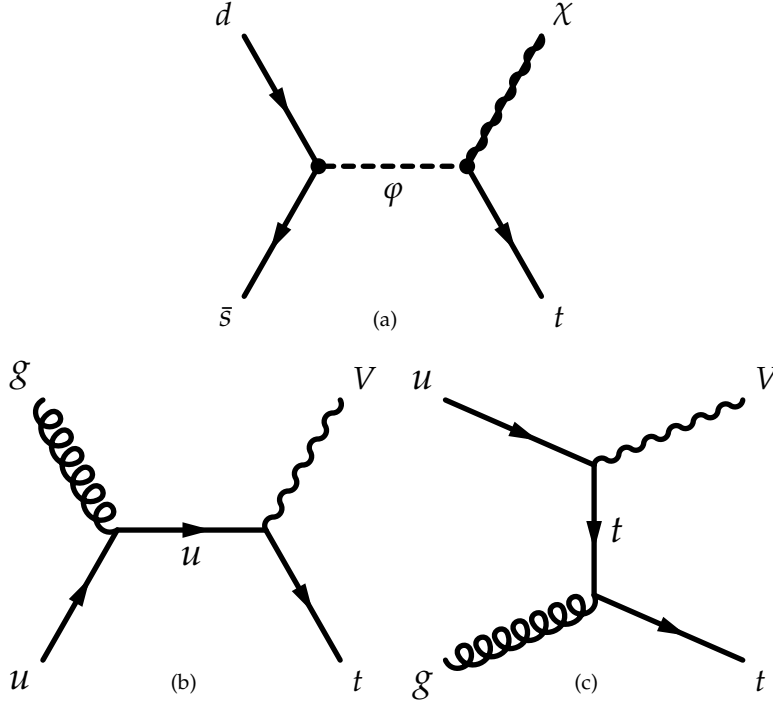
Figure B.1: Feynman diagrams of leading order processes leading to monotop events: production of a coloured scalar resonance φ decaying into a top quark and a spin-1/2 fermion χ (a), $s-$ (b) and t-channel (c) non resonant production of a top quark in association with a spin-1 boson V decaying invisibly.

metric matrices a_{SR}^q (scalar couplings) and b_{SR}^q (pseudoscalar couplings) while those to the new fermion χ and one single up-type quark are given by the three-component vectors $a_{SR}^{1/2}$ and $b_{SR}^{1/2}$ in flavor space.

Under the form of Eq. (B.1), the Lagrangian is the one introduced in the original monotop search proposal [AFM11]. It has been used by the CMS collaboration for Run I analyses after neglecting all pseudoscalar components of the couplings and adding the vector resonance case for which minimality requirements are difficult to accommodate [CMS15b]. In contrast, the study of Ref. [BCDF15] has imposed electroweak gauge invariance and required minimality. This enforces all new couplings to be right-handed so that

$$a_{SR}^{1/2} = b_{SR}^{1/2} = \frac{1}{2}y_s^* \qquad \text{and} \qquad a_{SR}^q = b_{SR}^q = \frac{1}{2}\lambda_s \,, \qquad \text{(B.2)}$$

where the objects y_s and λ_s are a tridimensional vector and a 3×3 matrix in flavor space respectively. This class of scenarios is the one that has been adopted by the ATLAS collaboration for its Run I monotop searches [?] and will be considered by both collaborations for Run II analyses.

The resulting model can be likened to the MSSM with an R-parity violating of a top squark to the Standard Model down-type quarks and an R-parity conserving interaction of a top quark and a top-squark to a neutralino.

NON-RESONANT PRODUCTION

For non-resonant monotop production, the monotop state is produced via flavor-changing neutral interactions of the top quark, a lighter up-type quark and a new invisible vector particle V. This is the only case considered, as having a new scalar would involve

in particular a mixing with the SM Higgs boson and therefore a larger number of free parameters. The Lagrangian describing the dynamics of this non-resonant monotop production case is:

$$\mathcal{L} = \left[V_\mu \bar{u} \gamma^\mu \left[a_{FC}^1 + b_{FC}^1 \gamma_5 \right] u + \text{h.c.} \right] \qquad \text{(B.3)}$$

where the flavor and color indices are again understood for clarity.

The strength of the interactions among these two states and a pair of up-type quarks is modeled via two 3×3 matrices in flavor space a_{FC}^1 for the vector couplings and b_{FC}^1 for the axial vector couplings.

As for the resonant case, the Lagrangian of Eq. (B.3) is the one that has been used by CMS after reintroducing the scalar option for the invisible state and neglecting all pseudoscalar interactions [**?**]. As already mentioned, a simplified setup motivated by gauge invariance and minimality has been preferred so that, as shown in Ref. [BCDF15], we impose all interactions to involve right-handed quarks only in order to simplify the model phenomenology,

$$a_{FC}^1 = b_{FC}^1 = \frac{1}{2} a_R \qquad \text{(B.4)}$$

where a_R denotes a 3×3 matrix in flavor space. This implies the vector field to be an $SU(2)_L$ singlet.

Model parameters and assumptions

The models considered as benchmarks for the first LHC searches contain further assumptions in terms of the flavor structure of the model with respect to the Lagrangians of the previous subsection.

In order to have an observable monotop signature at the LHC, the Lagrangians introduced above must include not too small couplings of the new particles to first and second generation quarks. For simplicity, we assumed that only channels enhanced by parton density effects will be considered, so that we fix

$$\begin{aligned} (a_R)_{13} = (a_R)_{31} = a \ , \\ (\lambda_s)_{12} = -(\lambda_s)_{21} = \lambda \qquad \text{and} \qquad (y_s)_3 = y \ , \end{aligned} \qquad \text{(B.5)}$$

all other elements of the matrices and vectors above being set to zero.

Implementation

The Monte Carlo simulation relevant for this case is discussed in Appendix A.

B.1.1   Parameter scan

Under all the assumptions of the previous sections, the parameter space of the resonant model is defined by four quantities, namely the mass of the new scalar field φ, the mass of the invisible fermion χ and the strengths of the interactions of the scalar resonance with the monotop system y and with down-type quarks λ. One of both

To do **There is still an on-going study that should be finished very soon (by the end of the week). The point is that CMS is fixing the y parameters in the way that the branching ratio of the scalar resonance into a monotop system is close to 100%, while ATLAS is fixing y = lambda. We are investigating both cases so to conclude whether this is good to keep both options allowed. (??)**

coupling parameters could however be traded with the width of the resonance.

The parameter space of the non-resonant model is defined by two parameters, namely the mass of the invisible state V and its flavour-changing neutral coupling to the up-type quarks a_R.

In the case of the non-resonant model, the invisible vector is connected to a hidden sector that could be, in its simplest form, parameterized by a new fermion [BCDF15]. This has effects on the width of the invisible V state.

A consensus between the ATLAS and CMS collaborations has been reached in the case of non-resonant monotop production. The results have been described above. In contrast, discussions in the context of resonant monotop production are still on-going. The related parameter space contains four parameters and must thus be further simplified for practical purposes. Several options are possible and a choice necessitates additional studies that will be achieved in a near future.

It has been verified that the kinematics do not depend on the width of the invisible state in the case where this width is at most 10% of the V-mass. This is illustrated in Figures B.2 and B.3, where we respectively show the invariant-mass and transverse-momentum spectra of the V-boson when it decays into a top-up final state and for different V-boson masses. The results are however independent of the visible or invisible decay modes as we are only concerned with the kinematical properties of the invisible state.
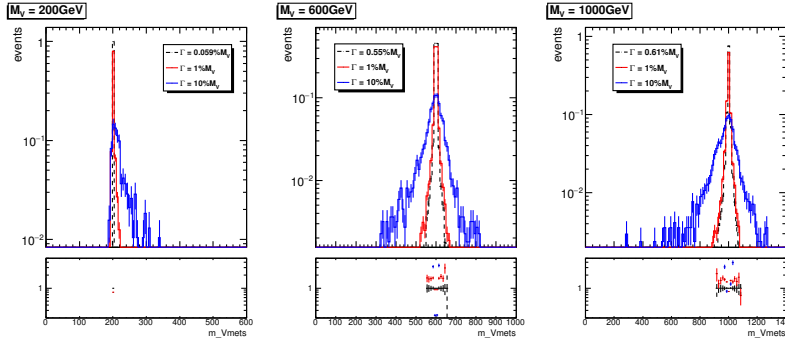
To do **Pictures will be improved in the next drafts. (??)**

Figure B.2: Distributions of the invariant mass of the V boson in the case of the process $pp \rightarrow tV \rightarrow t(t\bar{u} + \text{c.c.})$. We have imposed that the V-boson is produced on-shell and have chosen its mass to be $m_V = 200$, 600 and 1000 GeV (left, central and right panels). Moreover, we have considered three possible cases for the total width of the V-boson, which has been fixed to 0.61%, 0.1% and 10% of the mass.
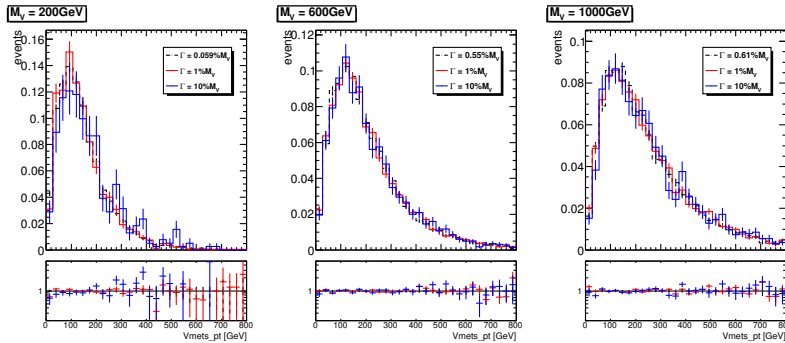

Figure B.3: Same as Figure B.2 in the case of the transverse-momentum distribution of the V-boson.

B.1.2 Single Top Models

Card files for MADGRAPH5_AMC@NLO are provided on the Forum SVN repository [For15e], corresponding to the Lagrangian from [AFM11]. Each coupling constant of this model can be set via the parameter card and the blocks which are relevant for the two models used for the experimental searches are described below. The relevant parameters in the MADGRAPH5_AMC@NLO parameter cards, also expressed in the notation introduced in the previous Section, are as follows for the two models considered.

1. Resonant scalar model described by the Lagrangian (B.1)

   - AQS and BQS: 3×3 matrices (flavour space) fixing the coupling of the scalar ϕ (S stands for scalar) and *down*-type quarks (Q stands for quarks), previously called a^q / b^q_{SR}.

   - A12S and B12S: 3×1 matrices (flavor space) fixing the coupling of the new fermion χ (where 12 stands for spin-1/2 fermion) and *up*-type quarks, previously called $a^{1/2}_{VR}$.

2. Non-resonant vectorial model described by the Lagrangian (B.3)

   - A1FC and B1FC: 3×3 matrices (flavor space) fixing the coupling of the vector V (1 stands for vector) and *up*-type quarks, previously called a^1_{FC}.

   - particle name: the dark matter candidate χ is not implemented

The width of the scalar resonance and of the new vector are set to all allowed decays in the ATLAS implementation, while the only allowed decay in the CMS implementation to the new fermion and a top quark for the resonant model.

B.2 Further W+$\not{E}_T$ models with possible cross-section enhancements

As pointed out in Ref. [BCD$^+$15], the mono-*W* signature can probe the iso-spin violating interactions of dark matter with quarks. The relevant operator after the electroweak symmetry breaking is

$$\frac{1}{\Lambda^2} \overline{\chi} \gamma_\mu \chi \left(\overline{u}_L \gamma^\mu u_L + \xi \overline{d}_L \gamma^\mu d_L \right) . \qquad (B.6)$$

Here, we only keep the left-handed quarks because the right-handed quarks do not radiate a *W*-gauge boson from the weak interaction. As the LHC constrains the cutoff to higher values, it is also important to know the corresponding operators before the electroweak symmetry. At the dimension-six level, the following operator

$$\frac{c_6}{\Lambda^2} \overline{\chi} \gamma_\mu \chi \, \overline{Q}_L \gamma^\mu Q_L \qquad (B.7)$$

To do **This section is being reworked by B. Fuks (??)**

To do **Continue discussion between ATLAS and CMS to reach an agreement, or include instructions to compare results. (??)**

conserves iso-spin and provides us $\xi = 1$ [BCD$^+$15]. At the dimension-eight level, new operators appear to induce iso-spin violation and can be

$$\frac{c_8^d}{\Lambda^4}\overline{\chi}\gamma_\mu\chi\,(H\overline{Q}_L)\gamma^\mu(Q_L H^\dagger) + \frac{c_8^u}{\Lambda^4}\overline{\chi}\gamma_\mu\chi\,(\tilde{H}\overline{Q}_L)\gamma^\mu(Q_L \tilde{H}^\dagger)\,. \qquad \text{(B.8)}$$

After inputting the vacuum expectation value of the Higgs field, we have

$$\xi = \frac{c_6 + c_8^d\, v_{\text{EW}}^2/2\Lambda^2}{c_6 + c_8^u\, v_{\text{EW}}^2/2\Lambda^2}\,. \qquad \text{(B.9)}$$

For a nonzero c_6 and $v_{\text{EW}} \ll \Lambda$, the iso-spin violation effects are suppressed. On the other hand, the values of c_6, c_8^d and c_8^u depend on the UV-models.

There is one possible UV-model to obtain a zero value for c_6 and non-zero values for c_8^d and c_8^u. One can have the dark matter and the SM Higgs field charged under a new $U(1)'$ symmetry. There is a small mass mixing between SM Z-boson and the new Z' with a mixing angle of $\mathcal{O}(v_{\text{EW}}^2/M_{Z'}^2)$. After integrating out Z', one has different effective dark matter couplings to u_L and d_L fields, which are proportional to their couplings to the Z boson. For this model, we have $c_6 = 0$ and

$$\xi = \frac{-\frac{1}{2} + \frac{1}{3}\sin^2\theta_W}{\frac{1}{2} - \frac{2}{3}\sin^2\theta_W} \approx -2.7 \qquad \text{(B.10)}$$

and order of unity.

B.3 Simplified model corresponding to dimension-5 EFT operator

As an example of a simplified model corresponding to the dimension-5 EFT operator described in Section 3.2, we consider a Higgs portal with a scalar mediator. Models of this kind are among the most concise versions of simplified models that produce couplings of Dark Matter to pairs of gauge-bosons. Scalar fields may couple directly to pairs of electroweak gauge bosons, but must carry part of the electroweak vacuum expectation value. One may thus consider a simple model where Dark Matter couples to a a scalar singlet mediator, which mixes with the fields in the Higgs sector.

$$L \subset m_s S^2 + \lambda S^2 H^2 + \lambda' S H^2 + y S \chi \overline{\chi} \qquad \text{(B.11)}$$

Where H is a field in the Higgs sector that contains part of the electroweak vacuum expectation value, S is a heavy scalar singlet and χ is a Dark Matter field. There is then an s-channel diagram where DM pairs couple to the singlet field S, which then mixes with a Higgs-sector field, and couples to W and Z bosons. This diagram contains 2 insertions of EW symmetry breaking fields, corresponding in form to the effective dimension-5 operator in Section 3.2.1.

B.4   Inert 2HDM Model

For most of the simplified models included in this report, the mass of the mediator and couplings/width are non-trivial parameters of the model. In these scenarios, we remain agnostic about the theory behind the dark matter sector and try to parameterize it in simple terms.

We have not addressed how to extend the simplified models to realistic and viable models which are consistent with the symmetries of the Standard Model. Simplified models often violate gauge invariance which is a crucial principle for building a consistent BSM model which incorporates SM together with new physics. For example, with a new heavy gauge vector boson mediating DM interactions, one needs not just the dark matter and its mediator, but also a mechanism which provides mass to this mediator in a gauge invariant way.

Considering both the simplified model and other elements necessary for a consistent theory is a next logical step. The authors of [BCI+] term these Minimal Consistent Dark Matter (MCDM) models. MCDM models are at the same time still toy models that can be easily incorporated into a bigger BSM model and explored via complementary constraints from collider and direct/indirect DM search experiments as well as relic density constraints. We discuss this model here both on its own merits and as an example of the flexibility of the simplified model approach.

The idea of an inert Two-Higgs Doublet Model (i2HDM) was introduced more than 30 years ago in [DM78, LHNOT07, DS09, GHS13, BCI+]. It is an extension of the SM with a second scalar doublet ϕ_2 with no direct coupling to fermions. This doublet has a discrete Z_2 symmetry, under which ϕ_2 is odd and all the other fields are even. The Lagrangian of the odd sector is,

$$\mathcal{L} = \frac{1}{2}(D_\mu \phi_2)^2 - V(\phi_1, \phi_2) \tag{B.12}$$

with the potential V containing mass terms and $\phi_1 - \phi_2$ interactions:

$$
\begin{aligned}
V & = & -m_1^2(\phi_1^\dagger \phi_1) - m_2^2(\phi_2^\dagger \phi_2) + \lambda_1(\phi_1^\dagger \phi_1)^2 + \lambda_2(\phi_2^\dagger \phi_2)^2 \\
& + & \lambda_3(\phi_2^\dagger \phi_2)(\phi_1^\dagger \phi_1) + \lambda_4(\phi_2^\dagger \phi_1)(\phi_1^\dagger \phi_2) + \frac{\lambda_5}{2}\left[(\phi_1^\dagger \phi_2)^2 + (\phi_2^\dagger \phi_1)^2\right],
\end{aligned}
\tag{B.13}
$$

where ϕ_1 and ϕ_2 are SM and inert Higgs doublets respectively carrying the same hypercharge. These doublets can be parameterized as

$$\phi_1 = \frac{1}{\sqrt{2}}\begin{pmatrix} 0 \\ v+H \end{pmatrix} \qquad \phi_2 = \frac{1}{\sqrt{2}}\begin{pmatrix} \sqrt{2}h^+ \\ h_1 + ih_2 \end{pmatrix} \tag{B.14}$$

In addition to the SM, i2HDM brings four more degrees of freedom coming from the inert doublet in the form of Z_2-odd charged scalar $h^\pm$ and two neutral Z_2-odd scalars h_1 and h_2. The lightest

neutral scalar, h_1 is identified as the dark matter candidate. The
i2HDM model has been explored at the phenomenological level
from the perspective of collider DM searches [BPtV01, AHT08,
ATYY14, BCI$^+$]. This model could produce $\not{E}_T$ +jet, Z, and Higgs as
well as $\not{E}_T$ +VBF signatures at the LHC (see Figs. B.4–B.9).
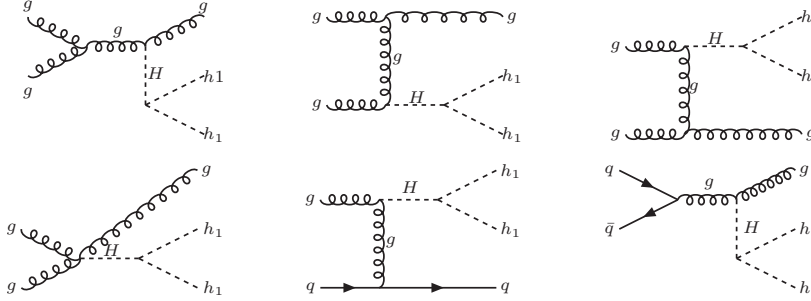
Figure B.4: Feynman diagrams for $gg \to h_1 h_1 + g$ process contributing to mono-jet signature, adapted from [BCI$^+$].
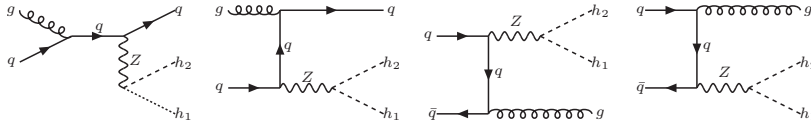
Figure B.5: Feynman diagrams for $q\bar{q} \to h_1 h_2 + g$ ($gq \to h_1 h_2 + q$) process contributing to mono-jet signature, adapted from [BCI$^+$].

Figure B.6: Feynman diagrams for $q\bar{q} \to h_1 h_1 + Z$ process contributing to mono-Z signature, adapted from [BCI$^+$].

An experimental analysis of the parameter space has recently
been performed in Ref. [BCI$^+$]. The authors of that study have im-
plemented the model in CalcHEP and micrOMEGAs and propose a
set of benchmark points (Table. B.1). Though the overall parameter
space of i2HDM is 5-dimensional, the parameter space relevant to
a specific LHC signature is only 1-2 dimensional. In the mono-jet
case, one can use two separate simplified models, a $gg \to h_1 h_1 + g$
process (via Higgs mediator) and a $q\bar{q} \to h_1 h_2 + g$ ($gq \to h_1 h_2 + q$)
process (using Z-boson mediator) to capture the physics relevant to
the search.
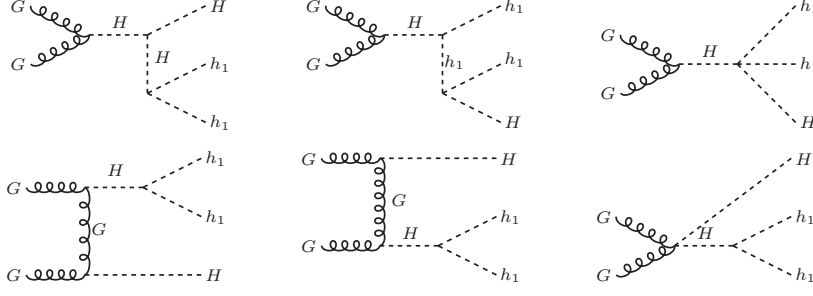
Figure B.7: Feynman diagrams for $gg \to h_1 h_1 + H$ process contributing to mono-Higgs signature, adapted from [BCI$^+$].

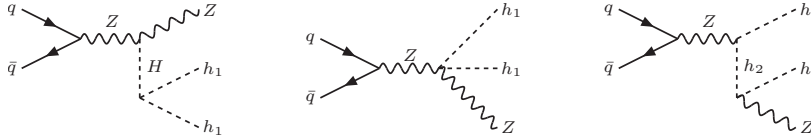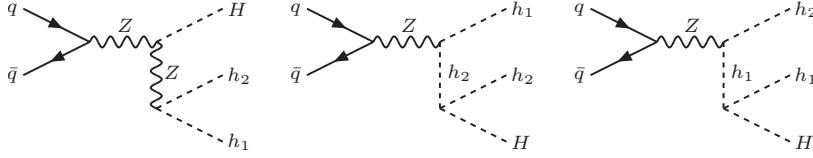Figure B.8: Feynman diagrams for $q\bar{q} \to h_1 h_2 + H$ process contributing to mono-Higgs signature, adapted from [BCI$^+$].
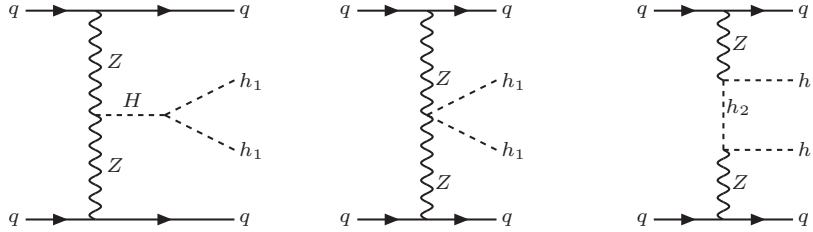
Figure B.9: Diagrams for $qq \to qq h_1 h_1$ DM production in vector boson fusion process, adapted from [BCI$^+$].

Benchmark	1	2	3	4	5
M_{h_1} (GeV)	45	53	66	82	120
M_{h_2} (GeV)	55	189	77	89	140
$M_{h_\pm}$ (GeV)	130	182	122	150	200
λ_2	0.8	1.0	1.1	0.9	1.0
λ_{345}	-0.010	-0.024	$+0.022$	-0.090	-0.100
Ω_h^2	1.1×10^{-1}	8.1×10^{-2}	9.9×10^{-2}	1.5×10^{-2}	2.1×10^{-3}
σ_{SI} (fb)	1.9×10^{-7}	7.9×10^{-7}	4.2×10^{-7}	4.5×10^{-7}	2.6×10^{-6}
σ_{LHC} (fb)	1.7×10^2	7.7×10^2	4.3×10^{-2}	1.2×10^{-1}	2.3×10^{-2}

Table B.1: Five benchmarks for i2HDM in $(M_{h_1}, M_{h_2}, M_{h_\pm}, \lambda_2, \lambda_{345})$ parameter space. We also present the corresponding relic density (Ω_{h^2}), the spin-independent cross section for DM scattering on the proton, and the LHC cross section at 13 TeV for mono-jet process $pp \to h_1, h_1 + jet$ for $p_T^{jet} > 100$ GeV cut.

C

Appendix: Presentation of experimental results for reinterpretation

We suggest the following to collider searches, when presenting results from the recommended benchmarks:

- Provide limits in collider language, on fundamental parameters of interaction: couplings and masses of particles in simplified model.

- Translate limits to non-collider language, for a range of assumptions in order to convey a rough idea of the range of possibilities. The details of this point are left for work beyond the scope of this Forum.

- Provide all necessary material for theorists to reinterpret simplified model results as building blocks for more complete models (e.g. signal cutflows, acceptances, etc). This point is detailed further in this appendix.

- As detailed in [KAM+12], model-independent results in terms of limits on cross-section times acceptance of new phenomena should be provided for all cases, but especially when EFTs are employed as benchmarks.

  Along with the design of new searches to hunt for new physics at the LHC, it is important to consider information needed in order to reinterpret the searches outside of the collaborations. The following is a non-exhaustive list of recommendations in order to make reinterpretation easier and faster. This appendix details considerations for reimplementation of the analysis as well as for using the simplified model results directly given by the collaborations.
  One of the important developments in recent years is an active development of the analyses recasting codes [DFK+15, CDFW14, KSTR15, CY11, KPSW]. The aim of these codes is to provide a public library of reimplemented and validated LHC analyses. Such libraries can then be used to analyze validity of a BSM scenario in a systematic and effective manner. The availability of public libraries further facilitates a unified framework and can lead to an organized and central structure to preserve LHC information in a long run.

In order to be able to develop such codes, it is important to get complete and systematic information from the collaborations.

- **Data digitization**: Availability of digitized data is one of the primary requirement. All information given by collaborations in the form of plots should be made available in a digitized format. Platforms such as HepData can be used in oder to maintain a centralized manner. In case when HepData can not be used, digitized data can be provided via analyses twiki pages. This information primarily includes expected and observed exclusion lines along with their $\pm 1\sigma$ uncertainty, expected and observed upper limits in case of simplified models, efficiency maps and all kinematic distributions as reported in the analysis. Units should be clearly specified. If the digitized figures are made available as a C macro or a ROOT file, the names of the objects should be clearly identifiable e.g. expected upper limits of a particular topology/model given as a ROOT file can be labeled as KEY: TH2D ExpectedUpperLimit;1. Furthermore, these digitized files can potentially contain more information (larger axes ranges) than displayed on the plot. This will help facilitate understand what happens beyond the limits displayed in the plot, e.g. a distribution for number of jets can be artificially limited to a point in the plot (for the purpose of clarity of figure) , however, this artificial limit leads to a sharp cutoff in the plot. While validating the analysis it is often necessary to compare the distributions beyond such artificial limits, having this information digitized will be of a great help in such cases.

C.1   Reimplementing analyses

This section lists information necessary in order to reimplement an analysis. Analysis reimplementation usually consists of several stages. Usually, one starts with reading the analysis note carefully, following which the preselection and event selection cuts are identified. These are then mimicked using a code typically written in C++. The detector simulation is carried out by using public detector simulation software e.g. Delphes [dF$^+$14]. The resulting ROOT file is then analyzed using the C++ code written in the previous step.

- **Analysis documentation**: The collaborations should provide a cutflow table with every analysis, such a cutflow table will naturally define the order of cuts implemented in an analysis. There are several preselection criteria which can not be easily simulated in phenomenology, e.g. MET cleaning. Numbers should be provided after such cuts so that theorists can rescale their number of events in order to account for such cuts. Efficiencies of several reconstructed objects are given as an input to detector simulation software like Delphes. It is thus very useful to get parametrized efficiencies for reconstructed objects (as a function of the rapidity η and/or transverse momentum p_T), along with the working

points at which they were evaluated (e.g. loose, tight selection). Object definitions should be clearly identifiable.

- **Validation**: Validation corresponds to re-deriving the results as given by collaborations in order to verify that the implementation of the analysis is correct. Usually most of the bug catching takes place in the phase of validation. The following items are necessary in order to recreate the results.

  - Monte Carlo generators: Monte Carlo generators along with the exact versions used to produce the event files should be listed.

  - Production cross sections: The order of production cross sections (e.g. LO,NLO,NLL) as well as the codes which were used to compute them should be provided. A table of reference cross sections for several values of particle masses such as ones provided by SUSY cross section working group will be highly appreciated.

  - Process Generation: Details of the generated process, detailing number of additional partons generated.

  - Availability of the LHE files: selected LHE files (detailing at least a few events if not the entire file) corresponding to the benchmarks listed in the analysis should be made available in order to cross check process generation. Experimental collaborations may generate events on-the-fly without saving the intermediate LHE file; we advocate that the cross-check of process generation is straight-forward if this information is present, so we encourage the generation of a few selected benchmark points allowing for a LHE file to be saved. For models concerning SUSY, corresponding SLHA files of benchmark files should also be details. Special attention should be paid to list the parameters which change the production cross section or kinematics of the process e.g. mixing angles.

  - Process cards: Process cards includes PDF choices, details of matching algorithms and scales and details of process generation. If process cards are not available, above items should be clearly identified.

  - model files: For models which are not already implemented in MADGRAPH5_AMC@NLO, availability of the corresponding model files in UFO format [DDF$^+$12] is highly desired. It details the exact notation used in the model and hence sets up a complete framework. In case MADGRAPH5_AMC@NLO is not used, enough information should be provided in order to clearly identify the underlying model used for interpretations.

- **Limit setting**: Detailed description of the likelihood used in order to derive the limits should be given, this can contain statistical procedure within the analysis text itself, however direct availability of the limit setting code as a workspace in RooStats or HistFitter [BBC$^+$15] is highly desirable.

- **Binned backgrounds**: For analyses using techniques such as sliding windows or an unbinned technique, the Standard Model backgrounds should be given in the form of bins. These backgrounds can then be interpolated.

- **Recast code**: Finally, the collaborations can provide an analysis code directly implemented in one of the public recasting codes detailed above. Such codes can be published via INSPIRE in order to track the versioning and citations.

C.2   *Simplified model interpretations*

The analyses almost always provide at least one simplified model interpretation along with the search results. These interpretations are simple and can be used in order to take a quick survey of viability of parameter space. Codes such as [KKL$^+$14b, KKL$^+$14a, PSWZ14] can make use of the simplified model results given in the form of 95% Confidence Level (CLs) upper limit or efficiency maps in order to test Beyond the Standard Model parameter space. It will thus be extremely useful if the results are given in a form as easily usable by the theory community.

- **Direct usability of the results**: The results given should be as useful as possible. For example, for a simplified model containing dark matter mass m_{DM}, mediator mass M_{med} and couplings g_{DM}, g_{q} it will be extremely useful to have 95% CLs upper limits on the product of couplings $\sqrt{g_{\mathrm{DM}} g_{\mathrm{q}}}$ or cross section times branching ratio as a function of m_{DM}, M_{med}. Limits on visible cross sections of the simplified models considered for interpretations should be made available.

- **Smooth grids**: The usage of simplified model results relies on interpolating between upper limit values. In order to facilitate the interpolation, regions where large variation of upper limits is observed should contain denser grid, if a uniform grid over the entire plane is not possible. For simplified model involving more than three parameters (two masses and product of couplings), slices of upper limits in the additional dimensions will be very useful e.g. for a simplified model involving one step cascade decay, upper limits can be provided for several values of intermediate mass in the plane of mother - daughter masses. Results with only one slice often render invalid to be used in a general model testing.

- **Availability of acceptance and efficiency maps**: Finally, acceptance and efficiency maps for all the signal regions involved in the analysis should be made available. These results are not only useful for model testing using simplified models but also to validate implementation of the analysis. Information about the most sensitive signal region as a function of masses is also very useful in order to determine the validity of approximate limit setting

2641 procedures being used by theorists (in the absence of any other
2642 sophisticated limit setting technique).

D

Appendix: Additional details and studies within the Forum

D.1 Further information for baryonic Z' Model

D.1.1 Cross-section scaling

The dependence of the cross section of the $pp \rightarrow H\chi\bar{\chi} + X$ process on $g_{hZ'Z'}$ is shown in Figure D.1. The curves have been fit to second-order polynomials, where y is the cross-section and x is the coupling $g_{hZ'Z'}$.

For $m_{med} = 100$ GeV, the fit function is

$$y = -0.12 - 3.4 \times 10^{-3}x + 2.7 \times 10^{-4}x^2$$

. For $m_{med} = 1$ TeV, the fit function is is

$$y = 0.0012 - 2.4 \times 10^{-7}x + 1.5 \times 10^{-7}x^2$$

,

$$y = -0.12 - 3.4 \times 10^{-3}x + 2.7 \times 10^{-4}x^2. \tag{D.1}$$

For $M_{med} = 1$ TeV, the fit function is is:

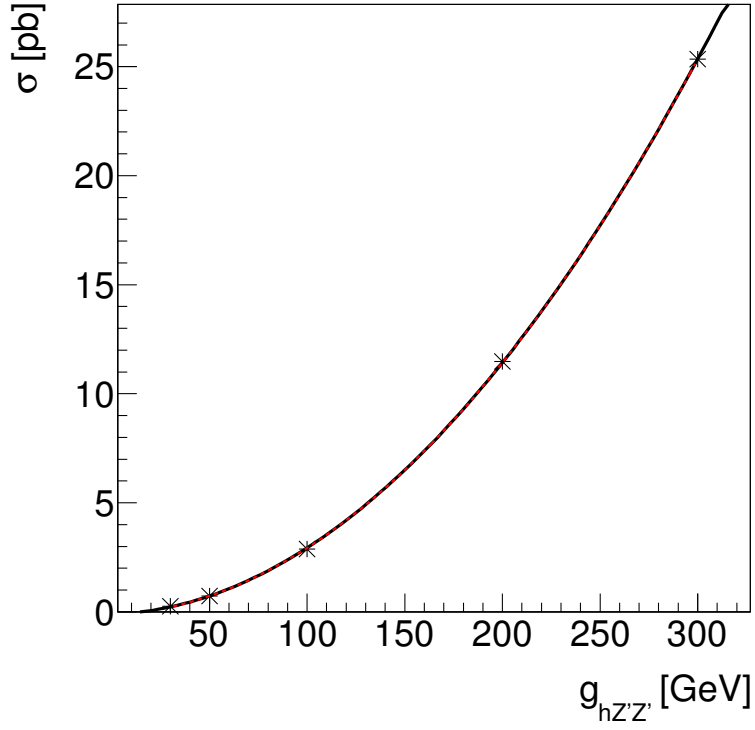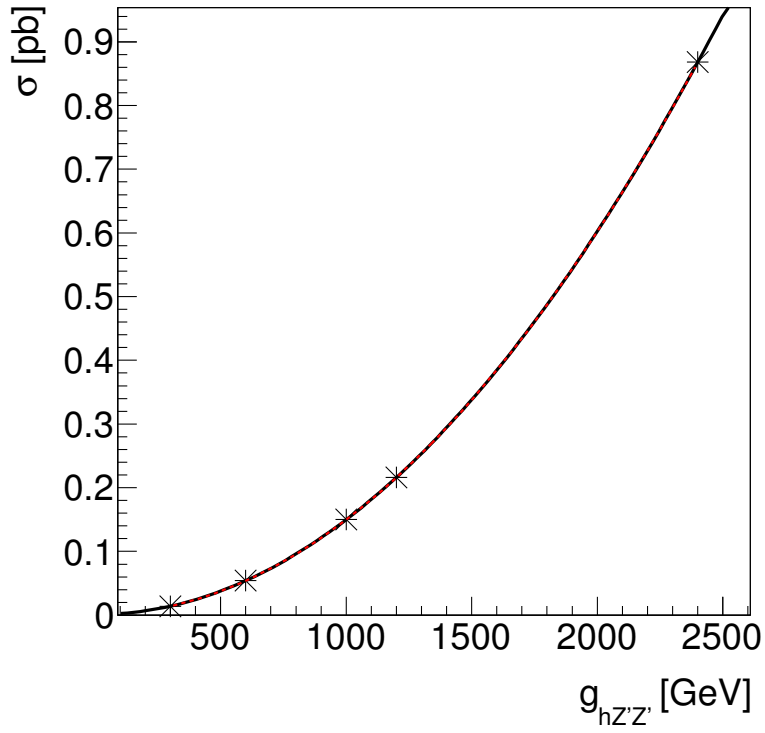$$y = 0.0012 - 2.4 \times 10^{-7}x + 1.5 \times 10^{-7}x^2. \tag{D.2}$$

Figure D.1: Cross section of the $pp \rightarrow$ $H\chi\bar{\chi}$ process as a function of $g_{hZ'Z'}$ for $m_{Z'} = 100$ GeV (left) and $m_{Z'} = 1$ TeV (right). The fit functions are shown in the text.

Bibliography

[A+08] J. Alwall et al. Comparative study of various algorithms for the merging of parton showers and matrix elements in hadronic collisions. *Eur.Phys.J.*, C53(2):473–500, 2008.

[A+12a] T. Aaltonen et al. A Search for dark matter in events with one jet and missing transverse energy in $p\bar{p}$ collisions at $\sqrt{s} = 1.96$ TeV. *Phys.Rev.Lett.*, 108:211804, 2012.

[A+12b] Daniele Alves et al. Simplified Models for LHC New Physics Searches. *J.Phys.*, G39:105005, 2012.

[A+14a] Jalal Abdallah et al. Simplified Models for Dark Matter and Missing Energy Searches at the LHC. *arXiv:1409.2893*, 2014.

[A+14b] J. Alwall et al. The automated computation of tree-level and next-to-leading order differential cross sections, and their matching to parton shower simulations. *JHEP*, 07(2):079, 2014.

[AAB+14] Jean-Laurent Agram, Jeremy Andrea, Michael Buttignol, Eric Conte, and Benjamin Fuks. Monotop phenomenology at the Large Hadron Collider. *Phys.Rev.*, D89(1):014028, 2014.

[ABG14] Prateek Agrawal, Monika Blanke, and Katrin Gemmler. Flavored dark matter beyond Minimal Flavor Violation. *JHEP*, 1410:72, 2014.

[ABHL14] Prateek Agrawal, Brian Batell, Dan Hooper, and Tongyan Lin. Flavored Dark Matter and the Galactic Center Gamma-Ray Excess. *Phys.Rev.*, D90(6):063512, 2014.

[ACD+14] Adam Alloul, Neil D. Christensen, Celine Degrande, Claude Duhr, and Benjamin Fuks. Feynrules 2.0 - a complete toolbox for tree-level phenomenology. *Comput.Phys.Commun.*, 185:2250–2300, 2014.

[ADNP15] Chiara Arina, Eugenio Del Nobile, and Paolo Panci. Dark Matter with Pseudoscalar-Mediated Interactions Explains the DAMA Signal and the Galactic Center Excess. *Phys.Rev.Lett.*, 114:011301, 2015.

[AFF⁺14]   J. Alwall, R. Frederix, S. Frixione, V. Hirschi, F. Maltoni, et al. The automated computation of tree-level and next-to-leading order differential cross sections, and their matching to parton shower simulations. *JHEP*, 1407:079, 2014.

[AFM11]   J. Andrea, B. Fuks, and F. Maltoni. Monotops at the LHC. *Phys.Rev.*, D84:074025, 2011.

[AHM⁺11]   Johan Alwall, Michel Herquet, Fabio Maltoni, Olivier Mattelaer, and Tim Stelzer. MadGraph 5 : Going Beyond. *JHEP*, 1106:128, 2011.

[AHT08]   Sarah Andreas, Thomas Hambye, and Michel H.G. Tytgat. WIMP dark matter, Higgs exchange and DAMA. *JCAP*, 0810:034, 2008.

[AHW13]   Haipeng An, Ran Huo, and Lian-Tao Wang. Searching for Low Mass Dark Portal at the LHC. *Phys.Dark Univ.*, 2:50–57, 2013.

[AJW12]   Haipeng An, Xiangdong Ji, and Lian-Tao Wang. Light Dark Matter and Z' Dark Force at Colliders. *JHEP*, 1207:182, 2012.

[ANOR10]   Simone Alioli, Paolo Nason, Carlo Oleari, and Emanuele Re. A general framework for implementing NLO calculations in shower Monte Carlo programs: the POWHEG BOX. *JHEP*, 1006:043, 2010.

[AST09]   Johan Alwall, Philip Schuster, and Natalia Toro. Simplified Models for a First Characterization of New Physics at the LHC. *Phys.Rev.*, D79:075020, 2009.

[ATL14a]   ATLAS Collaboration. Search for dark matter in events with a hadronically decaying W or Z boson and missing transverse momentum in pp collisions at $\sqrt{s} = 8$ TeV with the ATLAS detector. *Phys.Rev.Lett.*, 112(4):041802, 2014.

[ATL14b]   ATLAS Collaboration. Search for dark matter in events with a Z boson and missing transverse momentum in pp collisions at $\sqrt{s}=8$ TeV with the ATLAS detector. *Phys.Rev.*, D90(1):012004, 2014.

[ATL14c]   ATLAS Collaboration. Search for new particles in events with one lepton and missing transverse momentum in pp collisions at $\sqrt{s} = 8$ TeV with the ATLAS detector. *JHEP*, 1409:037, 2014.

[ATL14d]   ATLAS Collaboration. Sensitivity to WIMP Dark Matter in the Final States Containing Jets and Missing Transverse Momentum with the ATLAS Detector at 14 TeV LHC. (ATL-PHYS-PUB-2014-007), Jun 2014.

[ATL15a] ATLAS Collaboration. Search for dark matter in events with heavy quarks and missing transverse momentum in pp collisions with the ATLAS detector. *Eur.Phys.J.*, C75(2):92, 2015.

[ATL15b] ATLAS Collaboration. Search for invisible particles produced in association with single-top-quarks in proton-proton collisions at $\sqrt{s}$ = 8 TeV with the ATLAS detector. *Eur.Phys.J.*, C75(2):79, 2015.

[ATL15c] ATLAS Collaboration. Search for new phenomena in events with a photon and missing transverse momentum in pp collisions at $\sqrt{s} = 8$ TeV with the ATLAS detector. *Phys.Rev.*, D91(1):012008, 2015.

[ATL15d] ATLAS Collaboration. Search for new phenomena in final states with an energetic jet and large missing transverse momentum in pp collisions at $\sqrt{s} = 8$ TeV with the ATLAS detector. *arXiv:1502.01518 [hep-ex], Submitted to Eur.Phys.J. C*, 2015.

[ATYY14] Abdesslam Arhrib, Yue-Lin Sming Tsai, Qiang Yuan, and Tzu-Chiang Yuan. An Updated Analysis of Inert Higgs Doublet Model in light of the Recent Results from LUX, PLANCK, AMS-02 and LHC. *JCAP*, 1406:030, 2014.

[AWZ14] Haipeng An, Lian-Tao Wang, and Hao Zhang. Dark matter with t-channel mediator: a simple step beyond contact interaction. *Phys.Rev.*, D89(11):115014, 2014.

[BB13] Yang Bai and Joshua Berger. Fermion Portal Dark Matter. *JHEP*, 1311:171, 2013.

[BB14] Yang Bai and Joshua Berger. Lepton Portal Dark Matter. *JHEP*, 1408:153, 2014.

[BBB+89] Dmitri Yu. Bardin, Mikhail S. Bilenky, W. Beenakker, Frits A. Berends, W.L. van Neerven, et al. Z LINE SHAPE. 1989.

[BBC+15] M. Baak, G.J. Besjes, D. CÃ´te, A. Koutsman, J. Lorenz, et al. HistFitter software framework for statistical data analysis. *Eur.Phys.J.*, C75(4):153, 2015.

[BCD+15] Nicole F. Bell, Yi Cai, James B. Dent, Rebecca K. Leane, and Thomas J. Weiler. Dark matter at the LHC: EFTs and gauge invariance. 2015.

[BCDF15] Idir Boucheneb, Giacomo Cacciapaglia, Aldo Deandrea, and Benjamin Fuks. Revisiting monotop production at the LHC. *JHEP*, 1501:017, 2015.

[BCI+] A. Belyaev, G. Cacciapaglia, I. Ivanov, F. Rojas, and M. Thomas. page to appear.

[BDG+12]   Nicole F. Bell, James B. Dent, Ahmad J. Galea, Thomas D. Jacques, Lawrence M. Krauss, et al. Searching for Dark Matter at the LHC with a Mono-Z. *Phys.Rev.*, D86:096011, 2012.

[BDM14]   O. Buchmueller, Matthew J. Dolan, and Christopher McCabe. Beyond Effective Field Theory for Dark Matter Searches at the LHC. *JHEP*, 1401:025, 2014.

[BDMM15]   Oliver Buchmueller, Matthew J. Dolan, Sarah A. Malik, and Christopher McCabe. Characterising dark matter searches at colliders and direct detection experiments: Vector mediators. *JHEP*, 1501:037, 2015.

[BDSG+14]   Giorgio Busoni, Andrea De Simone, Johanna Gramling, Enrico Morgante, and Antonio Riotto. On the Validity of the Effective Field Theory for Dark Matter Searches at the LHC, Part II: Complete Analysis for the s-channel. *JCAP*, 1406:060, 2014.

[BDSJ+14]   Giorgio Busoni, Andrea De Simone, Thomas Jacques, Enrico Morgante, and Antonio Riotto. On the Validity of the Effective Field Theory for Dark Matter Searches at the LHC Part III: Analysis for the t-channel. *JCAP*, 1409:022, 2014.

[BDSMR14]   Giorgio Busoni, Andrea De Simone, Enrico Morgante, and Antonio Riotto. On the Validity of the Effective Field Theory for Dark Matter Searches at the LHC. *Phys.Lett.*, B728:412–421, 2014.

[BFG15]   Matthew R. Buckley, David Feld, and Dorival Goncalves. Scalar Simplified Models for Dark Matter. *Phys.Rev.*, D91(1):015017, 2015.

[BFH10]   Yang Bai, Patrick J. Fox, and Roni Harnik. The Tevatron at the Frontier of Dark Matter Direct Detection. *JHEP*, 1012:048, 2010.

[BFT10]   Tom Banks, Jean-Francois Fortin, and Scott Thomas. Direct Detection of Dark Matter Electromagnetic Dipole Moments. 2010.

[BGG+01]   A.J. Buras, P. Gambino, M. Gorbahn, S. Jager, and L. Silvestrini. Universal unitarity triangle and physics beyond the standard model. *Phys.Lett.*, B500:161–167, 2001.

[BHK+10]   Maria Beltran, Dan Hooper, Edward W. Kolb, Zosia A.C. Krusberg, and Tim M.P. Tait. Maverick dark matter at colliders. *JHEP*, 1009:037, 2010.

[BLW14]   Asher Berlin, Tongyan Lin, and Lian-Tao Wang. Mono-Higgs Detection of Dark Matter at the LHC. *JHEP*, 1406:078, 2014.

[BPtV01] C.P. Burgess, Maxim Pospelov, and Tonnis ter Veldhuis. The Minimal model of nonbaryonic dark matter: A Singlet scalar. *Nucl.Phys.*, B619:709–728, 2001.

[BT13] Yang Bai and Tim M.P. Tait. Searches with Mono-Leptons. *Phys.Lett.*, B723:384–387, 2013.

[C⁺13] Serguei Chatrchyan et al. Measurement of the cross section and angular correlations for associated production of a Z boson with b hadrons in pp collisions at $\sqrt{s} = 7$ TeV. *JHEP*, 1312:039, 2013.

[C⁺14] Serguei Chatrchyan et al. Measurement of the production cross sections for a Z boson and one or more b jets in pp collisions at sqrt(s) = 7 TeV. *JHEP*, 1406:120, 2014.

[CCW15] Francesca Calore, Ilias Cholis, and Christoph Weniger. Background model systematics for the Fermi GeV excess. *JCAP*, 1503:038, 2015.

[CDFW14] Eric Conte, BÃ'ranger Dumont, Benjamin Fuks, and Chris Wymant. Designing and recasting LHC analyses with MadAnalysis 5. *Eur.Phys.J.*, C74(10):3103, 2014.

[CDM⁺14] Linda Carpenter, Anthony DiFranzo, Michael Mulhearn, Chase Shimmin, Sean Tulin, et al. Mono-Higgs-boson: A new collider probe of dark matter. *Phys.Rev.*, D89(7):075017, 2014.

[CEHL14] Spencer Chang, Ralph Edezhath, Jeffrey Hutchinson, and Markus Luty. Effective WIMPs. *Phys.Rev.*, D89(1):015011, 2014.

[CEMW04] John M. Campbell, R. Keith Ellis, F. Maltoni, and S. Willenbrock. Associated production of a Z Boson and a single heavy quark jet. *Phys.Rev.*, D69:074021, 2004.

[CEMW06] John M. Campbell, R. Keith Ellis, F. Maltoni, and S. Willenbrock. Production of a Z boson and two jets with one heavy-quark tag. *Phys.Rev.*, D73:054007, 2006.

[CG87] R. Sekhar Chivukula and Howard Georgi. Composite Technicolor Standard Model. *Phys.Lett.*, B188:99, 1987.

[CGT13] Nathaniel Craig, Jamison Galloway, and Scott Thomas. Searching for Signs of the Second Higgs Doublet. 2013.

[CHH15] Andreas Crivellin, Ulrich Haisch, and Anthony Hibbs. LHC constraints on gauge boson couplings to dark matter. 2015.

[CHLR13] R.C. Cotta, J.L. Hewett, M.P. Le, and T.G. Rizzo. Bounds on Dark Matter Interactions with Electroweak Gauge Bosons. *Phys.Rev.*, D88:116009, 2013.

[CMS14a] CMS Collaboration. Search for dark matter, extra dimensions, and unparticles in monojet events in proton-proton collisions at $\sqrt{s}$ = 8 TeV. *arXiv:1408.3583 [hep-ex], Submitted to Eur.Phys.J. C*, 2014.

[CMS14b] CMS Collaboration. Search for new phenomena in monophoton final states in proton-proton collisions at $\sqrt{s}$ = 8 TeV. *arXiv:1410.8812 [hep-ex], Submitted to Phys.Lett. B*, 2014.

[CMS14c] CMS Collaboration. Search for the Production of Dark Matter in Association with Top Quark Pairs in the Dilepton Final State in pp collisions at $\sqrt{s} = 8$ TeV. Jun 2014. CMS-PAS-B2G-13-004.

[CMS15a] CMS Collaboration. Search for dark matter direct production using razor variables in events with two or more jets in pp collisions at 8 TeV. Mar 2015. CMS-PAS-EXO-14-004.

[CMS15b] CMS Collaboration. Search for Monotop Signatures in Proton-Proton Collisions at $\sqrt{s} = 8$ TeV. *Phys.Rev.Lett.*, 114(10):101801, 2015.

[CMS15c] CMS Collaboration. Search for physics beyond the standard model in final states with a lepton and missing transverse energy in proton-proton collisions at $\sqrt{s} = 8$ TeV. *Phys.Rev.*, D91(9):092005, 2015.

[CMS15d] CMS Collaboration. Search for the production of dark matter in association with top-quark pairs in the single-lepton final state in proton-proton collisions at sqrt(s) = 8 TeV. *arXiv:1504.03198 [hep-ex], Submitted to JHEP*, 2015.

[CNS+13] Linda M. Carpenter, Andrew Nelson, Chase Shimmin, Tim M.P. Tait, and Daniel Whiteson. Collider searches for dark matter in events with a Z boson and missing energy. *Phys.Rev.*, D87(7):074005, 2013.

[Col15] CMS Collaboration. Search for H/A decaying into Z+A/H, with Z to ll and A/H to fermion pair. 2015.

[CY11] Kyle Cranmer and Itay Yavin. RECAST: Extending the Impact of Existing Analyses. *JHEP*, 1104:038, 2011.

[DDF+12] Celine Degrande, Claude Duhr, Benjamin Fuks, David Grellscheid, Olivier Mattelaer, et al. UFO - The Universal FeynRules Output. *Comput.Phys.Commun.*, 183:1201–1214, 2012.

[dF+14] J. de Favereau et al. DELPHES 3, A modular framework for fast simulation of a generic collider experiment. *JHEP*, 1402:057, 2014.

[DFH+14] Tansu Daylan, Douglas P. Finkbeiner, Dan Hooper, Tim Linden, Stephen K. N. Portillo, et al. The Characterization of the Gamma-Ray Signal from the Central Milky Way: A Compelling Case for Annihilating Dark Matter. 2014.

[DFK+15] B. Dumont, B. Fuks, S. Kraml, S. Bein, G. Chalons, et al. Toward a public analysis database for LHC new physics searches using MADANALYSIS 5. *Eur.Phys.J.*, C75(2):56, 2015.

[DFMQ13] Abdelhak Djouadi, Adam Falkowski, Yann Mambrini, and Jeremie Quevillon. Direct Detection of Higgs-Portal Dark Matter at the LHC. *Eur.Phys.J.*, C73(6):2455, 2013.

[DGIS02] G. D'Ambrosio, G.F. Giudice, G. Isidori, and A. Strumia. Minimal flavor violation: An Effective field theory approach. *Nucl.Phys.*, B645:155–187, 2002.

[DM78] Nilendra G. Deshpande and Ernest Ma. Pattern of Symmetry Breaking with Two Higgs Doublets. *Phys.Rev.*, D18:2574, 1978.

[DNRT13] Anthony DiFranzo, Keiko I. Nagao, Arvind Rajaraman, and Tim M. P. Tait. Simplified Models for Dark Matter Interacting With Quarks. *JHEP*, 1311, 2013.

[DS09] Ethan M. Dolle and Shufang Su. The Inert Dark Matter. *Phys.Rev.*, D80:055012, 2009.

[FHKT11] Patrick J. Fox, Roni Harnik, Joachim Kopp, and Yuhsin Tsai. LEP Shines Light on Dark Matter. *Phys.Rev.*, D84:014028, 2011.

[FHKT12] Patrick J. Fox, Roni Harnik, Joachim Kopp, and Yuhsin Tsai. Missing Energy Signatures of Dark Matter at the LHC. *Phys.Rev.*, D85:056011, 2012.

[FNO07] Stefano Frixione, Paolo Nason, and Carlo Oleari. Matching NLO QCD computations with Parton Shower simulations: the POWHEG method. *JHEP*, 0711:070, 2007. * Temporary entry *.

[For15a] SVN repository for Madgraph input cards for model with s-channel exchange of vector mediator, for electroweak boson final states. https://svnweb.cern.ch/cern/wsvn/LHCDMF/trunk/models/EW_DMV/, 2015. [Online; accessed 15-May-2015].

[For15b] SVN repository for Madgraph inputs for 2HDM model leading to a mono-Higgs signature. https://svnweb.cern.ch/cern/wsvn/LHCDMF/trunk/models/EW_Higgs_2HDM/, 2015. [Online; accessed 12-May-2015].

[For15c] SVN repository for Madgraph inputs for dimension-
7 EFT models with direct DM-EW boson couplings.
https://svnweb.cern.ch/cern/wsvn/LHCDMF/trunk/
models/EW_Fermion_D7/contributed_by_Renjie_Wang/,
2015. [Online; accessed 24-April-2015].

[For15d] SVN repository for Madgraph inputs for model with
s-channel exchange of pseudo-scalar mediator, produced
in association with top quarks. https://svnweb.cern.
ch/cern/wsvn/LHCDMF/trunk/models/HF_S%2BPS/, 2015.
[Online; accessed 24-April-2015].

[For15e] SVN repository for Madgraph inputs for mono-top
models. https://svnweb.cern.ch/cern/wsvn/LHCDMF/
trunk/models/HF_SingleTop/, 2015. [Online; accessed
27-April-2015].

[For15f] SVN repository for Madgraph inputs for simplified
model with a colored scalar mediator coupling to DM
and b-quarks. https://svnweb.cern.ch/cern/wsvn/
LHCDMF/trunk/models/HF_S%2BPS/, 2015. [Online; ac-
cessed 24-April-2015].

[For15g] SVN repository for Madgraph inputs for vector and
scalar mediator models leading to a mono-Higgs sig-
nature. https://svnweb.cern.ch/cern/wsvn/LHCDMF/
trunk/models/EW_Higgs_all/, 2015. [Online; accessed
24-April-2015].

[For15h] SVN repository for Madgraph inputs with t-channel
exchange of colored scalar mediator. https://svnweb.
cern.ch/cern/wsvn/LHCDMF/trunk/models/Monojet_
tChannel/, 2015. [Online; accessed 27-April-2015].

[For15i] SVN repository for POWHEG input card for model with
s-channel exchange of axial vector mediator. https:
//svnweb.cern.ch/cern/wsvn/LHCDMF/trunk/models/
Monojet_DMA/, 2015. [Online; accessed 24-April-2015].

[For15j] SVN repository for POWHEG input card for model
with s-channel exchange of pseudo-scalar mediator,
coupling to the quarks through a top loop. https:
//svnweb.cern.ch/cern/wsvn/LHCDMF/trunk/models/
Monojet_DMP_tloop/, 2015. [Online; accessed 24-April-
2015].

[For15k] SVN repository for POWHEG input card for model
with s-channel exchange of scalar mediator, . https:
//svnweb.cern.ch/cern/wsvn/LHCDMF/trunk/models/
Monojet_DMS_topLoop/, 2015. [Online; accessed 24-April-
2015].

[For15l]   SVN repository for POWHEG input card for model
           with s-channel exchange of vector mediator. `https://svnweb.cern.ch/cern/wsvn/LHCDMF/trunk/models/Monojet_DMS/`, 2015. [Online; accessed 24-April-2015].

[FST06]   Jonathan L. Feng, Shufang Su, and Fumihiro Takayama.
           Lower limit on dark matter production at the large
           hadron collider. *Phys.Rev.Lett.*, 96:151802, 2006.

[FW13]   Patrick J. Fox and Ciaran Williams. Next-to-Leading
           Order Predictions for Dark Matter Production at Hadron
           Colliders. *Phys.Rev.*, D87(5):054030, 2013.

[GHS13]   A. Goudelis, B. Herrmann, and O. StÃĕl. Dark matter in
           the Inert Doublet Model after the discovery of a Higgs-
           like boson at the LHC. *JHEP*, 1309:106, 2013.

[GIR+10]   Jessica Goodman, Masahiro Ibe, Arvind Rajaraman,
           William Shepherd, Tim M.P. Tait, et al. Constraints on
           Dark Matter from Colliders. *Phys.Rev.*, D82:116010, 2010.

[GIR+11]   Jessica Goodman, Masahiro Ibe, Arvind Rajaraman,
           William Shepherd, Tim M.P. Tait, et al. Constraints on
           Light Majorana dark Matter from Colliders. *Phys.Lett.*,
           B695:185–188, 2011.

[GS11]   Jessica Goodman and William Shepherd. LHC Bounds
           on UV-Complete Models of Dark Matter. 2011.

[HFF+11]   Valentin Hirschi, Rikkert Frederix, Stefano Frixione,
           Maria Vittoria Garzelli, Fabio Maltoni, et al. Automation
           of one-loop QCD corrections. *JHEP*, 1105:044, 2011.

[HHR14]   Ulrich Haisch, Anthony Hibbs, and Emanuele Re. De-
           termining the structure of dark-matter couplings at the
           LHC. *Phys.Rev.*, D89(3):034009, 2014.

[HKR13]   Ulrich Haisch, Felix Kahlhoefer, and Emanuele Re. QCD
           effects in mono-jet searches for dark matter. *JHEP*,
           1312:007, 2013.

[HKSW15]   Philip Harris, Valentin V. Khoze, Michael Spannowsky,
           and Ciaran Williams. Constraining Dark Sectors at Col-
           liders: Beyond the Effective Theory Approach. *Phys.Rev.*,
           D91(5):055009, 2015.

[HKU13]   Ulrich Haisch, Felix Kahlhoefer, and James Unwin.
           The impact of heavy-quark loops on LHC dark matter
           searches. *JHEP*, 1307:125, 2013.

[HR90]   L.J. Hall and Lisa Randall. Weak scale effective super-
           symmetry. *Phys.Rev.Lett.*, 65:2939–2942, 1990.

[HR15]   Ulrich Haisch and Emanuele Re. Simplified dark matter
           top-quark interactions at the LHC. 2015.

[KAM$^+$12] S. Kraml, B.C. Allanach, M. Mangano, H.B. Prosper, S. Sekmen, et al. Searches for New Physics: Les Houches Recommendations for the Presentation of LHC Results. *Eur.Phys.J.*, C72:1976, 2012.

[Kap92] David B. Kaplan. A Single explanation for both the baryon and dark matter densities. *Phys.Rev.Lett.*, 68:741–743, 1992.

[KKL$^+$14a] Sabine Kraml, Suchita Kulkarni, Ursula Laa, Andre Lessa, Veronika Magerl, et al. SModelS v1.0: a short user guide. 2014.

[KKL$^+$14b] Sabine Kraml, Suchita Kulkarni, Ursula Laa, Andre Lessa, Wolfgang Magerl, Doris Proschofsky, and Wolfgang Waltenberger. SModelS: a tool for interpreting simplified-model results from the LHC and its application to supersymmetry. *Eur.Phys.J.*, C74:2868, 2014.

[Kop11] Joachim Kopp. Collider Limits on Dark Matter. 2011.

[KPSW] I.-W. Kim, M. Papucci, K. Sakurai, and A. Weiler. ATOM: Automated Testing Of Models. *to appear*.

[KSTR15] Jong Soo Kim, Daniel Schmeier, Jamie Tattersall, and Krzysztof Rolbiecki. A framework to create customised LHC analyses within CheckMATE. 2015.

[LHNOT07] Laura Lopez Honorez, Emmanuel Nezri, Josep F. Oliver, and Michel H.G. Tytgat. The Inert Doublet Model: An Archetype for Dark Matter. *JCAP*, 0702:028, 2007.

[LKW13] Tongyan Lin, Edward W. Kolb, and Lian-Tao Wang. Probing dark matter couplings to top and bottom quarks at the LHC. *Phys.Rev.*, D88(6):063510, 2013.

[LPS14] Hyun Min Lee, Myeonghun Park, and Veronica Sanz. Gravity-mediated (or Composite) Dark Matter. *Eur.Phys.J.*, C74:2715, 2014.

[LSWY13] Jia Liu, Brian Shuve, Neal Weiner, and Itay Yavin. Looking for new charged states at the LHC: Signatures of Magnetic and Rayleigh Dark Matter. *JHEP*, 1307:144, 2013.

[MMA$^+$14] Sarah Malik, Christopher McCabe, Henrique Araujo, A. Belyaev, Celine Boehm, et al. Interplay and Characterization of Dark Matter Searches at Colliders and in Direct Detection Experiments. 2014.

[MMPT07] Michelangelo L. Mangano, Mauro Moretti, Fulvio Piccinini, and Michele Treccani. Matching matrix elements and shower evolution for top-quark production in hadronic collisions. *JHEP*, 0701:013, 2007.

[MMW05] Fabio Maltoni, Thomas McElmurry, and Scott Willenbrock. Inclusive production of a Higgs or Z boson in association with heavy quarks. *Phys.Rev.*, D72:074024, 2005.

[Nas04] Paolo Nason. A New method for combining NLO QCD with shower Monte Carlo algorithms. *JHEP*, 0411:040, 2004.

[NCC$^+$14] Andy Nelson, Linda M. Carpenter, Randel Cotta, Adam Johnstone, and Daniel Whiteson. Confronting the Fermi Line with LHC data: an Effective Theory of Dark Matter Interaction with Photons. *Phys.Rev.*, D89(5):056011, 2014.

[Nus85] S. Nussinov. TECHNOCOSMOLOGY: COULD A TECHNIBARYON EXCESS PROVIDE A 'NATURAL' MISSING MASS CANDIDATE? *Phys.Lett.*, B165:55, 1985.

[par] DM@LHC participants. DM@LHC 2014 proceedings. To appear.

[PS14] Alexey A. Petrov and William Shepherd. Searching for dark matter at LHC with Mono-Higgs production. *Phys.Lett.*, B730:178–183, 2014.

[PSWZ14] Michele Papucci, Kazuki Sakurai, Andreas Weiler, and Lisa Zeune. Fastlim: a fast LHC limit calculator. *Eur.Phys.J.*, C74(11):3163, 2014.

[PVZ14] Michele Papucci, Alessandro Vichi, and Kathryn M. Zurek. Monojet versus the rest of the world I: t-channel models. *JHEP*, 1411:024, 2014.

[RWZ15] Davide Racco, Andrea Wulzer, and Fabio Zwirner. Robust collider limits on heavy-mediator Dark Matter. 2015.

[SMS06] Torbjorn Sjostrand, Stephen Mrenna, and Peter Z. Skands. PYTHIA 6.4 Physics and Manual. *JHEP*, 0605:026, 2006.

[SV12] Ian M. Shoemaker and Luca Vecchi. Unitarity and Monojet Bounds on Models for DAMA, CoGeNT, and CRESST-II. *Phys.Rev.*, D86:015023, 2012.

[WBG05] M.R. Whalley, D. Bourilkov, and R.C. Group. The Les Houches accord PDFs (LHAPDF) and LHAGLUE. 2005.

[WY12] Neal Weiner and Itay Yavin. How Dark Are Majorana WIMPs? Signals from MiDM and Rayleigh Dark Matter. *Phys.Rev.*, D86:075021, 2012.

[WY13] Neal Weiner and Itay Yavin. UV completions of magnetic inelastic and Rayleigh dark matter for the Fermi Line(s). *Phys.Rev.*, D87(2):023523, 2013.

[ZBW13] Ning Zhou, David Berge, and Daniel Whiteson. Mono-
everything: combined limits on dark matter produc-
tion at colliders from multiple final states. *Phys.Rev.*,
D87(9):095013, 2013.